THE NANOSTRUCTURE FORMATIONS ON THE STRANSKI KRASTANOW FILM-SUBSTRATE SYSTEM

HUANG ZHIJUN

[B. Eng]

A THESIS SUBMITTED

FOR THE DEGREE OF DOCTOR OF PHILOSOPHY

DEPARTMENT OF MATERIALS SCIENCE AND ENGINEERING

NATIONAL UNIVERSITY OF SINGAPORE

2008

Acknowledgement

I would like to express my great gratitude to my supervisor Dr. Chiu Cheng-hsin for his invaluable guidance and encouragement during my Ph.D. study.

I will also like to thank all the group members, Wang HangYao, Xie YiLun, C-T Poh, Koh TiongSong and Gerard Paul Marcelo Leyson for the insightful discussions and all the assistance.

Special thanks will be given to my wife and my parents for their remarkable patience and constant support. It will not be possible for me to complete my study without them.

Finally, I want to acknowledge National University of Singapore for the research scholarship.

Contents

Acknowledgement **i**

Contents **ii**

Abstract **vii**

List of figures **ix**

1 Introduction **1**

1.1 Review of the Self-Assembled Nanostructures 1

1.2 Objective and Approach 5

1.2.1 Formation of nanostructures in typical SK system 5

1.2.2 Nanostructures formation in SK system under electric field 7

1.3 Literature Review of Methodology 8

1.3.1 Numerical Simulation 8

1.3.2 Energy Analysis 9

1.4 Outline 11

2 Model **12**

2.1 SK System without Electric Field 12

2.1.1 The SK system 12

2.1.2 The surface chemical potential χ 15

2.1.3 The morphological evolution driven by surface diffusion 15

2.2 SK System with Electric Field 16

3 Energy Analysis **18**

3.1 Strain Energy 18

3.1.1 A single nanostructure 19

3.1.2 An adjacent nanostructure 22

3.1.3 A small adjacent nanostructure with the same facet as the pre-existing one 23

3.2 Electrostatic Energy 26

3.2.1 Problem statement 26

3.2.2 The complex-variable method 28

3.2.3 The first-order perturbation analysis 32

3.3 Interaction Energy 44

3.4 Surface Energy 46

4 Critical Film Thickness for Stranski-Krastanow Transition **47**

4.1 Introduction 47

4.2 The Critical Film Thickness of the SK Transition 48

4.3 The Activated Stranski-Krastanow Transition Method 55

4.3.1 Introduction 55

4.3.2 Numerical Simulation 56

4.4 Discussion 59

5 Formation of Nanostructures by Surface Undulation **61**

5.1 Introduction 61

5.1.1 Critical film thickness 61

5.1.2 The fastest surface undulation mode 62

5.2 Model and Methodology 64

5.2.1 Approach 64

5.3 The Common Features 65

5.3.1 The formation process on the coarsening SK systems 66

5.3.2 The wetting layer thickness 68

5.3.3 The island width 69

5.3.4 The formation of faceted island 69

5.3.5 Comparison 70

5.4 The Maximum Surface Coverage $\xi_{\max}$ of Faceted Islands 71

5.4.1 Derivation of $\xi_{\max}$ 71

5.4.2 The effects of $\mathcal{F}$, $\hat{H}_f$, and α on $\xi_{\max}$ 72

5.5 The Film Morphologies 74

5.5.1 An array of separate islands 74

5.5.2 Localized wetting layers and induced facets 75

5.5.3 The faceted ripple structure I 76

5.5.4 The Faceted Ripple Structure II 77

5.5.5 The nanostructure formation under the influence of a minimum of γ 79

5.6 Summary 79

6 Self-Assembly of Quantum Dot Molecules by Cooperative Formation 81

6.1 Introduction 81

6.2 Numerical Simulation for the CRT Formation 84

6.3 Kinetic pathways 87

6.4 Energy Analysis for the Cooperative Formation 89

6.4.1 A model problem 90

6.4.2 Energy changes 91

6.4.3 The gradient $\mathcal{F}$ 95

6.4.4 Derivation of $\mathcal{F}$ 96

6.4.5 Critical pit size for adjacent ridge formation 97

6.4.6 Fully faceted adjacent ridge 98

6.5 Discussion 99

6.5.1 The CRT formation 99

6.5.2 Deposition 100

6.5.3 Limitations 101

7 The SK System under Electric Field 103

7.1 Introduction 103

7.2 Model and Energy Analysis 104

7.2.1 Model system 105

7.2.2 Energy analysis 105

7.2.3 Parameters and normalization 107

7.3 SK Systems without Electric Field 109

7.3.1 Characteristics of the total energy change . . . 110
7.3.2 Stability condition against size variation . . . 111
7.4 Effects of Electric Field . . . 113
7.4.1 Characteristics of ΔE_{tot} and phase diagram of wire size stability . . 114
7.4.2 Boundaries of stable wire region . . . 116
7.5 The Asymptotic Cases . . . 117
7.5.1 Minimum criterion and basic stable states . . . 117
7.5.2 Maximum EM strength and utmost stable states . . . 122
7.5.3 Size stability of wires . . . 123
7.6 Numerical Simulation . . . 124
7.7 Discussion . . . 126
7.7.1 Modification of SK systems for stable nanostructures . . . 126
7.7.2 Kinetics . . . 127
7.7.3 Controlled growth of nanoislands . . . 128
7.7.4 Limitations . . . 129
7.8 Summary . . . 130

8 Conclusion **131**

Abstract

The thesis presents our study about the formation of nanostructures on the Stranski-Krastanow film-substrate system and our proposed schemes to control the self-assembled nanostructures in term of size, shape and site.

The study is conducted via two approaches: the energy analysis using the first order boundary perturbation method and 3-dimensional numerical simulation for the morphological evolution in the SK system. It is demonstrated in this thesis that the combination of these two methods is a powerful tool to analyze the nanostructures formation in the SK system.

First of all, our analysis shows that the critical film thickness under nucleation and surface undulation are different due to the nature of these two kinetic mechanisms. The recognition of two critical film thicknesses lays the foundation of our further study on the schemes to control the nanostructures.

Our subsequent investigations on the SK transition process reveal the common features of nanostructures and their formation mechanisms. Our parametric study demonstrates the impact of the key material properties such as the mismatch strain, surface energy density, interaction energy density and film thickness. Particularly, our analysis on the film thickness effect leads to the understanding of the mechanism for quantum dot molecules.

On the other hand, our study on the SK film-substrate system under the effect of electric field shows that it is possible to find equilibrium state for the nanostructures under the patterned electric field, and these nanostructures are stable against coarsening. Besides the analytical study, our numerical simulation also demonstrates the potential of controlling the nanostructures in terms of their sizes, shapes and sites by using patterned electrode.

List of Tables

5.1 The values of $\hat{g}_0 l$ and L of the cases considered in the parametric study . . 65

5.2 The maximum surface coverage and the island base width obtained by numerical simulation 71

6.1 Three film thicknesses and the initial surface profiles for QDMs 85

List of Figures

3.1 Schematic diagram of a heteroepitaxial film-substrate system 19
3.2 Schematic diagram of a nanostructure developing at the adjacent site . . . 22
3.3 Schematic diagram of conductive film-substrate system under electric field 27
3.4 Schematic diagram of two flat electrodes 30
3.5 Schematic diagram of two flat electrodes 31
3.6 Schematic diagrams of film-substrate structure under electrodes 36
3.7 Schematic diagram of a trapezoidal wire under trapezoidal pattern 41
3.8 Variation of U_1 with the wire width and U_2 with d_2/d_1 43

4.1 Schematic diagram for calculation the critical film thickness H_1 48
4.2 The critical film thickness of spontaneous formation 49
4.3 The critical film thickness of spontaneous formation 51
4.4 The contours of $H_2 - H_1$ 53
4.5 Simulation results of the ASKT method 56
4.6 The simulation results of different nanostructures produced with the ASKT method 58

5.1 Morphological evolution of SK system for class I2, J2, and K2 66
5.2 Evolution of the surface coverage 67
5.3 Cross-section profile of the I, J, K cases 68
5.4 Schematic diagram of the general island formation process 70
5.5 Variation of $\xi_{\max}$ with $\hat{H}_f$ 73
5.6 Morphological evolution of the faceted ripple structures 76
5.7 Morphological evolution of the SK system with minimum on (001) 78

6.1 Morphological evolution $Si_{0.7}Ge_{0.3}/Si$ with different film thickness and initial surface profiles . . . 86
6.2 Morphological evolution $Si_{0.7}Ge_{0.3}/Si$ at thin film with indent files . . . 87
6.3 Morphological evolution of a single QDMs . . . 88
6.4 Schematic diagrams of the two competing pathways of the CRT formation 89
6.5 Contours of the energy difference ΔE_{tot} as a function of ΔV and θ . . . 94
6.6 Effects of ΔV on ΔE_{eq} and ΔE_{tot} of faceted ridges . . . 95
6.7 Variation of $\pi\mathcal{F}/w_0\mathcal{S}$ with the normalized pit size $\hat{a}$ . . . 97

7.1 Schematic diagram of a triangular wire under a triangular patterned electric plate . . . 105
7.2 Contours of $\mathcal{J}$ as a function of $\hat{d}$ and $\hat{\mathcal{S}}_e$ . . . 109
7.3 Contours of $\mathcal{J}$ as a function of $\hat{d}$ and $\hat{\mathcal{S}}_e$variation of $\Delta\hat{E}_{tot}$ with $\hat{a}$ . . . 110
7.4 region of $(\hat{\Sigma}, \hat{H}_f)$ satisfying condition I . . . 113
7.5 Variation of $\Delta E_{tot}/\gamma_0 L$ with a and H_v . . . 115
7.6 Contours of $\mathcal{J}_{min}$ and $\hat{a}_{min}$ . . . 118
7.7 Simulation results of the EMSO process . . . 125

Chapter 1

Introduction

1.1 Review of the Self-Assembled Nanostructures

The self-assembly of nanostructures on the Stranski-Krastanow (SK) systems has attracted the attention of many researchers because of its potential applications in the manufacture of the optoelectronic devices, cellular automata, and other nano-scale devices. The nanostructures of the systems form after the film exceeds the critical thickness for the SK transition where the flat film surface becomes unstable against island formation (Asaro and Tiller 1972; Spencer et al. 1991; Srolovitz 1989). The size of the structures can be of the order of nanometer, and the self-assembly process can be applied to various material systems, including the SiGe/Si (Eaglesham and Cerullo 1990; Mo et al. 1990), the InGaAs/GaAs (Leonard et al. 1993; 1994), and the InP/GaInP systems (Ballet et al. 2000).

The self-assembly of nanostructures on the SiGe/Si(001) system has been of particular interest primarily due to the fact that the system serves as a good model for understanding the self-assembly process, and the system may be easily integrated into the Si-based microelectronics. The SiGe/Si(001) system can develop different types of nanostructures, characterized by specific facets and shapes. Examples include faceted islands such as pyramids, huts, and domes (Eaglesham and Cerullo 1990; Floro et al. 1997; 1998; Medeiros-Ribeiro et al. 1998; Mo et al. 1990; Ross et al. 1999; Stoffel et al.

2007), structures growing into films such as trenches and pits (Deng and Krishnamurthy 1998; Goldfarb et al. 1997; Jesson et al. 1996; Li et al. 2001; Shi and Lederman 2000), and structures consisting of ridges, islands, trenches, and pits such as the faceted ripple structures (Liu and Zhang 2007; Ozkan et al. 1997; 1999) and the quantum fortress (Gray et al. 2004c).

In order to realize the device applications, it is crucial to control the islands size uniformity since the size significantly affects the properties of each island due to the quantum confinement effect. However, the task is challenging. The difficulties mainly come from the instability of islands against coarsening where the larger islands grow bigger and the smaller ones tend to reduce their size, leading to a larger size distribution (Floro et al. 2000; Helen and Daniel 2005; Liu and Zhang 2007; Medeiros-Ribeiro et al. 1998; Stoffel et al. 2007). Although the island-coarsening problem has been well understood and recognized as a major obstacle to the development of self-assembly technology, how to suppress the coarsening process remain an open question (Chiu and Huang 2006; Daruka et al. 1999; Liang and Suo 2001; Shchukin and Bimberg 1998).

Many schemes have been suggested in the literature to overcome the challenges in the self-assembly of nanoislands on the SK systems. The schemes can be generally classified into five categories. The first one is to enhance the materials properties of the SK systems such as the surface stress (Daruka and Barabasi 1997; Medeiros-Ribeiro et al. 1998; Shchukin et al. 1995), the film-substrate interaction (Chiu 1999a; 2004) and the strain-dependent surface energy (Lu and Liu 2005; Retford et al. 2007; Shklyaev et al. 2005) in order to induce island arrays that are stable against coarsening.

In comparison, the second category employs embedded structures to improve the uniformity of the island size and spacing. The embedded structures can be multiple arrays of nanoislands separated by layers of a different material (Chiu and Wang 2007; G. et al. 2000; Liu et al. 2007; Tersoff et al. 1996). The embedded structures can also be the misfit dislocations in the strained film (Romanov et al. 1999; Shiryaev et al. 1997) or a regular dislocation network generated by bonding a film onto a substrate of the same material but with a twist and/or miscut between them (Pascale et al. 2006; Poydenot

et al. 2006).

The third category exploits special features on the film surface to control the growth of nanoislands. The features can be fabricated by lithography, which include mesas (Jin et al. 2000; Kamins et al. 1999; Kamins and Williams 1997; Kitajima et al. 2002; Konkar et al. 1998; Lee et al. 2000; Yang et al. 2004; Zhang et al. 1998), pit arrays (Chen et al. 2006; Jang et al. 2007; Kiravittaya et al. 2004; Machtay and Kukta 2006; Schmidt et al. 2000; Zhong et al. 2003), patterned oxide masks (Berbezier and Ronda 2007; Eggleston and Voorhees 2002; Nitta et al. 2000; Yoon et al. 2006), micropatterning by focused ion beams (Kammler et al. 2003; McKay et al. 2007), thin patterned films (Chiu et al. 2004), microdisks (Xie and Solomon 2005) and gold patterns (Robinson et al. 2006; 2007). The surface features can also be generated by novel techniques adopted in the growth process such as activating step bunching to produce regular ripples on vicinal surfaces (Zhu et al. 1998) .

The fourth category is making use of the rippling on solid surfaces at the length scale of nanometer. The phenomenon was observed in (Jesson et al. 1996) by annealing a $Si_{0.5}Ge_{0.5}$ alloy film of 5 nm in thickness on a thick Si substrate at temperatures ranging from 570 to 590 °C.The result revealed that the film developed into nanoridges and nanotrenches via a cooperative manner that the two types of nanostructures formed one after another at the adjacent sites. The cooperative ridge-trench (CRT) formation continued, resulting in a ripple structure.

After the observation by Jessen et al. (1996b), the CRT formation was realized to be a useful mechanism for self-assembling quantum-dot molecules (QDMs) on heteroepitaxial systems (Deng and Krishnamurthy 1998; Gray et al. 2002; 2006). The fabrication process of the QDMs consisted of two steps. The first step is to generate shallow holes on solid surfaces by embedding a small amount of hard particles in a buffer layer prior to the deposition of a heteroepitaxial film (Borgström et al. 2003; Deng and Krishnamurthy 1998; Weil et al. 1998). The shallow holes would trigger the CRT formation on the film in the second step, causing the self-assembly of QDMs around the holes. The QDMs generated by this process are clusters of dots with the number of dots being adjustable (Huang

et al. 2007; Sirlpitakchai and Suraprapapich 2007; Songmuang et al. 2003). The size distribution of the QDMs is much more uniform than that of single quantum dots. These advantages, namely, self-assembly, unique structures, adjustable number of dots, and uniform size distribution, suggest that the QDMs are a promising building block for quantum computation devices (Barth et al. 2005).

In addition to the two situations mentioned above, the CRT formation also happened on heteroepitaxial films during the deposition process (Deng and Krishnamurthy 1998; Jesson et al. 1996). This issue is examined in a series of papers aiming at understanding the dependence of the CRT formation on the growth rate, the substrate temperature, the film thickness, and the interrupting annealing during the process (Gray et al. 2004a; 2002; 2004b; 2005; 2004c; Vandervelde et al. 2003).

The fifth scheme, sometimes called the lithographically induced self-assembly (LISA), a liquid polymeric film on a thick substrate is exposed to an electrode with the gap between the film and the electrode being filled with air (Chou et al. 1999; Schäffer et al. 2000) and/or another liquid layer (Deshpande and Chou 2001; Lin et al. 2001; Lu et al. 2006; Morariu et al. 2003). The system is subject to an electric field, which can be an external one resulting from an applied voltage (Schäffer et al. 2000) or an intrinsic one due to localized charges or contact potential (Chou et al. 1999). The electric field causes the liquid film to form structures by viscous flow of the film. The advantage of the scheme is the capability of using patterns on the electrode to manipulate the sizes, shapes, and sites of the structures. The scheme, on the other hand, has the disadvantage of dielectric breakdown in the gap, limiting the reduction of the structure spacing and size (Pease et al. 2004). Another concern is the long-range ordering and the coalescence of the structures since in general the structures are unstable against size variation (Leach et al. 2005; Pease et al. 2004).

1.2 Objective and Approach

The objective of this research is to understand the self-assembly of nanoislands in typical SK systems and to develop a strategy for controlling the sizes, the shapes and the sites of islands in the SK system from theoretical points of view. The approaches adopted to investigate these two issues are discussed in the following sections.

1.2.1 Formation of nanostructures in typical SK system

Our study of the self-assembly process in the SK systems starts with the critical thickness of the SK transition on the film. Of particular interest is how the critical thickness is affected by the two island formation mechanisms of the systems, namely, surface undulation and nucleation. The formation via surface undulation follows a gradual morphological change from a smooth wavy surface to facet islands (Tersoff et al. 2002). Nucleation, on the other hand, refers to the spontaneous formation of islands larger than a critical size (Tersoff and Tromp 1993). By either mechanism, the islands on the SK system can develop only after the film exceeds a critical thickness.It is found that the critical thickness under the two mechanisms are different, and that under the surface undulation is larger than that under the nucleation in most of the cases.

Based on the finding of the two critical film thicknesses, we study the formation of nanostructures in three different regions of film thickness: between the two critical film thickness, slightly higher than the critical film thickness for surface undulation and thickness far exceeding the critical value.

For the thickness range between the two critical values, an almost flat film can develop into islands via spontaneous formation but with surface undulation being suppressed. The thickness range enables the nano-structures formation on the SK systems to be controllable. In this thesis, we propose to make simple patterns on the flat surfaces of the SK systems in the special film thickness range and then anneal the systems. The scheme is termed the activated SK transition (ASKT) method since the method is to trigger the SK transition to form nano-crystals at the pattern sites by self-assembly during the annealing

process (Chiu et al. 2004). The ASKT method is explored by simulating the morphological evolution of patterns on the SK systems in the special thickness range during the annealing process. The results show that the ASKT method has the potential capability to control the nano-crystal locations, and it can produce complicated shapes that cannot be easily fabricated by the conventional growth techniques. Furthermore, the feature length of the crystals can be a fraction of the original pattern size, and it can be tailored by adjusting the mismatch strain in the film without reducing the pattern size.

For the case where the film thickness is slightly above the critical value for surface undulation, we investigate the nanostructure formation effected by the surface undulation on the SK systems by carrying out three-dimensional simulation for the process. Particularly, we studied how the surface undulation led to the development of faceted nanostructures and wetting layers and how the development would be affected by the parameters of the SK systems. The results reveal that the development exhibits three common features in the coarsening SK systems. The results also provide an insight into the effects of the parameters of the SK systems on the maximum surface coverage of faceted islands, which in turn is the crucial quantity controlling the film morphologies during the formation process.

For the case of thick films, the morphological evolution is mainly characterized by the CRT formation; hence, our focus in this case is to illuminate the mechanism causing the CRT formation and to understand why the CRT formation can produce nanostructures of uniform size. The CRT formation is commonly explained by the cooperative nucleation model (Jesson et al. 1996). The model suggested that the presence of one type of structure (e.g. a trench) can reduce the energy barrier for the nucleation of the other type (e.g. an island) at the adjacent site, thus facilitating the repeating occurrences of the two types of structures (Jesson et al. 1996). The model points out the significant effects of an existing nanostructure on the nucleation of a different one; however, the nucleation model cannot fully account for the uniform size distribution of the ripple structures and QDMs.

We examined the CRT formation in this thesis by considering two issues that were overlooked previously. First, instead of nucleation, the adjacent new structure may de-

velop gradually via the surface undulation process. The surface undulation process, as mentioned earlier, is another mechanism of the morphological evolution of the film surface. The process is characterized by a gradual change of the surface profile, and the process can lead to the formation of faceted islands without experiencing an energy barrier (Chiu and Huang 2006; 2007; Tersoff et al. 2002). These unique features suggest that the surface undulation process can play an important role in the development of the adjacent new structure. Second, the gradual development of the adjacent new structure has to compete with the growth of the existing outermost one. The competition between the two pathways is the key to the alternative growth of ridges and trenches during the CRT formation (Huang et al. 2007).

1.2.2 Nanostructures formation in SK system under electric field

In the second part of the thesis, we examine the approach of applying patterned electrode to the self-assembly of nanoislands on the SK systems to fabricate nanostructures. The approach is termed the electromolding self-organization (EMSO) process in this thesis. The EMSO process retains the characteristics of the patterned electrode and the self-assembly of nanostructures in SK systems. The patterned electrode is an effective way to have complete control over the sizes, shapes, and sites of the self-assembled nanoislands; and the nanostructures developing from the SK systems exhibit remarkable material quality and properties.

In addition to these advantages, the most important feature of the EMSO process is that the process can produce nanostructures stable against size variation. This is in contrast to the common problem of unstable islands in previous schemes, such as the LISA method and the self-assembly of nanoislands in the SK systems. The unique feature is achieved by growing a flat film below the critical thickness for the SK transition. Because the flat film in such a case is the equilibrium profile, when a patterned electrode is used to generate a non-uniform electric field in the system, the flat film can be activated locally

to develop into an islanded surface that is the equilibrium or the meta-stable state. The equilibrium/meta-stable state realizes the island stability against size variation.

We explore the EMSO process in this thesis by carrying out energy analysis for the island formation and numerical simulations for the morphological evolution of the system. We focus on the case where the patterned electrode is applied during the annealing process of an SK system consisting of a conductor film and a semi-conductor substrate.

1.3 Literature Review of Methodology

The problems considered in this thesis are investigated by analyzing the total energy of the system and by simulating the morphological evolution during the annealing process. The methodologies presented in the literature for the energy analysis and the numerical simulation are reviewed in the following two sections. The methodologies adopted in this thesis are discussed later in Chap. 2.

1.3.1 Numerical Simulation

Three-dimensional (3D) simulation for the formation of nanostructures by the surface undulation process have been an important tool for studying the nanostructures on SK systems (Chiu 1999a;b; 2004; Chiu et al. 2004; Golovin et al. 2003; Levine et al. 2007; Liu and Zhang 2007; Liu et al. 2003a;c; Muller and Grand 1999; Pang and Huang 2007; Ramasubramaniam and Shenoy 2004; Tekalign and Spencer 2004; Zhang 2000; Zhang and Bower 2001). All of the simulations are based on a similar evolution equation to describe how the film morphology changed gradually when the surface chemical potential varied on the film surface. The key kinetic mechanism behind the equation is surface diffusion (Mullins 1957), while the growth of film can also be included (Chiu and Gao 1995; Liu et al. 2003a).

Several methods have been proposed to solve the evolution equation of the 3D cases. A straightforward method is to evaluate the surface chemical potential and then substitute

the result into the governing equation to simulate the morphological evolution (Chiu 1999a;b; 2004; Chiu et al. 2004; Liu and Zhang 2007). Besides the direct method, the evolution equation can also be solved by the finite element method (FEM) (Liu and Zhang 2007; Liu et al. 2003a;b;c; Ramasubramaniam and Shenoy 2004; Zhang 2000; Zhang and Bower 2001), and the phase field method (Muller and Grand 1999). All of the three methods need to evaluate the strain energy density on the film surface at each time step, a time-consuming calculation that can impose a severe limitation on the number of nanostructures allowed in a simulation. In spite of the difficulty, the results obtained by these methods are promising. Large scale simulations for rounded (Liu et al. 2003a) and hut islands (Chiu 2004; Liu and Zhang 2007) have been demonstrated recently.

Contrary to the methods that solve the full evolution equation, the fourth method adopts the assumption of a small surface slope to reduce the full evolution equation to a simpler one in which the surface migration rate is expressed as a function of the surface profile explicitly (Spencer et al. 1993). The scheme avoids evaluating the strain energy density during the simulation, and it has been successfully implemented for the 3D cases (Golovin et al. 2003; Tekalign and Spencer 2004). More recently, numerical simulation has also been developed to study the electric field induced viscous flow on the liquid film (Kim and Lu 2006; Verma et al. 2005).

1.3.2 Energy Analysis

The elasticity problem of nanostructures on heteroepitaxial film-substrate system has been studied by many researchers (Floro et al. 1997; Gray et al. 2002; Rastelli et al. 2001; Tersoff and Tromp 1993). One question often encounted when studying the nanostructures is the strain energy change during the island formation and the island shape transition processes. The question can be solved by FEM for linear elasticity problems and there is no difficulty to calculate any island shape.

Besides the FEM, Gao (Gao 1991a) proposed the first-order boundary perturbation method for solving the elasticity problem of a 2D strained solid with a wavy surface. The

method is accurate to the first-order of slope of the surface, and it can be applied to any smooth island profile, including cosine curves and 3D hexagonal island arrays. The method can also be extended to anisotropic solids and elastically dissimilar film-substrate systems (Gao 1991b).

A different perturbation method has been proposed by Tersoff and Tromp (1993). They showed that under the shallow island assumption, the effects of an island on the elasticity solution can be approximated by a distribution of surface traction on the flat surface of a semi-infinite solid. This approach can be used to model smooth surface profile as well as facet island in both 2D and 3D cases (Daruka et al. 1999).

In this thesis, we present the energy analysis using surface-traction approach for estimating the strain energy of facet island on the SK system. The advantage of this approach is that it only requires one-dimensional integral when evaluating the island strain energy change due to island formation in the two-dimensional cases. The formula is valid for single island containing one type or multiple types of facets and it is also valid for island arrays.

Besides the strain energy, another question often encountered when analyzing the growth of the nanostructures under the influence of the electrodes is to determine the electric field along the film surfaces and to calculate the corresponding electrostatic energy change during the process. This electrostatic problem can also be solved numerically by the finite element method (Hughes 1987) and the boundary element method (Beer 2001), which can take into account the effects of the shapes of the film and electrode surfaces precisely. Besides the numerical results, perturbation solutions of different cases involving two parallel electrodes are also available in the literature. For example, the results of flat electrodes containing air and a wavy dielectric film were derived by Schaffer et al. (2001) and by Yang and Song (2005), and those containing dielectric bi-layers with a wavy interface between the bi-layers were considered by Pease and Russel (2003, 2004) and by Lin et al. (2001). The scenario of wavy electrodes with a dielectric media was examined by Du and Srolovitz (2004); that of patterned electrodes with dielectric bi-layers by Verma et al. (2005); and that of anisotropic dielectric material was investigated by Chien et al.

(1996).

1.4 Outline

The outline of this thesis is as follows. Chapter 2 presents the continuum model for the SK system with and without the electric field. Chapter 3 describes the detailed energy analysis based on the first-order boundary perturbation method. Chapter 4 discusses our findings of the critical film thickness of the SK system and its applications in the ASKT method. Chapter 5 illustrates the formation of faceted islands on the film surface with the film thickness slightly higher than the critical value for the SK transition. Chapter 6 demonstrates the SK transition on thick film and the mechanism for the development of QDMs. Chapter 7 is devoted to the proposed scheme of using patterned electric plate to control the formation of nanostructures and the stability of the structures against size variation. This thesis is concluded with a summary in Chap. 8.

Chapter 2

Model

Our study of the nanostructures formation on the Stranski-Krastanow heteroepitaxial film-substrate system is mainly conducted under two scenarios: without electric field, and with electric field. This chapter presents the models adopted in this thesis for studying the nanostructure formation on the SK heteroepitaxial film-substrate system. In particular, Sec.2.1 focuses on the model for the scenario that the electric field is absent from the system, and Sec. 2.2 on that for the case when the electric field is present.

2.1 SK System without Electric Field

2.1.1 The SK system

Our study is based on a continuum model for the SK system which contains a thin film and a thick substrate bonded coherently along a flat interface (Chiu 1999a; 2004; Chiu et al. 2004). The system is attached to a set of Cartesian coordinate axes on the interface. The x and y axes are parallel with the interface, while the z axis is perpendicular to the interface. The z axis is taken to be in the [001] direction of the film material of the SK system.

The film and the substrate are elastically similar materials characterized by Young's modulus E and Poisson's ratio ν. The film and the substrate are subject to a mismatch

strain $\mathcal{E}_0$ between them, which results in deformation and strain energy in the system (Gao 1994). The strain energy is the driving force for the nanostructure formation; the characteristic strain energy density $w_{\sigma 0}$ is given by $w_{\sigma 0} = E(1+\nu)\mathcal{E}_0^2/2(1-\nu)$.

In addition to the strain energy, the system is also affected by the film-substrate interaction energy and the film surface energy. The interaction accounts for the SK transition and the development of the wetting layer (Chiu 1999a; Chiu and Gao 1995; Tersoff 1991). The interaction can be modeled as a special type of film surface energy of which the density g varies with the distance z between the film surface and the film-substrate interface (Chiu 1999a; Chiu and Gao 1995). If the interaction is caused by the quantum confinement, g is given by $g(z) = g_0 l/(z+l)$ where g_0 and l are material properties (Chiu 1999a; Suo and Zhang 1998). Similar phenomenological models for the interaction, also termed the wetting interaction or wetting potential can be found in the literature (Daruka and Barabasi 1997; Eisenberg and Kandel 2000; Kukta and Freund 1997; Ortiz et al. 1999; Spencer 1999; Spencer and Tersoff 1997).

The surface energy density γ is assumed to be a constant γ_0 except in the vicinity of the local minimum,

$$\gamma = \gamma_0 - \sum_j \Delta\gamma_j \exp\left(\eta_j |\mathbf{n} - \mathbf{n}_j|^2\right), \tag{2.1}$$

where $\mathbf{n}$ is the normal vector of the film surface, $\mathbf{n}_j$ is the orientation of the jth local minimum, $\Delta\gamma_j$ is the depth, and η_j controls the curvature of the minimum. The directions of $\mathbf{n}_j$ are taken to be {105}, {15 3 23}, and {113}, the facet orientations of the islands on the SiGe/Si system (Ross et al. 1999). In addition to the facet orientations, the surface energy density γ may also include a shallow minimum on {001} (Chiu 1999a; Rastelli et al. 2003; Tersoff et al. 2002). The shallow minimum affects the normalized effective surface energy density α of the flat film (Chiu 1999a; Chiu et al. 2004),

$$\alpha = \frac{\gamma_1 + K}{\gamma_0}, \tag{2.2}$$

where $\gamma_1 = \gamma$ at $\phi = 0$, $K = \partial^2\gamma/\partial\phi^2$ at $\phi = 0$, and ϕ is the angle between the vertical direction $\mathbf{e}_z$ and the normal vector $\mathbf{n}$ of the surface. For convenience, the normalized effective surface energy density α is shortened to the NESE density in the thesis.

The SK systems considered here are characterized by two characteristic lengths, L and $\hat{g}_0 l$, given by

$$L = \frac{\gamma_0}{w_{\sigma 0}}, \tag{2.3}$$

$$\hat{g}_0 l = \frac{g_0 l}{\gamma_0}, \tag{2.4}$$

The quantity L represents the length scale at which the strain energy reduction due to island formation is balanced by the corresponding surface energy increment. Typical values of L used in this thesis are 16000, 4000, 1000, 250, and 62.5 Å, roughly corresponding to the $Si_{1-x}Ge_x/Si$ systems with $x = 0.0625$, 0.125, 0.25, 0.5, and 1, respectively. The quantity $\hat{g}_0 l$, on the other hand, is the length scale associated with the interaction energy and the surface energy. In this study, l is assumed to be 1 Å, and $\hat{g}_0$ varies from 0.25, 0.0625, to 0.0156.

In most of the cases, the islands may undergo the coarsening process during which larger islands keep growing at the expense of smaller ones. The stability of the faceted islands against the coarsening process is determined by the sign of the stability number Σ (Chiu 2004),

$$\Sigma = \sqrt{\frac{\hat{g}_0 l U_0 \mathcal{S}}{L}} - \frac{\gamma_1 G}{\gamma_0}, \tag{2.5}$$

where $G = -1 + \gamma_2/\gamma_1 \cos\phi$, ϕ is the facet angle, and γ_2 is the surface energy density of the facet. If $\Sigma > 0$, stable island arrays exist, and the system will evolve toward the arrays. If $\Sigma < 0$, in contrast, the faceted islands are unstable against coarsening. The systems with $\Sigma < 0$ are called the coarsening SK systems throughout this thesis.

2.1.2 The surface chemical potential χ

The thermodynamics of the film surface is determined by the surface chemical potential χ (Chiu 1999a; Herring 1950; Leo and Sekerka 1989; Rice and Chuang 1981),

$$\chi = \mu_0 + \Omega \left[w_\sigma - (g+\gamma)\kappa + \frac{\partial g}{\partial z} n_z + \nabla^\Gamma \cdot \frac{\partial \gamma}{\partial \mathbf{n}} \right], \tag{2.6}$$

where μ_0 is the chemical potential of the film material without stress, Ω is the atomic volume, w_σ is the strain energy density, κ is the curvature, ∇^Γ is the surface gradient operator, and n_z is the z component of $\mathbf{n}$.

The physical meanings of the five terms in Eq. (2.6) are briefly discussed as follows. The first term μ_0 in Eq. (2.6) is the energy change when ignoring the effects of the stresses and the surface. This term is a constant when the film composition remains homogeneous. The second term Ωw_σ is responsible for the effect that the total strain energy of the film-substrate system decreases as a flat film surface develops into a rough profile (Asaro and Tiller 1972; Srolovitz 1989; Tersoff and Tromp 1993). Hence, the second term describes an energetic force favoring surface undulation and nanostructure formation. The third term $-\Omega(g+\gamma)\kappa$ is due to a change of the surface area (Herring 1950), and evidently this term impedes the development of islanded surfaces. The fourth term accounts for the variation of the interaction energy with the film thickness (Chiu 1999a; Chiu and Gao 1995), and including this term is crucial for modeling the SK transition and the formation of the wetting layer. The last term measures the surface energy variation due to the change of the surface orientations; this term determines the orientations of the facets that can form during the morphological evolution (Chiu 1999a; Leo and Sekerka 1989).

2.1.3 The morphological evolution driven by surface diffusion

The variation of χ on the film surface causes the morphological evolution of the system; the evolution controlled by surface diffusion is expressed as (Asaro and Tiller 1972; Mullins

1957)

$$\frac{\partial f(x,y,t)}{\partial t} = \frac{\Omega \rho_s D_s}{n_z k_B T_k} \nabla^\Gamma \cdot (\nabla^\Gamma \chi), \tag{2.7}$$

where $f(x,y,t)$ is the film surface profile at time t, ρ_s is the adatom density, D_s is the surface diffusivity, k_B is the Boltzmann constant, and T_k is the temperature. The surface diffusion mechanism is mass-conserved; it is the dominating kinetic mechanism of the morphological evolution of the SK systems during the annealing process.

The implementation of the morphological evolution simulation is similar to those in our previous works (Chiu 1999a; 2004; Chiu et al. 2004). The simulation employed the two-dimensional Fourier series with the same wavelength in the x and y directions to describe the film surface profile $f(x,y,t)$. The wavelength of the Fourier series defined the calculation cell size. The simulation consisted of three basic modules for determining the evolution of the surface profile $f(x,y,t)$. The first module evaluated χ expressed in Eq. (2.6). In particular, the last three terms in Eq. (2.6) are calculated by the fast Fourier transform method, while the term w is obtained by using the high-order boundary perturbation method to solve the elasticity problem of a strained film on a thick substrate (Chiu 1999a). The second module then used the result χ to compute the surface migration rate $\partial f(x,y,t)/\partial t$ according to the Eq. (2.6). Finally, the third module integrated the surface migration rate $\partial f(x,y,t)/\partial t$ with respect to time t by the generalized mid-point rule (Hughes 1987) to update the surface profile $f(x,y,t)$. The simulation results are normalized by the time scale $t_L = k_B T_k L^4/\rho_s D_s \Omega^2 \gamma_0$. Our simulation lacked the capability to produce perfect facets. Nevertheless, the term facet is loosely used in the thesis when describing the simulation results.

2.2 SK System with Electric Field

Similar to typical SK systems, the morphological evolution of the SK system under an electric field (EMSO) is still dictated by Eq. (2.6). The key change in the current case is

the expression for the surface chemical potential χ, which needs to take into account the effects of the electric field on the SK system (Du and Srolovitz 2004),

$$\chi = \mu_0 + \Omega \left[w_\sigma - w_e - (g+\gamma)\kappa + \frac{\partial g}{\partial z} n_z + \nabla^\Gamma \cdot \frac{\partial \gamma}{\partial \mathbf{n}} \right], \tag{2.8}$$

where w_e is the electrostatic energy density. The opposite signs associated with the w_σ and ω_e can be understood as follows.

When the surface moves along the normal vector direction $\mathbf{n}$, the volume of the film increases and the volume of the vacuum decreases. The increase of film volume means that the strain energy stored in the film system also rises, and this explains the positive sign of the term w_σ in Eq. (2.8). On the other hand, the decrease of the vacuum volume suggests the electrostatic energy in the vacuum reduces and this shows why the sign of the term ω_e is negative.

The simulation scheme for solving Eq. (2.8) is similar to those in the literature (Chiu 2004; Chiu et al. 2004). The results are still normalized by the same characteristic time $t_L = k_B T_k L^4 / \rho_s D_s \Omega^2 \gamma_0$ as that defined earlier in Sec. 2.1 .

Chapter 3

Energy Analysis

This chapter summarizes the first-order boundary perturbation method for evaluating the total energy change due to the formation of strained nanostructures on the SK film-substrate system under the condition of mass conservation. For simplicity, the discussion is limited to the two-dimensional (2D) cases, and the total energy is the sum of the strain energy, surface energy, interaction energy and electrostatic energy with the presence of electric field. The change of the strain energy ΔW_σ is discussed in Sec. 3.2, that of the electrostatic energy ΔW_e is derived in Sec. 3.2, that of the interaction energy is examined in Sec. 3.3, and that of the surface is shown in Sec. 3.4.

3.1 Strain Energy

This section summarizes the first-order perturbation method for determining the strain energy change due to the formation of a nanostructure. The section is divided into three parts. The first one examines the case of a single nanostructure. The second one explores the situation where a new nanostructure develops at a site adjacent to a pre-existing one. Based on the results of the second part, the third one considers the scenario that the new adjacent structure is much smaller than the preexisting one.

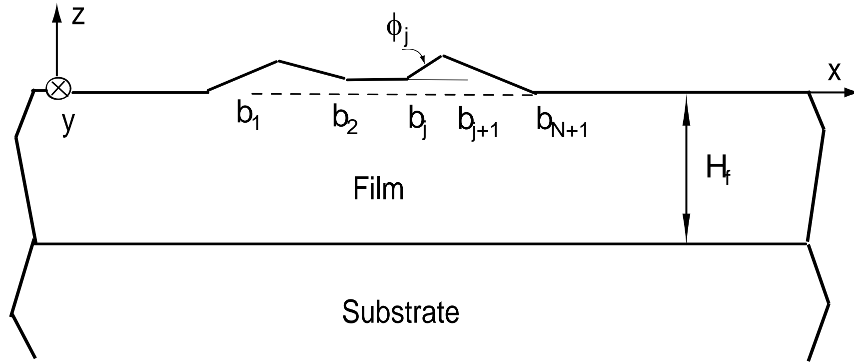

Figure 3.1: Schematic diagram of a heteroepitaxial film-substrate system containing a faceted nanostructure on a flat wetting layer of thickness H_f.

3.1.1 A single nanostructure

System

Figure 3.1 depicts the morphology of a 2D strained film-substrate system that may appear during the deposition/annealing process. The system is attached by a set of Cartesian coordinate axes on the flat film surface. Similar to the convention adopted in Sec. 3.1, the x and y axes lie parallel with the surface, while the z axis is normal to the surface.

The substrate of the system is a semi-infinite solid, and the film consists of a flat wetting layer of thickness H_f and a nanostructure with N facets. There are totally $N + 1$ vertices on the structure; the x components of the vertices are denoted as $\mathcal{B} = \{b_1, b_2, \ldots, b_{N+1}\}$. The angle between the jth facet and the x direction is ϕ_j. For convenience, one of the angles, denoted as ϕ^*, is chosen to define the characteristic slope $\mathcal{S} = \tan \phi^*$ of the structure. The ratio between the slope of the jth facet and the characteristic value $\mathcal{S}$ gives the relative slope m_j of the facet, i.e., $m_j = \tan \phi_j / S$.

Strain energy change

The strain energy change ΔW_σ due to the formation of the nanostructure can be estimated by the first-order perturbation method, assuming the total film volume is conserved during the formation process and the slope $\mathcal{S}$ is small (Chiu and Poh 2005; Daruka et al. 1999; Tersoff and Tromp 1993) The starting point of the method is to determine the strain

energy density $w_\sigma(x)$ on the islanded film surface (Chiu and Poh 2005; Daruka et al. 1999),

$$w_\sigma(x) = w_{\sigma 0}^{3d} - 2w_{\sigma 0}\mathcal{S}\Psi_\sigma(x), \tag{3.1}$$

where $w_{\sigma 0}^{3d} = 2w_{\sigma 0}/(1+\nu)$ is the strain energy density of the flat strained film, and the function $\Psi_\sigma(x)$ describes the variation of $w_\sigma(x)$ on the film surface due to the nanostructure,

$$\Psi_\sigma(x) = -\frac{2}{\pi}\sum_{j=1}^{N} m_j \Re\left[\ln\frac{x-b_{j+1}}{x-b_j}\right]. \tag{3.2}$$

The symbol $\Re$ in Eq. (3.2) denotes the real part of a complex number. Equation (3.1) is accurate to the first order of $\mathcal{S}$.

The result of $w_\sigma(x)$ is used in the following formula to describe the variation of the strain energy ΔW_σ of the system with that of the surface profile $\delta f(x)$ (Chiu and Poh 2005; Eshelby 1970; Rice 1968),

$$\Delta W_\sigma = \int_{\mathcal{B}} w_\sigma(x)\delta f(x)dx. \tag{3.3}$$

As shown in Fig. 3.1, the island morphology can be obtained by changing the characteristic slope $\mathcal{S}$ but fixing the wetting layer thickness h, the island base, the facets relative slope m. When $\mathcal{S} = 0$, the morphology is a flat film; as $\mathcal{S}$ increases, an island is added gradually onto the wetting layer. The morphological evolution δf during the process can be expressed as

$$\delta f(x) = \mathcal{F}(x)\delta\mathcal{S}, \tag{3.4}$$

where $\mathcal{F}(x) = f(x)/\mathcal{S}$ is the shape function of the island.

According to Eq. (3.4), the total film volume increases during the morphological evolution. Therefore, the strain energy change during the process will include the change

due to the volume increment and that due to the island shape change as shown below.

By substituting Eq. (3.1) and Eq. (3.4) into Eq. (3.3), we have

$$\frac{dWs}{d\mathcal{S}} = w_{\sigma 0}^{3d} \int_{\mathcal{B}} \mathcal{F}(x)dx - 2w_{\sigma}\mathcal{S} \int_{\mathcal{B}} \Psi_{\sigma}(x).\mathcal{F}(x)dx \tag{3.5}$$

Carrying out the integral in Eq. (3.5) and evoking the solution procedure outlined in (Chiu and Poh 2005) determine the strain energy change ΔW_{σ} to be

$$\Delta W_{\sigma} = -w_{\sigma 0}\mathcal{S}VU_{\sigma}, \tag{3.6}$$

where V is the volume of the structure and U represents the effect of the nanostructure shape on ΔW_{σ},

$$U_{\sigma} = \frac{1}{V} \int \Psi_{\sigma}(x) f(x) dx. \tag{3.7}$$

The quantity U_{σ} has the unique property that U_{σ} remains the same when the nanostructure enlarges self-similarly.

Equation (3.7) is valid for two-dimensional cases. The formula for 3D cases can be found in Chiu and Poh (2005); it is found that the formula is similar except that $\Psi_{\sigma} = \Psi_{\sigma}(x, y)$ is a function of x and y and the integration becomes areal integrals instead of the line integral in Eq. (3.7). By using formula for the 3D cases, Chiu et al (2005) determined the strain energy change due to the formation of a square-based pyramid island to be

$$\Delta W_{\sigma} = -\frac{1}{6} U_{3D} w_{\sigma 0} \tan^2\phi D^3, \tag{3.8}$$

where $U_{3D} = 1.98$ and D is the width of the pyramid base.

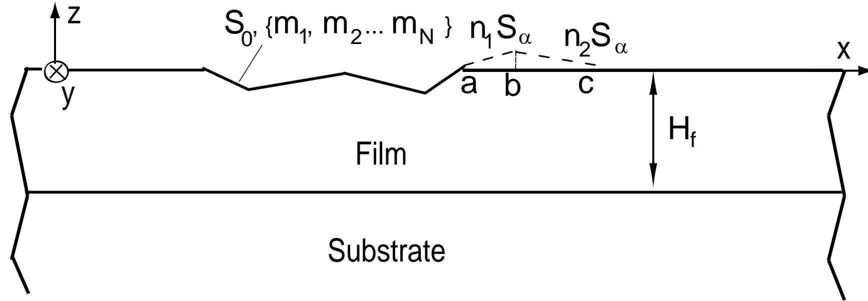

Figure 3.2: Schematic diagram of a nanostructure developing at the adjacent site of a preexisting one with N facets. The adjacent structure is illustrated by the dashed line, while the preexisting one by the solid line.

3.1.2 An adjacent nanostructure

System

Figure 3.2 illustrates the case considered in this section where a nanostructure (denoted by the dashed line) develops at the adjacent site of a preexisting one (denoted by the solid line). The preexisting nanostructure contains N facets with the characteristic slope being $\mathcal{S}_0$; the last vertex at the right edge of the nanostructure is located at $x = a$ and $z = 0$. In comparison, the adjacent nanostructure includes two surfaces. The slopes of the surfaces are $n_1\mathcal{S}_\alpha$ and $n_2\mathcal{S}_\alpha$, respectively, and $\mathcal{S}_\alpha$ is the corresponding characteristic slope. There are three vertices on the adjacent nanostructure. The first vertex is at the same location as the last vertex of the preexisting structure, the second one is at $x = b$ and $z = n_1\mathcal{S}_\alpha(b - a)$, and the third one is at $x = c$ and $z = 0$.

Strain energy change

It follows from Eq. (3.3) that the strain energy density on the film surface containing the preexisting and the adjacent nanostructures can be expressed as

$$w_\sigma(x) = {w_\sigma}_0^{3d} - 2w_{\sigma 0}\mathcal{S}_0\Psi_0(x) - 2w_{\sigma 0}\mathcal{S}_\alpha\Psi_\alpha(x), \tag{3.9}$$

accurate to the first order of $\mathcal{S}_0$ and $\mathcal{S}_\alpha$. In Eq. (3.9), $\Psi_0(x)$ describes the variation of $w_\sigma(x)$ due to the preexisting nanostructure and $\Psi_\alpha(x)$ illustrates that due the adjacent one. Both Ψ_0 and Ψ_α can be obtained by employing Eq. (3.2). For example, Ψ_α can be found to be

$$\Psi_\alpha(x) = -\frac{2}{\pi}\left(n_1 \ln\frac{x-b}{x-a} + n_2 \ln\frac{x-c}{x-b}\right). \tag{3.10}$$

Similar to the solution procedure for deriving ΔW_σ of a single nanostructure, Eq. (3.9) can be substituted into Eq. (3.6) to evaluate the variation of the strain energy of the system when the characteristic slope $\mathcal{S}_\alpha$ of the adjacent nanostructure increases gradually from 0 to $\mathcal{S}_\alpha$ with other parameters of the system being fixed, including $\mathcal{S}_0$ and the total mass of the film. The result can be written as (Chiu and Poh 2005),

$$\Delta W_\sigma = -2w_{\sigma 0}\mathcal{S}_0 V U_0 - w_{\sigma 0}\mathcal{S}_\alpha V U_\alpha, \tag{3.11}$$

where V is the volume of the adjacent nanostructure, and U_0 and U_α are given by

$$U_k = \frac{1}{V}\int_{\mathcal{B}} \Psi_k(x) f(x) dx. \tag{3.12}$$

In Eq. (3.12), the subscript k can be 0 or α, and $f(x)$ refers to the surface profile of the adjacent nanostructure. The quantities U_0 and U_α represent the effects of the shapes of the preexisting and adjacent nanostructures on ΔW_σ, respectively.

3.1.3 A small adjacent nanostructure with the same facet as the pre-existing one

This section examines the special case where the adjacent nanostructure is small and its first facet is the same as the last one of the preexisting structure, i.e., $n_1\mathcal{S}_\alpha = m_N\mathcal{S}_0$. The strain energy change can be examined by two approaches.

The first approach for calculating ΔW_σ

Since the adjacent structure is small, the function $\Psi_0(x)$ associated with the preexisting nanostructure in the vicinity of $x = a$ can be rewritten as the sum of the contribution from the vertex at $x = a$, denoted as $\Psi_a(x)$, and a constant Ψ_c representing the contribution from the remaining vertices,

$$\Psi_0(x) = \Psi_c + \Psi_a(x), \tag{3.13}$$

where Ψ_c and $\Psi_a(x)$ can be expressed as

$$\begin{aligned} \Psi_a(x) &= -\frac{2m_N}{\pi}\ln(x-a), &(3.14)\\ \Psi_c &= \lim_{x\to a}\left[\Psi_0(x) - \Psi_a(x)\right]. &(3.15) \end{aligned}$$

Substituting Eqs. (3.10) and (3.13) into (3.11) and (3.12), employing the identity $(c-b)n_2 + (b-a)n_1 = 0$, and evoking the condition $n_1\mathcal{S}_\alpha = m_N\mathcal{S}_0$ yield ΔW_σ for the special case considered here,

$$\Delta W_\sigma = -2w_{\sigma 0}\mathcal{S}_0\Delta V\left\{\Psi_c + \frac{m_N}{\pi}\left[3 - 2\ln(c-b)\right]\right\}, \tag{3.16}$$

where ΔV can be calculated to be

$$\Delta V = \frac{1}{2}\mathcal{S}_\alpha(n_1 - n_2)(c-b)(b-a). \tag{3.17}$$

The second approach for calculating ΔW_σ

In addition to the solution procedure described in Eqs. (3.1)–(3.7), the strain energy change due to the formation of an adjacent nanostructure can also be given by the difference between the strain energy of the system containing both the preexisting and the adjacent structures and that containing the preexisting one only. i.e., $\Delta W_\sigma = W_\sigma - W_{\sigma 0}$, where $W_{\sigma 0}$ is the strain energy of the system with the preexisting structure and W_σ is

that with both preexisting and the adjacent ones.

The procedure for evaluating the quantity W_σ starts with the function $\Psi(x)$ for the nanostructure,

$$\Psi_\alpha(x) = -\frac{2}{\pi}\left[\ln\left(\frac{x^2-b^2}{x^2}\right) - n\ln\left(\frac{x^2-c^2}{x^2-b^2}\right)\right]. \tag{3.18}$$

Substituting $\Psi(x)$ into Eqs. (3.6) and (3.7) leads to

$$W_\sigma = -w_0\mathcal{S}\int_{-c}^{c}\Psi(x)f(x)dx, \tag{3.19}$$

where $f(x)$ expresses the shape of the pit-ridge structure. The integral in Eq. (3.19) is divided into four ranges, $[-c,-b]$, $[-b,0]$, $[0,b]$, and $[b,c]$, corresponding to the four facets of the pit-ridge structure. Since the structure is symmetric, the results of the first and the second ranges are equal to those of the fourth and the third ranges, respectively. Accordingly, Eq. (3.19) can be reduced to

$$W_\sigma = -2w_0\mathcal{S}\left[\int_0^b f_3(x)\Psi(x)dx + \int_b^c f_4(x)\Psi(x)dx\right], \tag{3.20}$$

where $f_3(x) = \mathcal{S}(x-a)$ describes the third facet in the range $[0,b]$, and $f_4(x) = -n\mathcal{S}(x-c)$ is for the fourth facet in $[b,c]$.

The integral in Eq. (3.20) can be calculated analytically by the computer program *Mathematica*^{TM}. The result, though extremely lengthy, can be significantly simplified by evoking the following Taylor series expansion

$$\ln(1+t) = t - \frac{t^2}{2} + o(t^3), \tag{3.21}$$

under the condition $t \ll 1$.

Deducting $W_{\sigma 0}$ from the simplified expression yields the same formula in Eq. (3.16), which is derived from the solution procedure described in Eqs. (3.1)–(3.7). The agreement confirms the validity of the procedure presented in Sec. 3.1.3 for determining the strain

energy change due to the formation of an adjacent nanostructure.

3.2 Electrostatic Energy

In this section, we investigate the two-dimensional case where a conducting film containing a faceted nanowire on its surface is exposed to a patterned electrode with a dielectric media between the film and the electrode. Our approach is similar to those for solving the elasticity problems of strained and faceted wires on a flat film (Chiu and Poh 2005; Gao 1991a; Tersoff and Tromp 1993). The result is accurate to the first order of the slopes of the nanowire and the pattern, and the result is valid for the case of conducting films.

3.2.1 Problem statement

System

Figure 3.3 depicts a 2D system consisting of a thick substrate, a thin conductor film, a dielectric media of thickness H_v on top of the film along the surface Γ_1, and an electric plate in contact with the dielectric media along the surface Γ_2. The electric plate and the film are connected by a battery with the voltage difference fixed at $\Delta\Phi$.

The conductor film of the system contains a nanowire with N facets. The wire is similar to that considered in Fig. 3.1, characterized by the slope $\mathcal{S}_0$, the relative slopes of the facets $\{m_1, m_2, \ldots, m_N\}$, and the x-components of the vertices $\mathcal{B}$.

In addition to the nanostructure on the film surface Γ_1, the system also exhibits a $\mathcal{N}$-facet pattern on the electric plate surface Γ_2. The geometry of the pattern can be fully described by the characteristic slope $\mathcal{S}_e$ of the pattern, the relative slopes of the $\mathcal{N}$ facets $\{l_1, l_2, \ldots, l_{\mathcal{N}}\}$, and the x components of the vertices on the pattern $\{t_1, t_2, \ldots, t_{\mathcal{N}+1}\}$.

The electrostatics problem

The voltage difference $\Delta\Phi$ generated by the battery causes variation of potential Φ in the dielectric media. The potential Φ is determined by the Laplace equation $\nabla^2\Phi = 0$ and

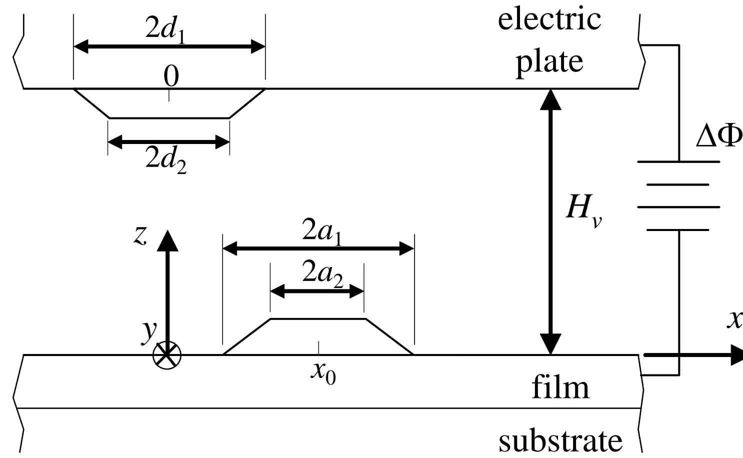

Figure 3.3: Schematic diagram of conducting film-substrate system under the influence of an electric field.

the boundary conditions that on Γ_1,

$$\Phi = 0, \tag{3.22}$$

and on Γ_2,

$$\Phi = \Delta\Phi. \tag{3.23}$$

The governing equation and the boundary conditions on Γ_1 and Γ_2 define the 2D electrostatics problem considered in this thesis.

When both Γ_1 and Γ_2 are flat, the solution to the electrostatics problem is found to be

$$\Phi_0(x, z) = E_0 z, \tag{3.24}$$

where $E_0 = \Delta\Phi/H_v$ is the magnitude of the electric field. The electrostatic energy density of this special case is given by $w_{e0} = \epsilon E_0^2/2$, where ϵ is the permittivity of the dielectric

media.

When nanostructures are present on Γ_1 and Γ_2, the solution can be expressed as

$$\Phi(x, z) = \Phi_0(x, z) + \Phi_\Gamma(x, z), \tag{3.25}$$

where $\Phi_\Gamma(x, z)$ are the potential induced by the structures on Γ_1 and Γ_2. Substituting Eqs. (3.24) and (3.25) into (3.22) yields the boundary condition for Φ_Γ on Γ_1,

$$\Phi_\Gamma(x, f) = -\mathcal{S}E_0\hat{f}(x). \tag{3.26}$$

By following a similar procedure, the boundary condition for Φ_Γ on Γ_2 can be determined to be

$$\Phi_\Gamma(x, H_v + g) = -\mathcal{S}_e E_0\hat{g}(x). \tag{3.27}$$

3.2.2 The complex-variable method

The complex-variable potential

The solution of the 2D Laplace equation can be expressed in terms of a complex-variable function,

$$\Phi = \Re\left[\psi(\zeta)\right], \tag{3.28}$$

where $\zeta = x + iz$, and $i = \sqrt{-1}$. By employing the general expression for Φ and evoking the change of variable,

$$\frac{\partial}{\partial x} - i\frac{\partial}{\partial z} = 2\frac{\partial}{\partial \zeta}, \tag{3.29}$$

the electric field $E = E_x + iE_z$ and the electrostatic energy density w_e can be determined to be

$$E = \overline{\psi'(x)}, \tag{3.30}$$

$$w_e = \frac{\epsilon}{2}\Re\left[\psi'(x)\overline{\psi'(x)}\right], \tag{3.31}$$

where ϵ is the electric permittivity of the dielectric media.

The complex-variable potential $\psi_0(\zeta)$ corresponding to the special solution $\Phi_0(\mathbf{x})$ expressed in Eq. (3.24) can be found to be

$$\psi_0(\zeta) = -iE_0\zeta. \tag{3.32}$$

Green's functions

Before proceeding to the perturbation analysis, it is helpful to discuss the Green's functions that are employed later in the thesis. The first one is the solution to the problem shown in Fig. 3.4(a) where two flat electrodes are separated by a distance of H_v. The potential on the upper electrode $z = H_v$ is zero. The potential on the bottom electrode $z = 0$ is also zero in the range $x < s$, while $\Phi = 1$ in the range $x > s$.

The first step to solve the problem is to map the stripe between the two electrodes to the upper half space in the ω plane by the function,

$$\omega = \exp\left[\eta(\zeta - s)\right], \tag{3.33}$$

where $\eta = \pi/H_v$. The mapping can be visualized in Fig. 3.4(b), which indicates the six points in the ζ planes, namely, $\zeta_A = s$, $\zeta_B = \infty$, $\zeta_C = \infty + iH_v$, $\zeta_D = s + iH_v$, $\zeta_E = -\infty + iH_v$, and $\zeta_F = -\infty$, are mapped onto $\omega_A = 1$, $\omega_B = \infty$, $\omega_C = -\infty$, $\omega_D = -1$, $\omega_E = 0$, and $\omega_F = 0$, respectively, in the ω plane.

It follows from the mapping shown in Fig. 3.4 that the boundary conditions on $z = 0$ and $z = H_v$ can be rewritten as $\Phi = \Re[\psi] = 1$ on the line between ω_A and ω_B and

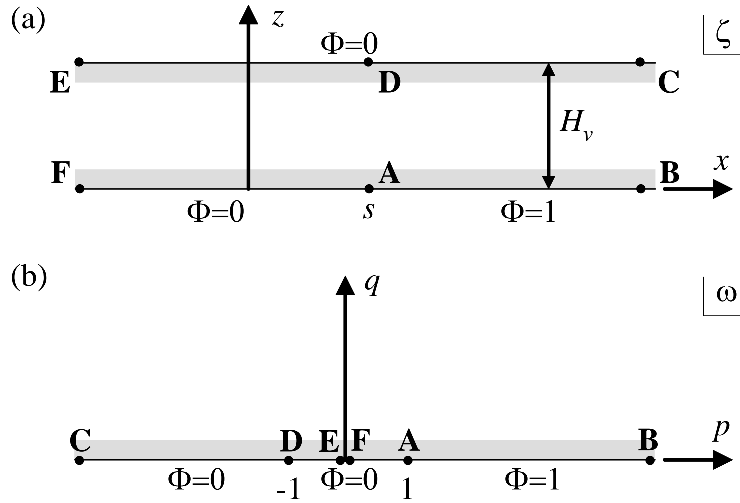

Figure 3.4: (a) Schematic diagram of two flat electrodes with $\Phi = 0$ on the upper electrode and $\Phi = 0$ and 1 on the lower electrode in the range $x < s$ and $x > s$, respectively. (b) The stripe between $0 \leq z \leq H_v$ is mapped on the upper half plane by the function $\omega = \exp[\eta(\zeta - s)]$

$\Phi = \Re[\psi] = 0$ on the line between ω_C and ω_A. The complex-variable function ψ_b satisfying the condition can be found to be

$$\psi_b = 1 + i\pi^{-1}\ln(\omega - 1). \tag{3.34}$$

Replacing ω in the solution with the function given in Eq. (3.33) yields the Green's function for the electrostatics problem illustrated in Fig. 3.4(a),

$$\psi_b(\zeta, s) = \frac{i}{\pi}\left[e^{\eta(\zeta - s)} - 1\right] + 1. \tag{3.35}$$

The first Green's function can be employed to write down the general solution to the problem where $\Phi = 0$ on the top flat electrode and $\Phi = h(x)$ on the bottom flat electrode,

$$\psi(\zeta) = \int \psi_b(\zeta, s) h_b'(s) ds. \tag{3.36}$$

Equation (3.36) is useful when examining the cases of faceted wires on the film surface.

The second Green's function refers to the solution to the two-electrode problem plotted in Fig. 3.5(a) where $\Phi = 0$ on the bottom surface $z = 0$, and on the upper surface

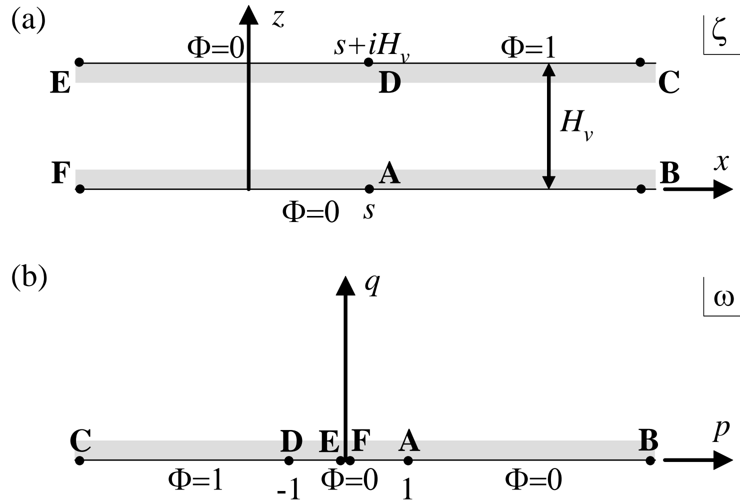

Figure 3.5: (a) Schematic diagram of two flat electrodes with $\Phi = 0$ on the lower electrode and $\Phi = 0$ and 1 on the upper electrode in the range $x < s$ and $x > s$, respectively. (b) The stripe between $0 \leq z \leq H_v$ is mapped on the upper half plane by the function $w_\sigma = \exp[\eta(\zeta - s)]$

$z = H_v$, $\Phi = 0$ in the range $x < s$ and $\Phi = 1$ in the range $x > s$. The solution procedure for deriving the Green's function of the current case is identical to that of the first one. (1) Map the stripe between the two surfaces $z = 0$ and $z = H_v$ onto the upper half space of the ω plane by the function expressed in Eq. (3.33). (2) Express the boundary conditions on the ω plane: $\Re[\psi] = 1$ on the line between ω_C and ω_D, and $\Re[\psi] = 0$ on that between ω_D and ω_B, see Fig. 3.5(b). (3) Write down the analytical solution on the ω plane that satisfies the boundary condition: $\psi_t(\omega) = -i\pi^{-1}\ln(\omega + 1)$. (4) Substituting the mapping function $\omega(\zeta)$ given in Eq. (3.33) into the solution yields the second Green's function,

$$\psi_t(\zeta, s) = -\frac{i}{\pi}\ln\left[e^{\eta(\zeta - s)} + 1\right]. \tag{3.37}$$

Similar to the first case, the second Green's function can be used to write down the general solution to the problem where $\Phi = 0$ on $z = 0$ and $\Phi = h(x)$ on $z = H_v$,

$$\psi(\zeta) = \int \psi_t(\zeta, s)h_t'(s)ds. \tag{3.38}$$

The result is applied later to the cases involving a patterned electrode.

3.2.3 The first-order perturbation analysis

General expression for the first-order perturbation solution

The electrostatics problem given in Eqs. (3.26) and (3.27) can be significantly simplified by assuming that the characteristic slopes $\mathcal{S}$ and $\mathcal{S}_e$ are small. Under the assumption, the weak singularities due to the vertices on the nanostructures can be neglected (Tersoff and Tromp 1993), and the function $\Phi_\Gamma(x,z)$ can be expressed as

$$\Phi_\Gamma(x,z) = \mathcal{S}E_0\Phi_1(x,z) + \mathcal{S}_eE_0\Phi_2(x,z), \tag{3.39}$$

accurate to the first order of $\mathcal{S}$ and $\mathcal{S}_e$. In Eq. (3.39), Φ_1 refers to the effects of the wire on Φ, and Φ_2 describes the corresponding pattern effect. Substituting $z = f(x)$ into Eq. (3.39) leads to Φ_Γ on the film surface. Expressing the result by Taylor series expansion about $z = 0$ and neglecting the terms involving higher order terms of $\mathcal{S}$ and $\mathcal{S}_e$ yield

$$\Phi_\Gamma(x,f) = \mathcal{S}E_0\Phi_1(x,0) + \mathcal{S}_eE_0\Phi_2(x,0). \tag{3.40}$$

By employing a similar scheme, Φ_Γ on the pattern surface $z = H_v + g(x)$ can be estimated to be

$$\Phi_\Gamma(x,H_v+g) = \mathcal{S}E_0\Phi_1(x,H_v) + \mathcal{S}_eE_0\Phi_2(x,H_v). \tag{3.41}$$

Both Eqs. (3.40) and (3.41) are accurate to the first order of $\mathcal{S}$ and $\mathcal{S}_e$.

Substituting Eqs. (3.40) and (3.41) into (3.26) and (3.27) and noticing that $\mathcal{S}$ and $\mathcal{S}_e$ are two independent parameters of the system determine the boundary conditions for Φ_1,

$$\Phi_1(x,0) = -\hat{f}(x), \qquad \Phi_1(x,H_v) = 0, \tag{3.42}$$

and those for Φ_2,

$$\Phi_2(x,0) = 0, \qquad \Phi_2(x,H_v) = -\hat{g}(x). \tag{3.43}$$

Equation (3.42) suggests, accurate to the first order of $\mathcal{S}$ and $\mathcal{S}_e$, the boundary conditions for $\Phi_1(x, z)$ can be written as a distribution of electrostatic potential $-\hat{f}(x)$ on the flat surface $z = 0$. Similarly, Eq. (3.43) shows that the boundary conditions for $\Phi_2(x, z)$ can be represented by the potential distribution $-\hat{g}(x)$ on $z = H_v$.

The electrostatics problem described by the boundary conditions given in Eqs. (3.41) and (3.42) can be solved by using the two Green's functions, ψ_b and ψ_t, discussed in Sec. 3.2.2 to calculate the complex-valued function ψ_Γ due to the non-flat boundaries. Summing the results and the special solution $\psi_0(\zeta)$ expressed in Eq. (3.33) yields the first-order perturbation solution of the system shown in Fig. 3.5,

$$\psi(\zeta) = \psi_0(\zeta) - iE_0\mathcal{S}\psi_1(\zeta) - iE_0\mathcal{S}_e\psi_2(\zeta) + O(\mathcal{S}_{max}^2), \tag{3.44}$$

where ψ_1 is the first-order term due to the wires on the film surface and ψ_2 is that due to the patterns on the electrode,

$$\psi_1(\zeta) = -\frac{1}{\pi}\int \left[\ln\left(e^{\eta(\zeta-s)} - 1\right) + 1\right] m(s)ds, \tag{3.45}$$

$$\psi_2(\zeta) = \frac{1}{\pi}\int \left[\ln\left(e^{\eta(\zeta-s)} + 1\right) + 1\right] l(s)ds. \tag{3.46}$$

In Eqs. (3.45) and (3.46), $m(s) = f'(s)/\mathcal{S}$ is the relative slope on the film surface, and $l(s) = g'(s)/\mathcal{S}_e$ is that on the patterned electrode.

The surface electrostatic energy density

It follows from Eqs. (3.43), (3.45), and (3.46) that the derivative $\psi'(\zeta)$ on the film surface $\zeta_\Gamma = x + if(x)$ can be written as

$$\psi(\zeta_\Gamma) = -iE_0\left[1 + \mathcal{S}\psi_1'(x) + \mathcal{S}_e\psi_2'(x)\right]. \tag{3.47}$$

Substituting the expression into Eq. (3.45) and ignoring the high-order terms yields the electrostatic energy density w_e on the film surface accurate to the first order of $\mathcal{S}$ and $\mathcal{S}_e$,

$$w_e(\zeta_\Gamma) = w_{e0}\left[1 + 2\mathcal{S}\Psi_1(x) + 2\mathcal{S}_e\Psi_2(x)\right] + O(\mathcal{S}_{max}^2), \tag{3.48}$$

where $\Psi_1(x) = \Re[\psi_1'(x)]$, $\Psi_2(x) = \Re[\psi_2'(x)]$, and $w_{e0} = \epsilon E_0^2/2$ is the characteristic electrostatic energy density.

Equation (3.48) shows that the wire and the pattern cause the electrostatic energy density w_e on the film surface to deviate from the constant w_{e0} by $2\mathcal{S}w_{e0}\Psi_1(x)$ and by $2\mathcal{S}_e w_{e0}\Psi_2(x)$, respectively. The effects are proportional to the slopes of the wire and pattern, the density w_{e0}, and the two functions $\Psi_1(x)$ and $\Psi_2(x)$ that describes the variation of w_e on the film surface.

The two functions $\Psi_1(x)$ and $\Psi_2(x)$ are controlled by the relative slopes, m and l, of the wire and pattern, respectively. The two functions are independent of the electric permittivity ϵ of the dielectric media between the film and the electric plate and the slopes of the wires and patterns.

Analytic expressions for faceted wires and patterns

The integrals in Eqs. (3.45) and (3.46) cannot be calculated analytically in most of the cases. The two equations, however, can be employed to obtain concise results for the functions $\Psi_1(\zeta)$ and $\Psi_2(\zeta)$ when the wires and the patterns are faceted. The results are presented in this section.

We first consider $\psi_1'(\zeta)$ by differentiating Eq. (3.43) with respect to ζ and noticing that the integration can be divided into N intervals corresponding to the projections of the N facets of the wire on the plane $z = 0$,

$$\psi_1'(\zeta) = -\frac{\eta}{\pi}\sum_{j=1}^{N}\int_{b_j}^{b_{j+1}} \frac{m_j e^{\eta(\zeta - s)}}{e^{\eta(\zeta - s)} - 1} ds. \tag{3.49}$$

Carrying out the integral in Eq. (3.49) and taking the real part of the result lead to a simple expression for $\Psi_1(\zeta)$,

$$\Psi_1(\zeta) = -\frac{1}{\pi}\Re\left\{\sum_{j=1}^{N} m_j \ln\left[\frac{e^{\eta(\zeta-b_{j+1})}-1}{e^{\eta(\zeta-b_j)}-1}\right]\right\}. \tag{3.50}$$

Equation (3.50) determines the electric field due to the N-facet wire on the film surface. The expression is further reduced to

$$\Psi_1(\zeta) = -\frac{1}{\pi}\sum_{j=1}^{N} m_j \ln\left(\frac{\zeta-b_{j+1}}{\zeta-b_j}\right), \tag{3.51}$$

when $\eta\zeta = \pi\zeta/H_v \to 0$.

Turn to the function $\Psi_2(\zeta)$. The function can be calculated by employing the same solution procedure for $\Psi_1(\zeta)$, which leads to the following formula,

$$\Psi_2(\zeta) = \frac{1}{\pi}\Re\left\{\sum_{j=1}^{\mathcal{N}} l_j \ln\left[\frac{e^{\eta(\zeta-t_{j+1})}+1}{e^{\eta(\zeta-t_j)}+1}\right]\right\}. \tag{3.52}$$

Equations (3.50) and (3.52) are the first-order perturbation solutions for single wire and pattern containing multiple facets. The results are also applicable to the cases of multiple wires and patterns.

Examples

Equations (3.50) and (3.52) are applied to three special cases in this section, namely, the trapezoidal wire, the flat tape, and the trapezoidal pattern. Of particular interest here are the two functions, $\Psi_1(\zeta)$ and $\Psi_2(\zeta)$, of the three cases. As discussed earlier, the results can be further substituted into Eqs. (3.30) and (3.31) to calculate the electric filed $\mathbf{E}$ and the electrostatic energy density w_e in the system.

Trapezoidal wires

Figure 3.6(a) illustrates the details of the first case where a trapezoidal wire forms on a film surface. The center of the wire base is located at $x = x_0$. The characteristic

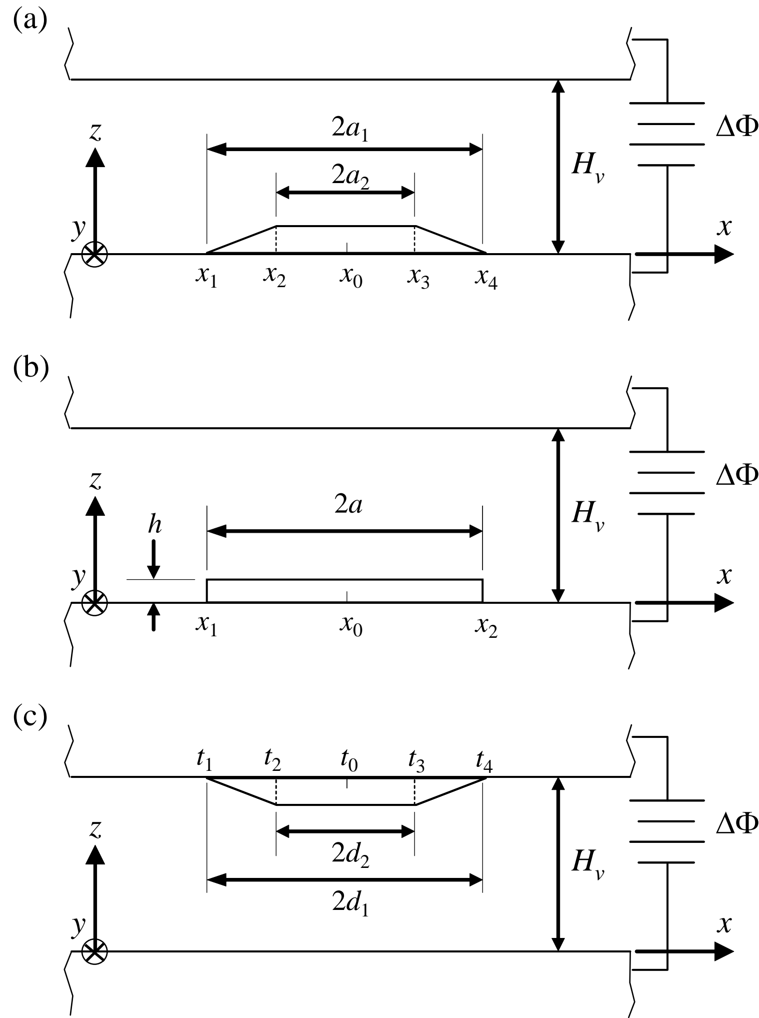

Figure 3.6: Schematic diagrams of a film-substrate structure under the influence of an electric plate containing (a) a trapezoidal wire on the film, (b) a flat tape on the film, and (c) a trapezoidal pattern on the electric plate.

slope of the structure is $\mathcal{S} = \tan\phi$, and the relative slopes of three facets of the wire are $\{1, 0, -1\}$. The width of the wire base is $2a_1$, that of the wire top surface is $2a_2$, and the x components of the wire vertices are $\{x_1, x_2, x_3, x_4\}$ where $x_1 = x_0 - a_1$, $x_2 = x_0 - a_2$, $x_3 = x_0 + a_2$, and $x_4 = x_0 + a_1$. Substituting the information into Eqs. (3.50) and (3.52) determines $\Psi_1(\zeta)$ and $\Psi_2(\zeta)$ of the current case to be $\Psi_2 = 0$ and

$$\begin{aligned}\Psi_1(\zeta) &= \frac{1}{\pi}\Re\left\{\ln\left[e^{\eta(\zeta-x_1)}-1\right]-\ln\left[e^{\eta(\zeta-x_2)}-1\right]\right. \\ &\quad \left.-\ln\left[e^{\eta(\zeta-x_3)}-1\right]+\ln\left[e^{\eta(\zeta-x_4)}-1\right]\right\}. \end{aligned} \tag{3.53}$$

When $|\eta(\zeta - x_0)| = |\pi\eta(\zeta - x_0)| \ll 1$, Eq. (3.53) can be expressed by Taylor's series expansion at $\eta(\zeta - x_0) = 0$

$$\Psi_1(\zeta) = \frac{1}{\pi} \ln \left[\frac{(\zeta - x_1)(\zeta - x_4)}{(\zeta - x_2)(\zeta - x_3)} \right] + \frac{\eta^2}{12\pi}(a_1^2 - a_2^2) + O(\eta^4). \tag{3.54}$$

A flat tape

Figure 3.6(b) plots the second case considered in this section, showing a flat tape on a flat film surface. The thickness of the tape is h, the width is w, and $w \gg h$. Under the assumption $w \gg h$, the flat tape can be viewed as a trapezoidal wire as shown in Fig. (3.6)(a) with $(x_4 - x_3)/(x_4 - x_1) \ll 1$. This suggests that the solution of the flat tape can be obtained by applying the limit $(x_4 - x_3)/(x_4 - x_1) \to 0$ to the solution of the trapezoidal wire written in Eq. (3.53),

$$\mathcal{S}\Psi_1(\zeta) = \frac{h}{\mathcal{S}H_f} \Re \left[\frac{1}{e^{\eta(\zeta - x_1)} - 1} - \frac{1}{e^{\eta(\zeta - x_2)} - 1} \right], \tag{3.55}$$

where x_1 and x_2, respectively, are the locations of the left and right edges of the tape. Substituting Eq. (3.55) into (3.43) shows that the effect of the thin flat tape on the electric field is proportional to the thickness h of the tape, and is insensitive to the slopes of the edges.

Trapezoidal pattern

Figure 3.6(c) depicts the trapezoidal pattern considered in the third case, where the characteristic slope is $\mathcal{S}_e$, the relative slope of the pattern is $\{-1, 0, 1\}$, and the x components of the vertices are $\{t_1, t_2, t_3, t_4\} = \{t_0 - d_1, t_0 - d_2, t_0 + d_2, t_0 + d_1\}$ where t_0 is the location of the center of the pattern, $2d_1$ is the width of the top surface on the electrode, and $2d_2$ is that of the surface facing the substrate. Substituting these quantities into Eq. (3.41)

yields $\Psi_2(\zeta)$ of the trapezoidal pattern,

$$\begin{aligned}\Psi_2(\zeta) &= \frac{\Re}{\pi}\left\{\ln\left[e^{\eta(\zeta-t_1)}+1\right]-\ln\left[e^{\eta(\zeta-t_2)}+1\right]\right.\\ &\quad \left.-\ln\left[e^{\eta(\zeta-t_3)}+1\right]+\ln\left[e^{\eta(\zeta-t_4)}+1\right]\right\}. \qquad (3.56)\end{aligned}$$

Similar to $\Psi_1(\zeta)$ of a trapezoidal wire, $\Psi_2(\zeta)$ of the pattern at large H_v/a_1 can be simplified by Taylor's series expansion at $\zeta = t_0$,

$$\Psi_2 = \mathcal{K}_0 + \mathcal{K}_2\hat{\zeta}^2 + O(\hat{\zeta}^4), \qquad (3.57)$$

where $\hat{\zeta} = \eta(\zeta - t_0)$ and the two coefficients $\mathcal{K}_0$ and $\mathcal{K}_2$ are given by

$$\mathcal{K}_0 = \frac{2}{\pi}\ln\left[\frac{\cosh(\eta d_1/2)}{\cosh(\eta d_2/2)}\right] \qquad (3.58)$$

$$(3.59)$$

$$\mathcal{K}_2 = \frac{1}{4\pi}\frac{\sinh[\eta(d_1-d_2)/2]\sinh[\eta(d_1+d_2)/2]}{\cosh^2(\eta d_1/2)\cosh^2(\eta d_2/2)}. \qquad (3.60)$$

Electrostatic energy change

In this section we derive the electrostatic energy change ΔW_e (per unit length in the y direction) due to the formation of a wire on the film surface. The derivation process follows closely the procedure for evaluating the strain energy change of strained faceted wires (Chiu and Poh 2005). The procedure starts with writing down the variation of the total electrostatic energy of the system δW_e with that of the film morphology δf (Chiu et al. 2006; Du and Srolovitz 2004),

$$\delta W_e = -\int w_e \delta f dx. \qquad (3.61)$$

The wire morphology can be obtained by changing the characteristic slope $\mathcal{S}$ but fixing other parameters in the system, including the pattern geometry, the relative slope m, and the projection $\mathcal{B}$ of the wire facets onto its base. When $\mathcal{S} = 0$, the morphology is a flat

film; as $\mathcal{S}$ increases, a wire is added gradually onto the film. The morphological variation δf during the process can be expressed as

$$\delta f(x) = \hat{f}(x)\delta\mathcal{S}, \tag{3.62}$$

where $\hat{f}(x) = f(x)/\mathcal{S}$ is the normalized wire shape function depending on the size and the relative facet slope m of the wire. The volume of the film increases and accordingly that of the dielectric media decreases during the variation process described in Eq. (3.62). This implies that the total electrostatic energy change during the process would include the effect due to the volume change and that due to the wire shape. This becomes clear later in Eq. (3.63).

Substituting Eqs. (3.48) and (3.62) into (3.61) leads to

$$\begin{aligned}\frac{dW_e}{d\mathcal{S}} &= -w_{0e}\left\{\int \hat{f}(x)dx + 2\mathcal{S}\int \Psi_1(x)\hat{f}(x)dx \right.\\ &\left. + 2\mathcal{S}_e\int \Psi_2(x)\hat{f}(x)dx\right\}.\end{aligned} \tag{3.63}$$

Integrating Eq. (3.63) with respect to $\mathcal{S}$ from 0 to $\mathcal{S}$ and noticing that the three integrals in the equation are independent of $\mathcal{S}$ yields the total electrostatic energy change ΔW^* during the process,

$$\begin{aligned}\Delta W^* &= -w_{e0}\left\{\int \mathcal{S}\hat{f}(x)dx + \mathcal{S}^2\int \Psi_1(x)\hat{f}(x)dx \right.\\ &\left. + 2\mathcal{S}\mathcal{S}_e\int \Psi_2(x)\hat{f}(x)dx\right\}.\end{aligned} \tag{3.64}$$

By using $f = \mathcal{S}\hat{f}$ and noticing that the first integral in Eq. (3.64) gives the island volume V, the electrostatic energy change dW^* in Eq. (3.64) can be rewritten as

$$\Delta W^* = -w_{e0}V + \Delta W, \tag{3.65}$$

where

$$\Delta W \quad = \quad -w_{e0}\left\{\mathcal{S}\int \Psi_1(x)f(x)dx + 2\mathcal{S}_e\int \Psi_2(x)f(x)dx\right\} + O(\mathcal{S}^2_{max}).$$

It can be demonstrated that the first term $-w_{e0}V$ in Eq. (3.65) is the electrostatic energy change when the total film volume increases by V without the formation of any wire on the film. This interpretation of $-w_{e0}V$ suggests the second term ΔW in Eq. (3.66) is the electrostatic energy change due to the formation of wire when the volume of the film and that of the dielectric media are fixed. The second term ΔW can be regarded as the electrostatic energy of the wire.

The wire electrostatic energy ΔW in Eq. (3.66) can be rewritten as

$$\Delta W = -w_{e0}\mathcal{S}VU_1 - 2w_{e0}\mathcal{S}_eVU_2 + O(\mathcal{S}^2_{max}), \tag{3.66}$$

where U_1 and U_2 are determined by

$$U_k = \frac{1}{V}\int \Psi_k(x)f(x)dx. \tag{3.67}$$

The result indicates ΔW consists of two parts. The first part, $-w_{e0}\mathcal{S}VU_1$, is the electrostatic energy of a wire in the absence of the pattern on the electric plate. This part is proportional to the electrostatic energy density w_{e0}, the slope $\mathcal{S}$ of the wire, the volume V of the wire, and the quantity U_1 representing the effect of the wire shape. In comparison, the second part of Eq. (3.66) refers to the influence of the pattern; this part is controlled by the density w_{e0}, the wire volume V, the slope of the pattern, and the quantity U_2 indicating the pattern shape effect.

General solution of trapezoidal wires and patterns

To derive the general solution of trapezoidal wires and patterns, Eqs. (3.66) and (3.67) are employed to investigate the electrostatic energy ΔW_e of the system shown in Fig. 3.7 where a trapezoidal wire is exposed to an electric plate containing a trapezoidal pattern

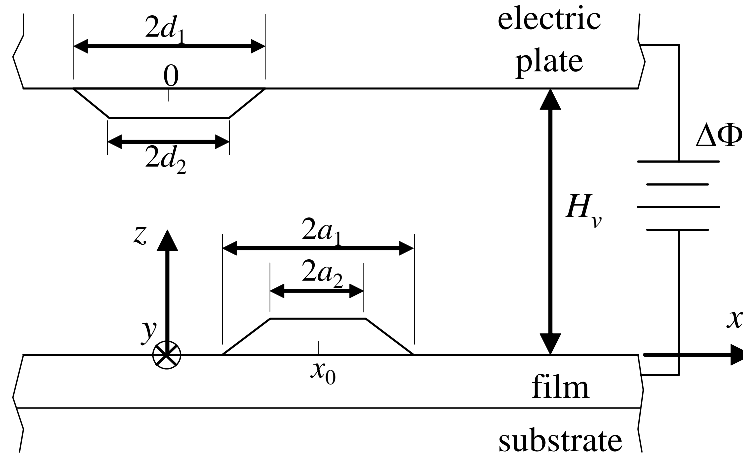

Figure 3.7: Schematic diagram of a trapezoidal wire under the influence of a trapezoidal pattern with a misalignment of x_0 between the centers of the two structures.

that is misaligned with the wire. Of particular interest here is to obtain an analytical expression for the dependence of ΔW on the electrode height H_v between the film surface and the electric plate, the width ratio $\xi = a_2/a_1$ of the wire, the shape and size of the pattern, and the misalignment x_0 between the wire and the pattern when H_v is large.

The key to the investigation is to determine the two quantities U_1 and U_2 defined in Eq. (3.67) for the case where $a_1/H_v \ll 1$. The first one, U_1, can be calculated by substituting the asymptotic result of $\Psi_1(x)$ given in Eq. (3.54) and the surface profile $f(x)$ of the trapezoidal wire,

$$f(x) = \begin{cases} \mathcal{S}(x - x_1) & x_1 \le x \le x_2 \\ \mathcal{S}(a_1 - a_2) & x_2 \le x \le x_3 \\ -\mathcal{S}(x - x_4) & x_3 \le x \le x_4, \end{cases} \quad , \tag{3.68}$$

into Eq. (3.67) to yield

$$U_1 V = \frac{2\mathcal{S}}{\pi}\left[(a_1^2 + a_2^2)\ln 4 + 2a_1^2 \ln a_1 + 2a_2^2 \ln a_2 - (a_1 - a_2)^2 \ln(a_1 - a_2) \right.$$
$$\left. -(a_1 + a_2)^2 \ln(a_1 + a_2) + \frac{(a_1^2 - a_2^2)^2}{24}\eta^2\right]. \tag{3.69}$$

By evoking the definition $a_2/a_1 = \xi$ and evaluating the wire volume $V = \mathcal{S}(a_1^2 - a_2^2)$, U_1 in Eq. (3.69) can be simplified to

$$U_1 = \frac{2}{\pi}\left[\frac{1+\xi^2}{1-\xi^2}\ln 4 + \frac{2\xi^2}{1-\xi^2}\ln\xi \right.$$
$$\left. -\frac{1-\xi}{1+\xi}\ln(1-\xi) - \frac{1+\xi}{1-\xi}\ln(1+\xi)\right] + \frac{\pi(1-\xi^2)}{12}\left(\frac{a_1}{H_v}\right)^2. \tag{3.70}$$

The first four terms in Eq. (3.70) represent the effect of the wire width ratio ξ on U_1 when $a_1/H_v = 0$, while the last term describes the dependence of U_1 on a_1/H_v.

The quantity U_1 expressed in Eq. (3.70) is further explored in Fig. 3.8 by plotting the variation of U_1 with the wire width ratio ξ for the cases, where $a_1/H_v = 0$ and 0.5. The results, denoted by the solid lines in the figure, indicate U_1 is positive and declines as xi increases from 0 to 1. The findings show the wire formation causes the electrostatic energy of the system to decrease, and a triangular wire ($\xi = 0$) is more effective in reducing the electrostatic energy than a trapezoidal one for the same amount of wire volume V and slope $\mathcal{S}$. Comparing the results of the two cases reveals that larger a_1/H_v leads to higher U_1; in other words, smaller electrode height H_v can induce more electrostatic energy reduction even though the electric field $\Delta\Phi/H_v$ is fixed.

In addition to the analytical result given in Eq. (3.70), Fig. 3.8(a) also depicts numerical results of U_1, which are obtained by carrying out the integration given in Eq. (3.67) and are denoted by the solid circles in the figure. The differences between the numerical and the analytical results are found to be small. The finding suggests that, though derived from the condition $a_1/H_v \ll 1$, Eq. (3.70) is a good approximation of U_1 even when a_1/H_v is as high as 0.5.

After understanding U_1, our investigation turns to the quantity U_2 at large H_v. The

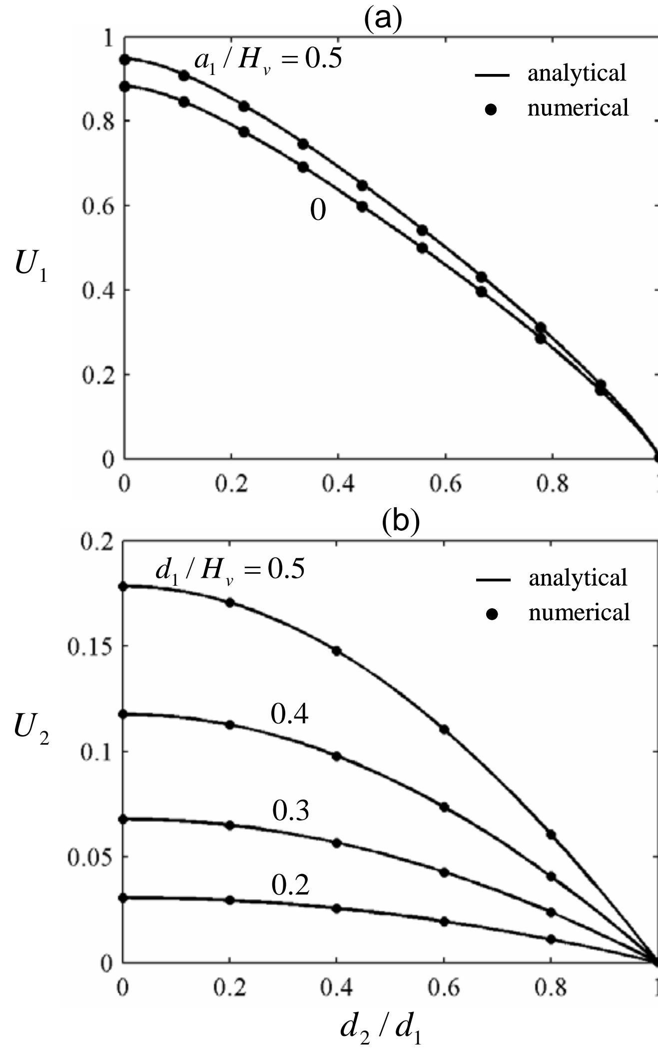

Figure 3.8: (a) The variation of U_1 with the wire width ratio ξ for the cases, where $a_1/H_v = 0$ and 0.5. (b) The variation of U_2 with d_2/d_1 for the cases, where $a_1/H_v = 0.1$, $x_0 =$, and $d_1/H_v = 0.2$, 0.3, 0.4, and 0.5.

quantity is determined by substituting $\Psi_2(x)$ given in Eq. (3.70) and the function $f(x)$ expressed in (3.68) into Eq. (3.67),

$$U_2 = \mathcal{K}_0 - \pi^2 \mathcal{K}_2 \left[\frac{1+\xi^2}{6} \left(\frac{a_1}{H_v} \right)^2 + \left(\frac{x_0}{H_v} \right)^2 \right], \tag{3.71}$$

where $\mathcal{K}_0$ and $\mathcal{K}_2$ are given in Eqs. (3.58) and (3.60), respectively. The first term in Eq. (3.71) refers to the effect of the pattern geometry on U_2 when a_1/H_v is negligible and $x_0 = 0$; the effect, as indicated in Eq. (3.58), is controlled by the pattern width ratio d_1/d_2 and the normalized pattern size d_1/H_v. In comparison, the second and the

third terms describe the dependence of U_2 on the normalized wire size a_1/H_v and the normalized misalignment x_0/H_v, respectively. The third term is found to decrease with x_0/H_v, meaning a wire aligning with the pattern is more energetically favorable than misaligned ones. This demonstrates the potential capability of using the patterns to dictate the wire locations.

According to Eq. (3.71), Fig. 3.8(b) depicts the variation of U_2 with the pattern width ratio d_2/d_1 for the cases, where $d_1/H_v = 0.2$, 0.3, 0.4, and 0.5, $x_0 = 0$, $a_1/H_v = 0.1$, and $\xi = 0$. The results, denoted by the solid lines, indicate U_2 is positive and declines with increasing d_2/d_1 and/or decreasing d_1/H_v. The findings show that the electrostatic energy reduction due to the wire formation is enhanced by the pattern; the pattern effect is the highest when the pattern shape is triangular; and the effect increases with the pattern size.

Besides the properties of U_2, Fig. 3.8(b) also compares the analytical expression for U_2 given in Eq. (3.71) with the numerical results, which are calculated by Eq. (3.67) and denoted by the solid circles in the figure. The differences between the analytical and numerical results are negligible for the cases considered in the figure. Further investigation suggests the difference increases with a_1/H_v and reaches 6.5% when $a_1/H_v = 0.5$. The result shows that Eq. (3.71) is a good approximation of U_2 for moderate values of a_1/H_v.

3.3 Interaction Energy

As discussed earlier in Sec. 2.1, the interaction energy can be modeled by a special type of surface energy of which the density g depends on the distance z between the film surface and the film-substrate interface. Thus, the change of the interaction energy is determined by

$$\Delta E_I = \int g d\Gamma_{\mathcal{B}} + \int g d\Gamma_w - \int g d\Gamma_0, \tag{3.72}$$

where $d\Gamma_{\mathcal{B}}$ refers to the area integral over the wire facets, $d\Gamma_w$ represents that over the wetting layer surface, and $d\Gamma_0$ denotes that over the flat film surface before the wire

formation.

The area integral $d\Gamma_{\mathcal{B}}$ can be expressed as $d\Gamma_{\mathcal{B}} = (\mathcal{S}m)^{-1}dx$; substituting the expression into the first term in Eq. (3.72) yields,

$$\int g d\Gamma_{\mathcal{B}} = \sum_{j=1}^{N} \frac{1}{\sin\phi_j} \left[\mathcal{G}(z_{j+1}) - \mathcal{G}(z_j)\right], \tag{3.73}$$

where z_j is the z component of the jth vertices of the wire and $\mathcal{G}(z)$ is defined by

$$\mathcal{G}(z) = \int g(z)dz. \tag{3.74}$$

The function $\mathcal{G}(z)$ is simplified to $\mathcal{G}(z) = g_0 l \ln(z + H_f + l)$ if the quantum confinement is the mechanism of the film-substrate interaction.

Turn to the second and the third terms in Eq. (3.72). The third term refers to the interaction energy of the system prior to the wire formation, and is given by $g(H_f)A$, where A is the area of the flat films surface. The second term, on the other hand, corresponds to the interaction energy of the flat wetting layer after the wire formation, and can be expressed as $g(H_f - \Delta H_f)(A - b)$, where $b = b_{N+1} - b_1$ is the width of the wire base, $H_f - \Delta H_f$ is the thickness of the wetting layer, and $\Delta H_f = V/A$. By evoking the conditions $A \gg b$ and $H_f \gg \Delta H_f$, the difference between the second and the third terms can be calculated to be

$$g(H_f - \Delta H_f)(A - b) - g(H_f)A = -g'(H_f)V - g(H_f)b. \tag{3.75}$$

Adding the above result and that expressed in Eq. (3.73) and adopting the simplification $\sin\phi_j \approx \mathcal{S}m_j$ for small values of ϕ_j determine the change of the interaction energy to be

$$\Delta E_I \;=\; \frac{1}{\mathcal{S}} \sum_{j=1}^{N} \frac{\mathcal{G}(z_{j+1}) - \mathcal{G}(z_j)}{m_j} - g(H_f)(b_{N+1} - b_1) - g'(H_f)V. \tag{3.76}$$

Equation (3.76) is for two-dimensional cases. The result of the three-dimensional cases can be obtained by a similar approach except that the integrations in Eq. (3.72) becomes

area integrals instead of line integrals. Carrying out the area integrals for a pyramid with a square base and assuming the interaction mechanism is quantum confinement yields the interaction energy change ΔE_I due to the formation of the pyramid,

$$I(\hat{A}) = -1 + \frac{\hat{A}}{3} + \frac{2(1+\hat{A})\ln(1+\hat{A}) - 2\hat{A}}{\hat{A}^2 \cos\phi}. \tag{3.77}$$

3.4 Surface Energy

The surface energy change ΔE_s due to the formation of the nanostructure can be expressed as

$$\Delta E_s = \sum_{j=1}^{N} \gamma_0 G_j (b_{j+1} - b_j), \tag{3.78}$$

where $G_j = -1 + \gamma_j/(\gamma_0 \cos\phi_j)$, γ_j is the surface energy density of the jth facet, and γ_0 is that of the flat wetting layer. Summing the changes of the strain, electrostatic, interaction, and surface energy yields the total energy change ΔE_{tot},

$$\Delta E_{tot} = \Delta W_\sigma + \Delta W_e + \Delta E_I + \Delta E_s. \tag{3.79}$$

Chapter 4

Critical Film Thickness for Stranski-Krastanow Transition

4.1 Introduction

The formation of nanoislands is generally observed in the SK mode in heteroepitaxial film-substrate systems. The 3D structures can form after the film thickness exceeds a critical value, and the formation can take place via two kinetic mechanisms: spontaneous formation by nucleation and gradual morphological transition by surface diffusion. In the nucleation process, the structure has to be larger than a critical size in order to be stable against shrinkage, and there is an energy barrier for the structure to exceed the critical size (Tersoff and Tromp 1993). In comparison, the surface undulation process is characterized by smooth morphological changes without experiencing an energy barrier (Tersoff et al. 2002).

The two mechanisms of island formation, namely, the spontaneous formation and surface undulation, not only affect the pathways of the formation but also influence the critical film thickness for the SK transition. The critical film thickness of the two mechanisms are derived in this chapter, and it is found that the critical thickness under surface undulation is larger than that under spontaneous formation. The difference in the critical thickness implies that there is a special thickness range in which an almost flat film

can develop into islands via spontaneous formation but with surface undulation being suppressed. The thickness range can be exploited to control the nanostructure formation.

This chapter is divided into two parts. The first part analyzes the critical film thickness of the SK systems for the case of surface undulation and spontaneous formation. The second part of this chapter then focuses on the scheme of fabricating self-assembled nanostructures in the special film thickness range. This scheme is named the activated Stranski-Krastanow transition (ASKT) method.

4.2 The Critical Film Thickness of the SK Transition

Our study is based on the continuum model for the SK film-substrate systems (Chiu 1999a), which is discussed in Chaps. 2 and 3. Therefore the system described here is characterized by the surface energy γ, the film thickness H_f and the two length scales of the system, namely $\hat{g}_0 l = g_0 l/\gamma_0$ and $L = \gamma_0/w_{\sigma 0}$.

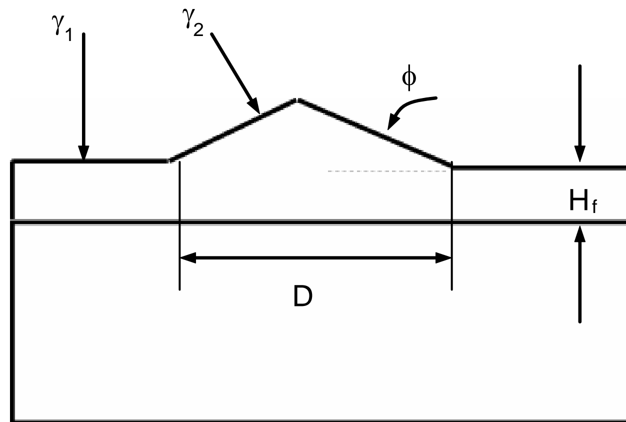

Figure 4.1: A schematic diagram of a pyramid island on a film-substrate system.

We first calculate the total energy change ΔE_{tot} as the SK system undergoes a mass-conserved shape transition from a flat film to one with a pyramid island as shown in Fig. 4.1. The film thickness is H_f, the island base width is D, the island height is A, and the facet angle is ϕ. The surface energy densities of the wetting layer and the facet surface

are γ_1 and γ_2, respectively. The total energy change ΔE_{tot} is the sum of the change of the surface energy ΔE_s, the interaction energy ΔE_I, and the strain energy ΔW_σ. The quantities ΔE_s and ΔE_I can be can be calculated by using Eqs. (3.76) and (3.78), and ΔW_σ is expressed in Eq. (3.34). Summing the results yields

$$\Delta E_{tot} = -U_0 w_{\sigma 0} \mathcal{S} D^3/6 + \gamma_1 D^2 G + g(H_f) D^2 I(\hat{A}), \tag{4.1}$$

where $\hat{A} = A/(H_f + L)$, $G = 1 + \gamma_2/\gamma_1 \cos\phi$, $U_0 = 1.98$, and $I(\hat{A})$ is expressed in Eq. (3.77).

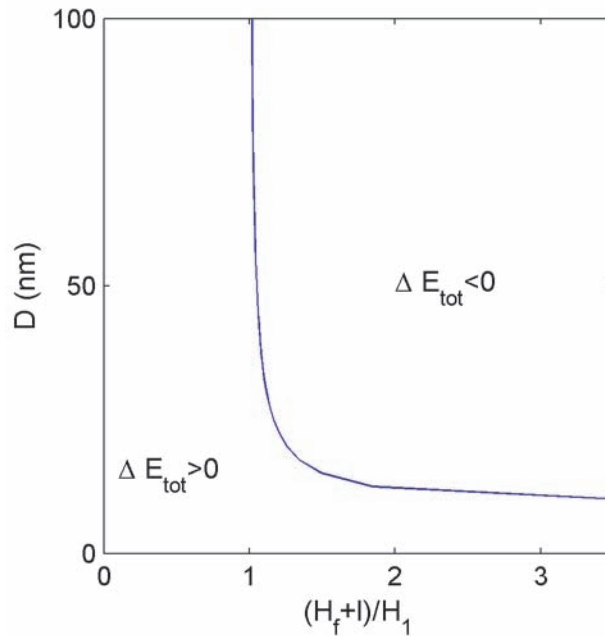

Figure 4.2: The region of (D, H_f) in which the island formation is energetically favored for the case where $L = 250$ Å, $\phi = 11.4°$, $\gamma_2/\gamma_0 = 0.99$, $\gamma_1/\gamma_0 = 0.99$, and $l = 1$ Å. The corresponding stability number Σ is negative.

The total energy change $\Delta E_{tot}(D, H_f)$ depends on the island size D and the film thickness H_f. The domain (D, H_f) with $\Delta E_{tot} < 0$ specifies the region in which the island formation is energetically favorable. The characteristic of the region is found to be controlled by the sign of the stability number Σ.

$$\Sigma = \sqrt{\frac{\hat{g}_0 l U_0 \mathcal{S}}{L}} - \frac{\gamma_1 G}{\gamma_0}. \tag{4.2}$$

An example is shown in Fig. 4.2 for the case where $\Sigma < 0$. The results indicates that the island formation is energetically favorable when the island size is larger than a critical value D_{cr}. At large film thickness, D_{cr} is a constant, which can be derived as follows.

When $H_f \to \infty$, $\hat{A}$ is infinitesimally small, and $I(\hat{A})$ in Eq. (3.77) is reduced to

$$I(\hat{A}) = -1 + \frac{\hat{A}}{3} + \frac{2}{\cos\phi}. \tag{4.3}$$

Substituting Eq. (4.3) into (4.1) yields,

$$\Delta E_{tot} = -U_0 w_{\sigma 0} \mathcal{S}^2 D^3/6 + \gamma_1 D^2 G, \tag{4.4}$$

which is dictated by strain energy and surface energy. Equation (4.4) suggests the total energy ΔE_{tot} is negative when the island size is sufficiently large. Solving the equation $\Delta E_{tot} = 0$ determines the critical island size D_{cr} at large values of H_f,

$$\lim_{H_f \to \infty} D_{cr} = \frac{6\gamma_1 GL}{\gamma_0 U_0 \mathcal{S}^2}, \tag{4.5}$$

which is independent of the film thickness H_f. The result is consistent with that derived earlier by Tersoff and Tromp (1993).

After discussing D_{cr} at large H_f, our focus turns to the dependence of D_{cr} on H_f. As illustrated in Fig. 4.2, the critical island size D_{cr} increases as the film thickness decreases and reaches infinity at a critical value of thickness. The finding suggests the critical film thickness can be determined by analyzing the total energy change of large islands. In the case of large islands, $\hat{A} \to \infty$, $I(\hat{A})$ is reduced to $\hat{A}/3$, and the total energy change can be expressed as

$$\Delta E_{tot} = \left[-U_0 w_{\sigma 0} \mathcal{S}^2 + \frac{\mathcal{S}\hat{g}_0 l}{H_f + l}\right] \frac{D^3}{6} - \gamma_1 \left[\frac{\hat{g}_0 l}{\gamma_1 (H_f + l)} - G\right] D^2. \tag{4.6}$$

Equation (4.6) indicates the total energy change at large D is dictated by the coefficient of D^3. A positive coefficient means the total energy change is still positive even when the

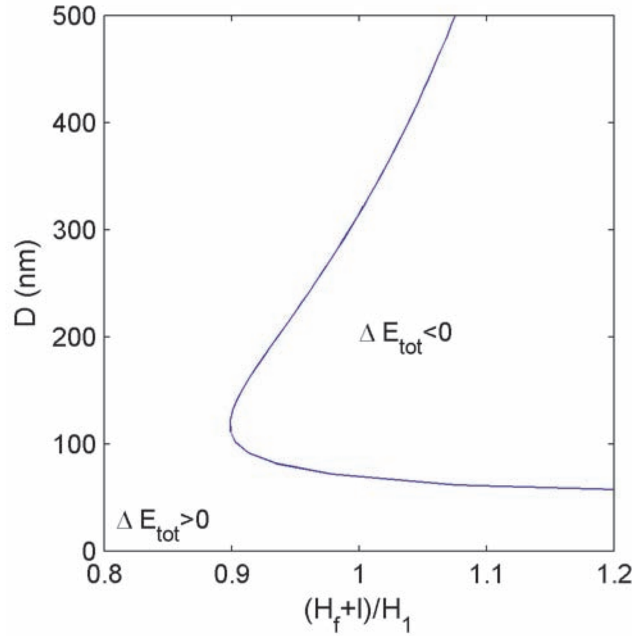

Figure 4.3: The region of (D, H_f) in which the island formation is energetically favored for the case where $L = 250$ Å, $\phi = 11.4°$, $\hat{g}_0 = 0.3$ and $\Sigma > 0$

island size is big; therefore, the island formation is suppressed in this case. A negative coefficient, on the other hand, indicates the total energy becomes negative when the island size is sufficiently large and the island formation is energetically favorable. The condition that the coefficient is zero determines the critical film thickness for the SK transition,

$$H_f + l = H_1 = \sqrt{\frac{\hat{g}_0 l L}{U_0 \mathcal{S}}} = \sqrt{\frac{g_0 l}{w_{\sigma 0} U_0 \mathcal{S}}}. \tag{4.7}$$

In the range $H_f + l < H_1$, the spontaneous formation of any pyramid island with facet angle ϕ is prohibited.

Figure 4.3 plots the region (D, H_f) of $\Delta E_{tot} < 0$ for the case where $\Sigma > 0$. The region is characterized by three thickness ranges. In the range $(H_f + L)/H_1 > 1$, island formation is favored when D exceeds a critical value D_{cr}. Similar to the case of $\Sigma < 0$, D_{cr} is a constant given by Eq. (4.5) at large film thickness and D_{cr} increases as the film thickness decreases. The critical size D_{cr} in the current case, however, reaches a finite value at $H_f + l = H_1$ instead of an infinitely large number as in the previous case. When the film thickness is less than $H_1 - l$, the energetically favorable island size is bounded by

two values; the upper and the lower bounds approach each other and coincide at some film thickness. Below this thickness, island formation is suppressed. The findings, together with the result sin Fig. 4.3, show that, irrespective of the sign of Σ, $(H_f + l) > H_1$ is a sufficient condition for the island formation to be energetically favorable.

The critical value H_1 results from the competition between the strain energy relaxation ΔW_σ and the interaction energy change ΔE_I for the case of large island. As shown in Eq. (4.6), both types of energy dominate the total energy change ΔE_{tot} in this case. The strain energy relaxation ΔW_σ favors island formation, and is proportional to D^3. The strength of the relaxation is a constant given by $U_0 w_{\sigma 0} \tan^2(\phi)/6$. The interaction relaxation, on the other hand, discourages the formation of islands since the formation causes a thinner wetting layer and thus higher interaction energy. The corresponding interaction energy change is also proportional to D^3, while the strength decreases with the film thickness. As a consequence, the strain energy dictates at large H_f, but the interaction energy at small H_f is strong enough to suppress the formation of large islands. The balance of the two types of energy occurs at $H_f + l = H_1$.

According to Eq. (4.6), the total energy change ΔE_{tot} at the critical thickness H_1 is determined by the coefficient of D^2 since the coefficient of D^3 is zero at the critical thickness. The coefficient of D^2 can be rewritten as

$$\frac{\hat{g}_0 l}{(H_f + l)} - \gamma_1 G = \sqrt{\frac{\hat{g}_0 l U_0 \mathcal{S}}{L}} - \gamma_1 G = -\gamma_1 \Sigma, \tag{4.8}$$

which depends on the stability number Σ. The dependence suggests that the characteristics of the favorable island formation region is significantly affected by the parameter Σ. When Σ is negative as in the coarsening case, the D^2 term is positive. Therefore, both the D^3 and D^2 terms are positive when $H_f + l < H_1$. This explains why island formation is suppressed in the range $H_f + l < H_1$ and the critical island size is infinity at $H_f + l = H_1$ as shown in Fig. 4.3. Turn to the case where Σ is positive. In this case, the D^3 term is still positive when the film thickness is slightly smaller than the critical value, while the D^2 term is negative. The opposite signs of the D^3 and D^2 terms mean that the total

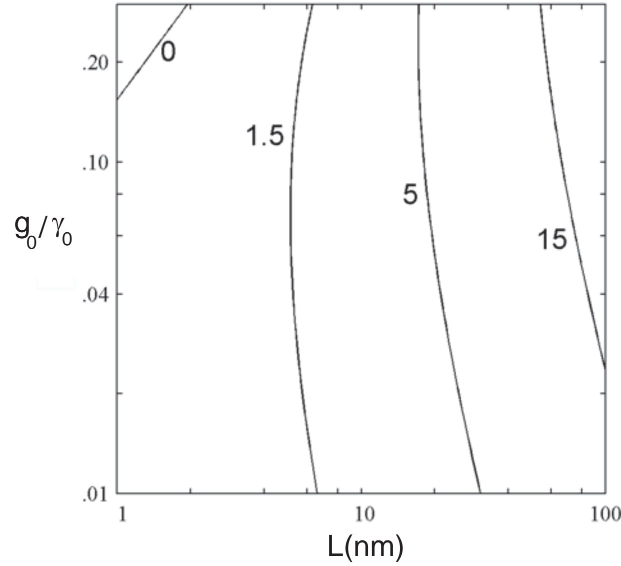

Figure 4.4: The contours of $H_2 - H_1$, in Å, as a function of L and $\hat{g}_0$. $\phi = 11.3°$, $\gamma_2/\gamma_0 = 0.99$, and $\gamma_1/\gamma_0 = 1$

energy can be negative if the island size is small. This explains the result in Fig. 4.8 that the island can form on a stable film with $H_f + l$ less than H_1.

In contrast to the spontaneous formation, the surface undulation means the film first develops a slightly wavy surface before the surface transforms into faceted island (Rastelli et al. 2003; Tersoff et al. 2002). The critical film thickness for island formation via surface undulation can be determined by solving a nonlinear equation derived in (Chiu 1999a). Nevertheless, when g_0 is much less than γ_0, the result can be simplified to (Chiu 1999a;b; Suo and Zhang 1998)

$$H_f + l = H_2 = \sqrt[3]{\frac{\alpha \hat{g}_0 l L^2}{2}} = \sqrt[3]{\frac{\alpha . g_0 \gamma_0 l L^2}{2 w_{\sigma 0}^2}}. \tag{4.9}$$

Figure 4.4 plots the difference $H_2 - H_1$ as a function of L and $\hat{g}_0$ when $\phi = 11.3°$ and $\alpha = 1$. The result demonstrates that except at small L and large $\hat{g}_0$, the critical thickness H_2 for surface undulation is larger than H_1 for spontaneous formation. The difference is more than the height of one Si mono layer when $L > 10$ nm and $\hat{g}_0 \in [0.01, 0.02]$.

The difference between island nucleation and surface undulation is analogous to that

between nucleation and spinodal decomposition in phase transformation. The surface undulation and the spinodal decomposition both occur under the condition that the energy of the system is in the vicinity of a maximum so that the system can evolve toward a minimum without involving nucleation. Nucleation, in contrast, is needed in order for the system to reach another energy minimum if the energy of the system has been in the vicinity of a minimum. In island formation, this corresponds to the case that the flat surface is stable against infinitesimal perturbation but the facet island formation is energetically favorable.

Although the case where $H_2 < H_1$ cannot be ruled out mathematically, this would not occur in the SK systems studied in experiments because the corresponding interaction energy density would result in unreasonably large critical film thickness for the SK transition. Take $L = 62.5$ Å in the Fig. 4.4 for example, which is about the value of Ge/Si system. The quantity H_2 in this case has to be larger than 12 Å in order to satisfy the condition $H_2 < H_1$, but the value is much larger than the experimental findings, which is between 4 and 5 Å.

In summary, due to the fact that the first critical thickness H_1 of spontaneous formation is found to be smaller than the second critical film thickness H_2 of surface undulation in most of the cases, the morphological evolution can be classified into three regimes according to the film thickness. At small thickness, $H_f < H_1$, the morphological evolution leads to a flat film for any initial surface profile. At large film thickness $H_f + l > H_2$, in contrast, the morphological evolution always causes surface undulation and faceted island formation, irrespective of the initial profile. For films with thickness in the range $H_1 < H_f + l < H_2$, the outcome of the morphological evolution of a film depends on the initial profile. If the evolution starts with a slightly rough surface, the morphological evolution results in a flat film. The morphological evolution, however, can produce faceted island if there are sufficiently large pre-existing patterns or nanostructures on the film surface. The finding motivates us to propose an approach to control the self-assembled nanostructures by pre-patterning in the thickness range of $H_1 < H_f < H_2$ (Chiu et al. 2004).

4.3 The Activated Stranski-Krastanow Transition Method

4.3.1 Introduction

The SK systems satisfying the condition $H_2 > H_1$ can be applied to control the growth of nanostructures. The proposed scheme, called the activated Stranski-Krastanow transition (ASKT) method, is to make patterns on the film in the thickness range $H_1 < H_f < H_2$ and then anneal the system. If the patterns are larger than the critical size as shown in Fig. 4.2, the formation of islands is energetically favorable, and the patterns can self-assemble into nanostructures during the annealing process. The un-patterned surface, on the other hand, will remain smooth. The contrast between the patterned and un-patterned surfaces means the nanostructures can be fabricated at the selected locations.

The suppression of surface undulation and island nucleation on the un-patterned flat area can be understood as follows. The surface undulation is prohibited since the surface is stable against waviness of small amplitude in the special thickness range. The island nucleation is possible energetically but impeded kinetically because of a low adatom density during the annealing process. The low density significantly reduces the probability that a sufficient number of adatoms can accumulate in a small regime to attempt nucleus formation.

The patterns in the ASKT method can develop into nano-structures during the annealing process by the spontaneous shape transition and the surface undulation. The first mechanism is similar to the island nucleation, and it is insignificant during the annealing process. The surface undulation is prohibited on the un-patterned surface; however, the mechanism can be activated by the patterns to facilitate nano-structure formation.

In summary, the ASKT method is to anneal the SK systems in a special thickness range. In this method, islands cannot form on the flat film surface since the surface undulation is suppressed energetically and the spontaneous island formation is kinetically

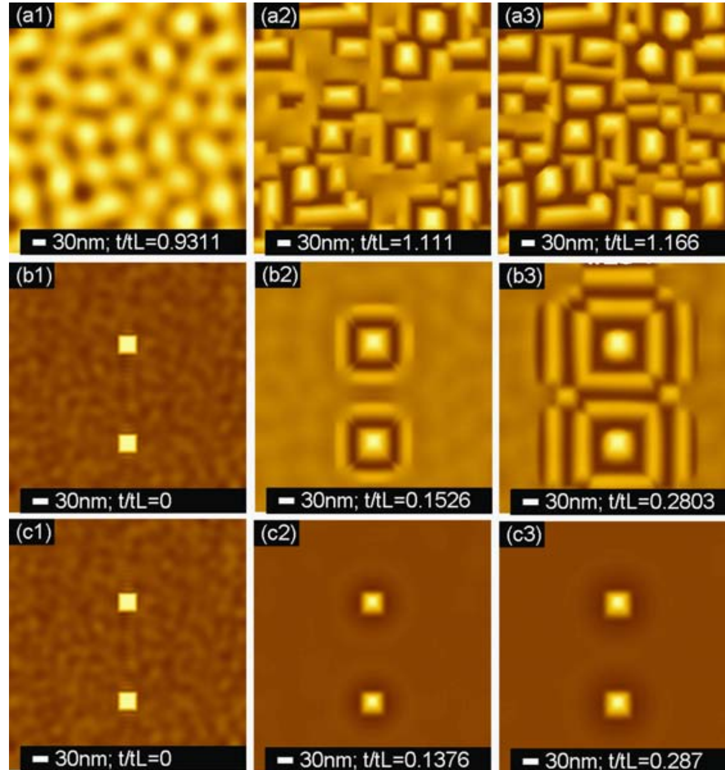

Figure 4.5: The simulation results for the morphological evolution of the SK systems, where L = 250 Å, $\hat{g}_0$ = 0.0625, l = 1 Å. Three cases of different film thickness H_f and the initial surface profile are shown in (a1-a3), (b1-b3), and (c1-c3). In particular, H_f =2.5, 2.5, and 1.05 nm in (a1-a3), (b1-b3), and (c1-c3), respectively. The initial surface for the case in (a1-a3) is a slightly wavy surface; those in (b1)-b(3) and (c1)-(c3) are identical, containing two square patterns. The color represents the height of the surface, varying from brown for trenches/valleys to light yellow for peaks. The corresponding height difference is 0.04, 7.6, 8.1, 1.4, 7.5, 8.3, 1.4, 4.3, and 5.2 in (a1-c3), respectively.

impeded. The island formation, however, can be activated by introducing patterns on the film to self-assemble into nano-structures by surface undulation.

4.3.2 Numerical Simulation

The self-assembly process controlled by the surface undulation mechanism is further studied by numerical simulation to explore the potential capability of the ASKT method. The implementation of the numerical simulation is discussed in Chap. 3.

We considered the model system where $L = 250$ Å, $\hat{g}_0 = 0.0625$, and $l = 1$ Å, corresponding to $Si_{50}Ge_{50}$/Si film-substrate system. We compared the morphological evolution of the SK system in the two thickness ranges, $H_f + l > H_2$ and $H_1 < H_f + l < H_2$. The

morphological evolution in the first range, plotted in Figs. 4.5(a1)-4.5(b3), follows the cooperative formation process: island are encircled by trenches, and subsequently the trenches facilitate the growth of island at the adjacent sites. The cooperative formation can be triggered on a slightly wavy surface, see Figs. 4.5(a1)-(a3), and on a patterned surface, see4.5(b1)-(b3). The results are consistent with the experimental findings of similar Si_xGe_{1-x}/Si system (Jesson et al. 1996). The results also suggest that it is challenging to control the island locations and island shapes when the surface undulation can occur on the whole surface.

The morphological evolution of the same system is completely different when the film thickness is in the second range $H_f + l \in [H_1, H_2]$. The surface undulation of small amplitude is energetically unfavorable in this case, and our simulation confirmed that a slightly wavy surface would evolve toward a flat profile. The morphological evolution of a patterned surface is plotted in Figs. 4.5(c1)-(c3). The results demonstrate that the patterns can develop into islands without inducing other nanostructures on the surface.

Besides single islands, different patterns may self-assemble into different shapes of nanostructures. This is shown in our simulation by varying the size, the height, and the aspect ratio of rectangle patterns on the same SK system considered in Fig. 4.5 with $H_f \approx 1$ nm. The structures found in our simulations includes island arrays, rings, and wires as shown in Fig. 4.6. The island arrays can be 2×2 and 3×3. The ring shape can be a square or a rectangle, and it can contain a single rim or multiple rims. Since the shapes are controlled by the pattern geometry, all the shapes can be produced on the same substrate.

The nanostructures shown in Fig. 4.6 are appealing for their unique morphologies and their potential in device application. For example, the 2×2 island array and the square ring may be adopted as the basic unit for the quantum cellular automata (Orlov et al. 1997). The wire and the long rectangular ring may be used for the nano-electronic devices (Cui and Lieber 2001). In addition to the two examples, other applications can also be developed by using different patterns to produces more complicated structures.

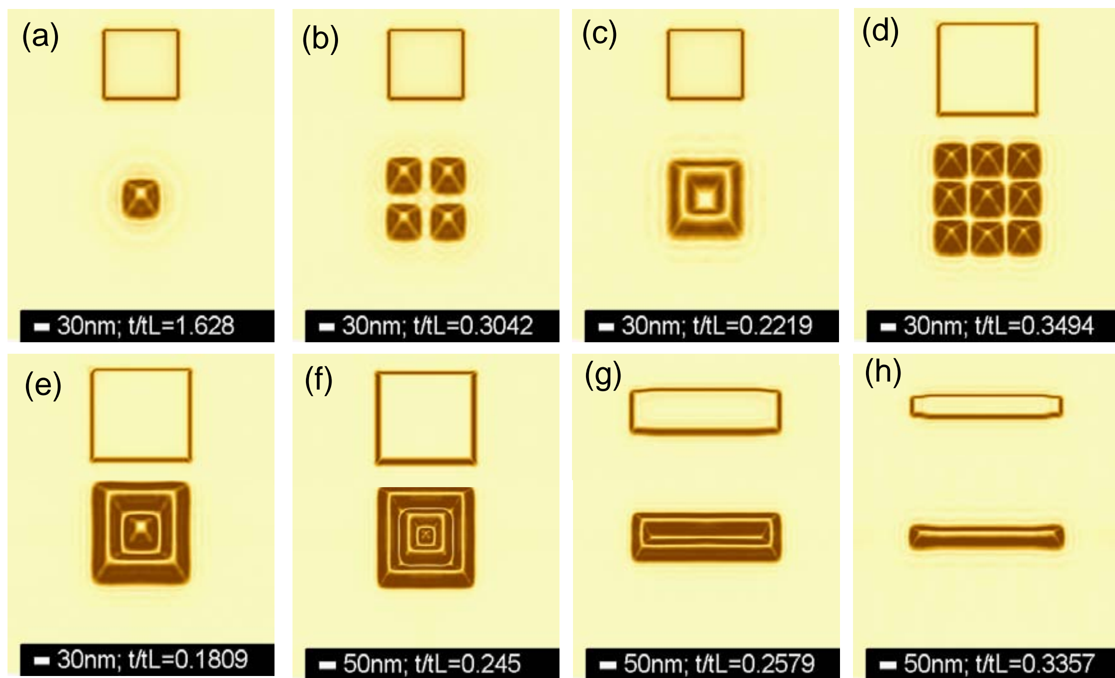

Figure 4.6: The simulation results for the effect of the pattern geometry on the shapes of the nanostructures fabricated by the ASKT method. The size of the patterns are (a-c) 150, (d-f) 200, (g) 150×450, and (h) 50×450 nm. The height of the patterns is 0.75, 1.55, 3.1, 3.5, 2.9, and 2.5 nm in (a-h), respectively. The patterns lead to (a) single pyramid island; (b) 2×2 island array; (c) 3×3 island array; (d) a single-rim square ring; (e) a single-rim square ring with a quantum dot in center; (f) a double-rim square ring with a quantum dot in center; (g) a rectangular ring; and (h) a wire. The color represents the angle ϕ between the vertical direction and the normal vector of the surface, which ranges from light yellow for $\phi = 0°$ to brown for 11.3°.

4.4 Discussion

Although patterns are needed to activate the island formation in the ASKT method, the pattern sizes does not impose a lower limit on the feature length of the nanostructures. The feature length is controlled by the characteristic length L. This is demonstrated in Fig. 4.6 that patterns of different shapes and sizes on the same SK system with $L =$ 250 Å lead to nanostructures of similar feature length. It is further found in our simulation that the feature length decreases when L increases. This means that the feature length can be reduced by increasing the mismatch strain $\mathcal{E}_0$ in the SK system without changing the pattern size.

We only adopted a simple interaction mechanism to account for the SK transition in the project; however, the results would be similar when more realistic mechanisms of the film-substrate interaction are included. The key point here is that the critical thickness H_1 of the transition under spontaneous formation differs from H_2 under surface undulation, irrespective of the interaction mechanisms. The fundamental difference between H_1 and H_2 is the pivot of the ASKT method for the controlled self-assembly of nanostructures.

The difference between the H_1 and H_2 is indicated in the experimental observations; however, the importance of the idea still needs to be exploited in the future.

One of the important conditions for the realizing the ASKT method is to have large value of $H_2 - H_1$. This can be easily achieved when the surface energy density γ is a minimum in the film thickness direction. One example is the SiGe film on the Si(001) substrate (Tersoff et al. 2002). In such a case, reducing the process temperature would cause the minimum to be stronger, leading to higher H_2 and thus a larger value of $H_2 - H_1$.

Another issue in the ASKT method is whether or not the nucleation rate can be low. It is known that nucleation plays a significant role in the island formation of the SiGe systems with a large Ge concentration, particularly during the growth process. In such a case, the adatoms are abundant, and it is easy to have enough adatoms to diffuse by a short distance to form nuclei. The scenario, however, is different during an annealing process in the ASKT method. The adatom density is much lower, the probability at any

moment to have enough adatoms in such a short distance to form nuclei is extremely low. For example, when the adatom concentration x_a is 2%, the probability of gathering 180 Ge adatoms to form a pyramid nuclei of 5 nm is 0.02^{180}, less than 10^{-300}. The low adatom concentration during the annealing process results in a high kinetic barrier to suppress the nucleation mechanism in the ASKT method.

Chapter 5

Formation of Nanostructures by Surface Undulation

This chapter investigates the nanostructure formation of typical Stranski-Krastanow systems by simulating the surface undulation of the system driven by the surface diffusion mechanism. This chapter is organized as follows: Section 1 reviews the critical film thickness of typical SK system, Sec. 2 describes the approach that are adopted to study the nano-islands in this chapter, Sec. 3 presents the common features that are observed in our simulation, Sec. 4 examines the effect of key parameters of the SK system and Sec. 5 summaries the key morphological evolution processes in the SK system.

5.1 Introduction

5.1.1 Critical film thickness

As discussed in Chap 4, the SK systems can form faceted islands only when the film thickness exceeds a critical value. The critical thickness depends on whether the development of the faceted islands follows the spontaneous formation or the surface undulation (Chiu et al. 2004). The spontaneous formation means the faceted islands grow directly on the film surface by the mechanism of nucleation (Tersoff and Tromp 1993). The critical value

is called the first critical thickness, and it is given in Eq. (4.7). In contrast to the spontaneous formation, the surface undulation means the film first develops a slightly wavy surface before the surface transforms into faceted islands (Rastelli et al. 2003; Tersoff et al. 2002). The critical value is called the second critical thickness, and it is given by Eq. (4.9). The critical value H_2 is adopted in this thesis to normalize the film thickness and the quantity H_1,

$$\hat{H}_f = (H_f + l)/H_2, \tag{5.1}$$

$$\hat{H}_1 = H_1/H_2. \tag{5.2}$$

5.1.2 The fastest surface undulation mode

In the section, we employ the first-order boundary perturbation method to derive the fastest surface undulation mode due to surface diffusion (Chiu 1999a; Gao 1991a; Srolovitz 1989). We consider the case where the surface profile is described by a cosine curve $f(x,t) = A(t)\cos kx$ where $A(t)$ is the amplitude at time t and k is the wave number. For a shallow surface $Ak \ll 1$, the morphological evolution expressed in Eq. (2.7) can be simplified to (Srolovitz 1989)

$$\frac{\partial f}{\partial t} = D' \frac{\partial^2 \chi}{\partial x^2}, \tag{5.3}$$

where $D' = \Omega \rho_s D_s / k_B T_k$. The surface chemical potential χ is given by (Chiu 1999a)

$$\chi = \mu_0 + \Omega \left\{ w_{\sigma 0} + g'(H_f) + A \cos kx \left[\alpha \gamma_0 k^2 - 4 w_{\sigma 0} k + g''(H_f) \right] \right\},$$

according to the continuum model adopted in the thesis and assuming $g(H_f)/\gamma_0 \ll 1$.

Substituting Eq. (5.4) into (7.30) yields the evolution equation for the amplitude $A(t)$ of the cosine surface,

$$\frac{dA}{dt} = CA, \tag{5.4}$$

$$C = -D' \left[\alpha\gamma_0 k^4 - 4w_{\sigma 0} k^3 + g''(H_f) k^2 \right]. \tag{5.5}$$

The solution of $A(t)$ can be found to be $A(t) = A_0 \exp(Ct)$ where A_0 is the amplitude at $t = 0$. The result indicates the amplitude $A(t)$ varies exponentially with the quantity Ct, which depends on the wave number k. The wave number k_0 resulting in the largest C corresponds to the fastest surface undulation mode under the surface diffusion mechanism.

The value of k_0 can be obtained by solving the equation $dC/dk = 0$,

$$k_0 = \frac{3 + \sqrt{9 - 2\alpha \hat{g}''(H_f) L^2}}{4\alpha L}, \tag{5.6}$$

where $\hat{g}''(H_f) = g''(H_f)/\gamma_0$. By evoking the definitions of $\hat{g}''(H_f)$, $\hat{H}_f$, H_2, and k_0 can be rewritten as

$$k_0 = \frac{3 + \sqrt{9 - 8\hat{H}_f^{-3}}}{2\alpha L}. \tag{5.7}$$

The wavelength λ_0 of the fastest mode is thus

$$\lambda_0 = \frac{2\pi}{k_0} = \frac{4\pi\alpha L}{3 + \sqrt{9 - 8\hat{H}_f^{-3}}}. \tag{5.8}$$

The values of α are briefly discussed as follows. For the case where $\gamma(\mathbf{n})$ is uniform in the vicinity of (001), $\gamma_1 = \gamma_0$, $K = \partial^2\gamma/\partial\phi^2 = 0$, and $\alpha = (\gamma_1 + K)/\gamma_0 = 1$. For the case where γ contains a shallow minimum on (001), the value of K can be significantly high even though the surface energy density γ_1 on (001) is only lowered by a nominal value. This means that $\alpha > 1$ when a minimum of γ on (001) is introduced, and α increases with the strength of the minimum.

5.2 Model and Methodology

5.2.1 Approach

We adopt the continuum model described in Chap. 3 to study the nanostructure formation effected by the surface undulation on the SK systems. The film thickness is higher than the critical value for surface undulation. and the initial surface $f(x, y, 0)$ is taken to be an almost flat profile with some random roughness.

The nanostructure formation considered here is controlled by three nondimensional parameters: the characteristic length ratio $\mathcal{F} = \hat{g}_0 l/L$, the normalized film thickness $\hat{H}_f$, and the NESE density α [defined in Eq. (2.2)]. The ratio $\mathcal{F}$, representing the normalized strength of the interaction energy, controls the SK transition, the wetting layer formation, and the stability of islands against coarsening. The normalized thickness $\hat{H}_f$ is related to the amount of film material that can be transformed into islands, and the NESE density α determines the effect of $\gamma(\mathbf{n})$ on the surface undulation process. The formation is also affected by the minimum of γ on $\{105\}$, $\{113\}$, and $\{15\ \ 3\ \ 23\}$. The minimum is included in our simulations, while the magnitude of the minimum is fixed.

A major part of our investigation is based on a parametric study of $\mathcal{F} = \hat{g}_0 l/L$ with the other two parameters of the SK systems being fixed: $\hat{H}_f = 1.3$ and $\alpha = 1$. The choice of α implied γ is uniform in the vicinity of (001). The cases in the parametric study are listed in Table 5.1. Each case is labeled by a letter followed by an integer. The letter, ranging from I to M, refers to the ratio $\mathcal{F}$ of the case: The ratio $\mathcal{F}$ of the I, J, and K cases are small, causing pyramids to be unstable against coarsening. On the contrary, those of the L and M cases are sufficiently high to stabilize the coarsening. The integer following the letter refers to the value of $\hat{g}_0 l$. The number is 1, 2, and 3 when $\hat{g}_0 l = 0.25$, 0.0625, and 0.01563 Å respectively.

The I, J, and K cases of the parametric study are first analyzed in the following sections to reveal the common features of the formation of faceted nanostructures on the coarsening SK systems. The common features lead to a simple model for determining

Table 5.1: The values of $\hat{g}_0 l$ and L of the cases considered in the parametric study.

$\hat{g}_0 l$ (Å)	L (Å)				
	16000	4000	1000	250	62.5
0.25	I1	J1	K1	L1	M1
0.0625		I2	J2	K2	L2
0.01563			I3	J3	K3

the effects of $\{F, H_f, \alpha\}$ on the maximum surface coverage ξ_{max} in Sec. 5.4. After understanding how $\mathcal{F}$, $\hat{H}_f$, and α affect ξ_{max}, Section 5.5 turns to numerical simulation that illustrates the effects of ξ_{max} on the film surface profile during the nanostructure formation. The simulation includes the cases in Table 5.1 and those with different values of $\hat{H}_f$ and α.

5.3 The Common Features

The common features of the nanostructure formation on the coarsening SK systems can be summarized as follows.

1. The essence of the nanostructure formation process is the transformation of the film material above the wetting layer into faceted islands.

2. The wetting layer thickness is equal to the first critical thickness for the SK transition.

3. The nanostructure width measured at the average film height is close to a constant during the formation process.

The common features are observed by comparing the morphological evolution of the I, J, and K cases. An example of the comparison is shown in Fig. 5.1 for Cases I2, J2, and K2. The three cases are arranged in three rows which contain five sub-figures. The first four illustrate how the film morphology changes as the surface coverage of faceted islands increases to the maximum value. The fifth one plots the film cross-sections along the solid line shown in the first sub-figure at four time steps.

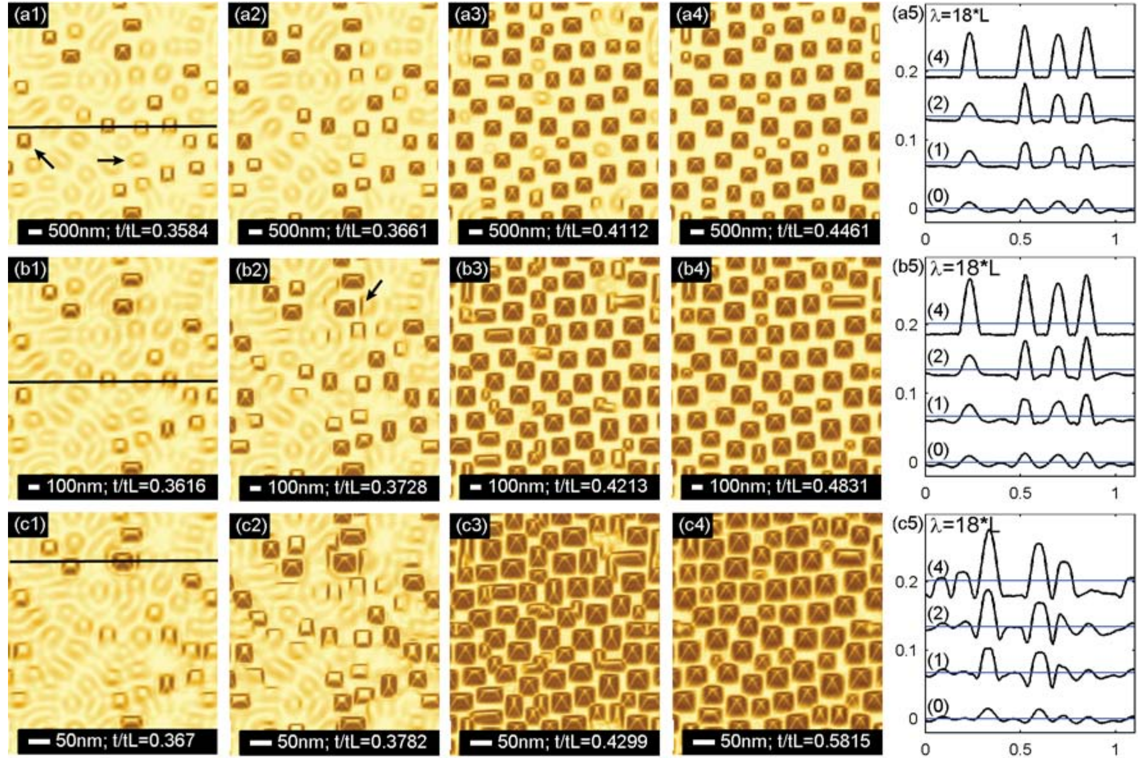

Figure 5.1: The morphological evolution of (a1–a5) Cases I2, (b1–b5) Case J2, and (c1–c5) Case K2. In (a5), (b5), and (c5), Line (0) is from the result prior to the emergence of faceted islands, and Lines (1), (2), and (4) are obtained from the first, second, and fourth sub-figures of the corresponding case. In (a5), (b5), and (c5), the horizontal lines represent the average film height.

5.3.1 The formation process on the coarsening SK systems

Figures. 5.1(a1)–5.1(a5) show a typical example of the nanostructure formation effected by the surface undulation. The film first develops a wavy profile containing shallow bumps and valleys, see Fig. 5.1(a1). The bumps then undergo a shape transition from smooth structures, to faceted islands with rounded tops, and finally to pyramids, see the arrows in Fig. 5.1(a1). The bump-pyramid transition shown in the simulation is consistent with the experimental observations reported in the literature (Rastelli et al. 2003; Tersoff et al. 2002).

As the bumps and the pyramids form on the film, the film material is transported from the valleys toward the islands by surface diffusion. This causes the valleys to deepen and evolve into a flat wetting layer, see Fig. 5.1(a5).

Similar island formation process, characterized by the growth of a wavy surface profile,

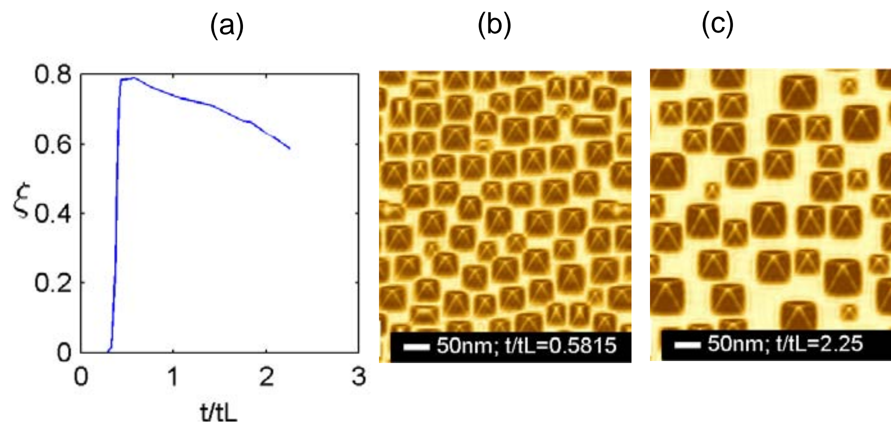

Figure 5.2: The evolution of the surface coverage ξ of the faceted islands during the morphological evolution of Case K2, (b) the film surface profile at the maximum surface coverage, and (c) the film surface profile at the stage of island coarsening.

the shape transition, and the development of a flat wetting layer, is observed in all of the I, J, and K cases. This confirms the first common feature that the nanostructure formation of the coarsening SK systems can be depicted as the transformation of film material above the wetting layer into faceted islands. The essence of the first feature is similar to that of barrierless island formation during the deposition process (Tersoff et al. 2002). The two processes, however, differ significantly in the kinetic pathways.

Besides the film morphology and the cross-sections shown in Fig. 5.1, the island formation process can also be visualized by the evolution of the surface coverage ξ of the faceted islands. One example is depicted in Fig. 5.2(a) for Case K2. The result indicates the coverage ξ is zero at the initial stage of the formation process when the film surface is dominated by shallow bumps and valleys. After the initial stage, the coverage ξ increases drastically, reaches a maximum, and then declines gradually. The fast increase of ξ signals the bump-pyramid transition, while the decrease of ξ is caused by the island coarsening process after the islands and the wetting layer form. During the coarsening process, bigger islands grow bigger, and smaller ones become smaller and then disappear. The nature of the coarsening process is evidently shown in the comparison between Figs. 5.2(b) and 5.2(c) where the former plots the film profile with the maximum surface coverage of faceted islands and the latter depicts that at the later stage of the morphological evolution

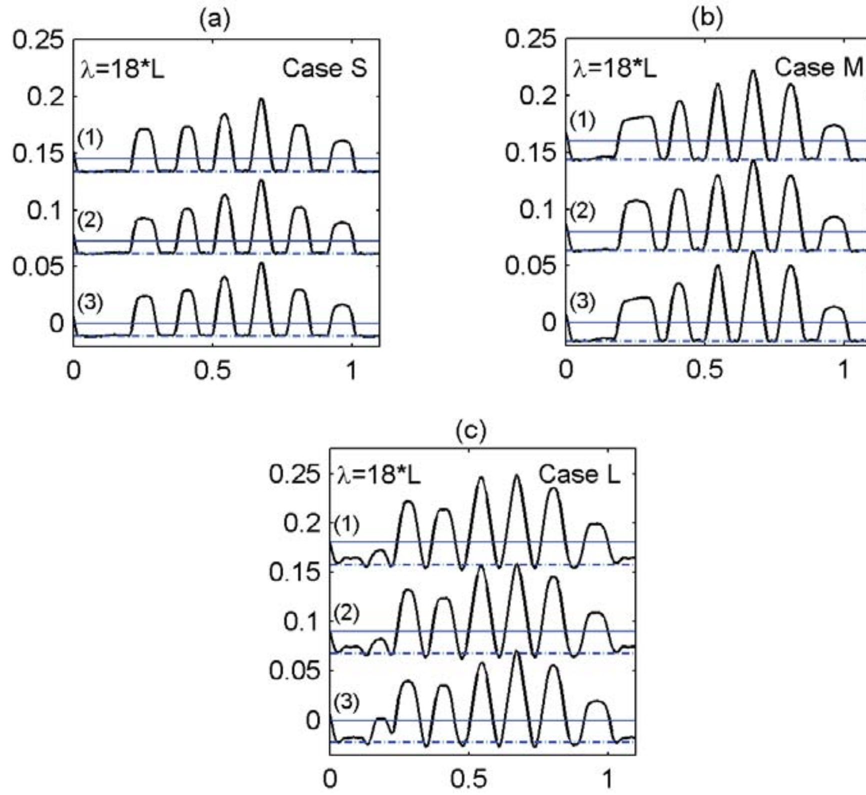

Figure 5.3: The cross-section profiles of the (a) I, (b) J, and (c) K cases examined in Table 5.1 when the island surface coverage ξ reaches the maximum.

5.3.2 The wetting layer thickness

Figures 5.3(a), 5.3(b), and 5.3(c) plot the cross-sections of the I, J, and K cases, representing when the faceted island surface coverage attains the maximum. The horizontal dash-dotted lines in the figure indicate the average film height, and the dash-dotted lines correspond to the first critical thickness. The dash-dotted lines are found to coincide well with the wetting layer surface, demonstrating the second common feature.

The second feature can be understood as follows. The first critical thickness, given in Eq. (4.7), refers to the film thickness below which the formation of a pyramid island of any size is energetically unfavorable (Chiu et al. 2004). This means the portion of the film below the first critical thickness cannot develop into islands, and this portion will remain a flat layer. In contrast, the portion of the film above the first critical thickness is unstable

against island formation, and this portion will gradually transform into islands. The different characteristics of the two portions of the film lead to the tendency to develop a flat wetting layer during the formation of nanostructures. The second feature is independent of the type of wetting potential in the SK system.

The second feature suggests that the first critical thickness for the SK transition can be determined by measuring the wetting layer thickness after the annealing process. This is a potentially simpler and more reliable scheme than the conventional method, where the critical thickness is obtained by observing the SK transition during the film growth process, a challenging task if the islands form via a gradual barrierless process.

As a remark, Eq. (4.7) suggests that the critical thickness H_1 for island formation and the wetting layer thickness decrease when the characteristic slope $\mathcal{S}$ of the island increases. Hence, the wetting layer thickness for the dome islands, characterized by the {113} facets, is smaller than that of the {105} pyramids. This explains the observations in experiments that there is a shallow valley around the dome islands (Medeiros-Ribeiro et al. 1998; Rastelli et al. 2001).

5.3.3 The island width

The island width is investigated by examining the evolution of the film surface cross-sections depicted in Figs. 5.1(a5), 5.1(b5), and 5.1(c5). Of particular importance are the interception points of the cross-sections and the horizontal lines at the average film height. These points determine the nanostructure width d_0 measured at that height. It is found that the width d_0 does not change significantly during the formation of nanostructures. The finding can be observed in all of the cases shown in Fig. 5.1. The island width d_0 at the average film height is termed the basic width in the thesis.

5.3.4 The formation of faceted island

The three features together describe how nanostructures form on the SK system during the annealing process. The process starts with the growth of a wavy surface, see Fig. 5.4(a).

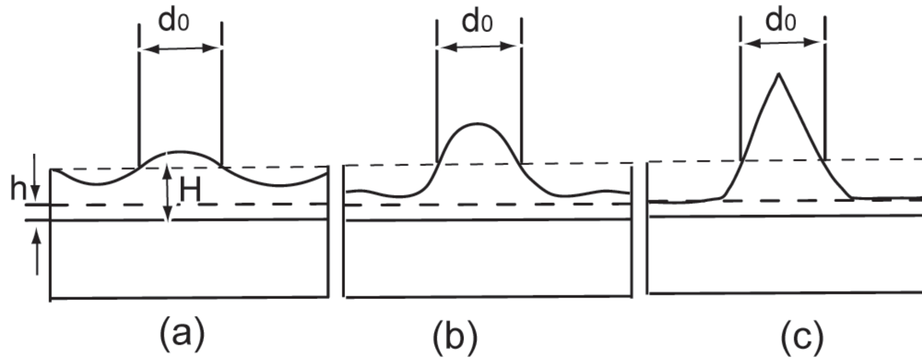

Figure 5.4: The schematic diagram of the general island formation process that consists of surface undulation, bump pyramid transition, and wetting layer development. The basic width d_0 of the island approximates to a constant even though the shape of the island changes significantly during the formation process.

As the amplitude of the wavy surface increases, faceting is triggered at the average film height since the slope of the surface is the highest there, see Fig. 5.4(b). After the facet is initiated, the facet develops quickly in the lateral direction of the facet, resulting in a fully developed pyramid. The process continues until all of the film material above the first critical thickness is transformed into islands, leading to a flat wetting layer, see Fig. 5.4(c).

This common feature can be understood by the general nanostructure formation process depicted in Fig. 5.4. The process starts with undulation of the film surface. As the amplitude of the wavy surface increases, faceting is triggered at the average film height since the slope of the slightly wavy surface is highest there. This explains why the basic width of the shallow bump is similar to that of the truncated pyramid.

5.3.5 Comparison

Strictly speaking, the surface profiles in Figs. 5.1(a5), 5.1(b5), and 5.1(c5) are not perfect facets, raising a question of the applicability of the third feature to the case of perfect facets. To answer the question, we first compared our simulations with those in the

Table 5.2: The maximum surface coverage and the island base width obtained by numerical simulation (d_{num} and ξ_{num}) and those predicted by Eqs. (5.11) and (5.12) (d_{th} and ξ_{th})

Case	d_{num} (Å)	ξ_{num}	d_{th} (Å)	ξ_{th}
I1	2.13×10^4	0.44	2.20×10^4	0.43
I2	5.32×10^3	0.44	5.51×10^3	0.43
I3	1.33×10^3	0.44	1.38×10^3	0.43
J1	5.68×10^3	0.60	5.86×10^3	0.58
J2	1.42×10^3	0.60	1.47×10^3	0.58
J3	3.54×10^2	0.60	3.66×10^2	0.58
K1	1.51×10^3	0.79	1.58×10^3	0.76
K2	3.73×10^2	0.80	3.95×10^2	0.76
K3	9.35×10^1	0.80	9.88×10^1	0.76

literature studying perfect facets. It is found that those results also revealed fast facet growth in the lateral direction even though there is no stress in the systems (Liu and Metiu 1993).

In addition to the literature results, we also compared d and ξ_{max} obtained from the numerical simulations with those predicted by Eqs. (5.11) and (5.12), which are derived later in Sec. 5.4. The results are listed in Table 5.2 for all of the I, J, and K cases. In the table, d_{num} and ξ_{num} refer to the simulation results; d_{th} and ξ_{th} are the values predicted by Eqs. (5.11) and (5.11), respectively. The simulation results agree well with the predicted values. The good agreement suggests the third feature is applicable to the cases of perfect facets.

5.4 The Maximum Surface Coverage ξ_{max} of Faceted Islands

5.4.1 Derivation of ξ_{max}

The faceting process shown in Fig. 5.4 suggests a simple model for estimating the average base width d of faceted islands when the faceted islands have fully developed and the

island surface coverage reaches the maximum $\xi_{\max}$,

$$d = d_0 + \frac{2(H_f - h)}{\tan\phi}, \tag{5.9}$$

where H_f is the film thickness and h is the wetting layer thickness equal to the first critical thickness. The basic width d_0 in Eq. (5.9) is half of the wavelength λ_0 given in Eq. (5.8). Similarly, the difference $H_f - h$ in Eq. (5.10) can be obtained by evoking Eqs. (4.7), (4.9), (5.1) and (5.2),

$$\frac{H_f - h}{L} = \frac{H_2\hat{H} - H_1}{L} = \sqrt[3]{\frac{\alpha\mathcal{F}}{2}}\hat{H}_f - \sqrt{\frac{\mathcal{F}}{U_0\mathcal{S}}}. \tag{5.10}$$

Substituting Eqs. (5.9) and (5.10) into (5.9) yields (5.11)

$$\frac{d}{L} = \frac{2\pi\alpha}{3 + \sqrt{9 - 8\hat{H}_f^{-3}}} + \frac{2}{\tan\phi}\left(\sqrt[3]{\frac{\alpha\mathcal{F}}{2}}\hat{H}_f - \sqrt{\frac{\mathcal{F}}{U_0\mathcal{S}}}\right). \tag{5.11}$$

With the knowledge of $H_f - h$ and d, the maximum surface coverage $\xi_{\max}$ of faceted islands can be determined by

$$\xi_{\max} = \frac{6}{\tan\phi}\frac{H_f - h}{d}. \tag{5.12}$$

Equations (5.9)–(5.12) indicate the dependence of $\xi_{\max}$ on $\mathcal{F}$, $\hat{H}_f$, and α.

Equation (5.12) may predict $\xi_{\max} > 1$. This means the wetting layer depth $H_f - h$ is so large that the faceted island bases cannot reach the wetting layer after the shape transition from a smooth profile to faceted nanostructures. In such cases, the nanostructures cover the whole film surface after the shape transition and $\xi_{\max} = 1$.

5.4.2 The effects of $\mathcal{F}$, $\hat{H}_f$, and α on $\xi_{\max}$

The effects of $\mathcal{F}$, $\hat{H}_f$, and α on $\xi_{\max}$ are illustrated in Fig. 5.5. In particular, Fig. 5.5(a) depicts the variation of $\xi_{\max}$ with $\hat{H}_f$ for the I, J, and K cases, where $\mathcal{F} = 1.56 \times 10^{-5}$,

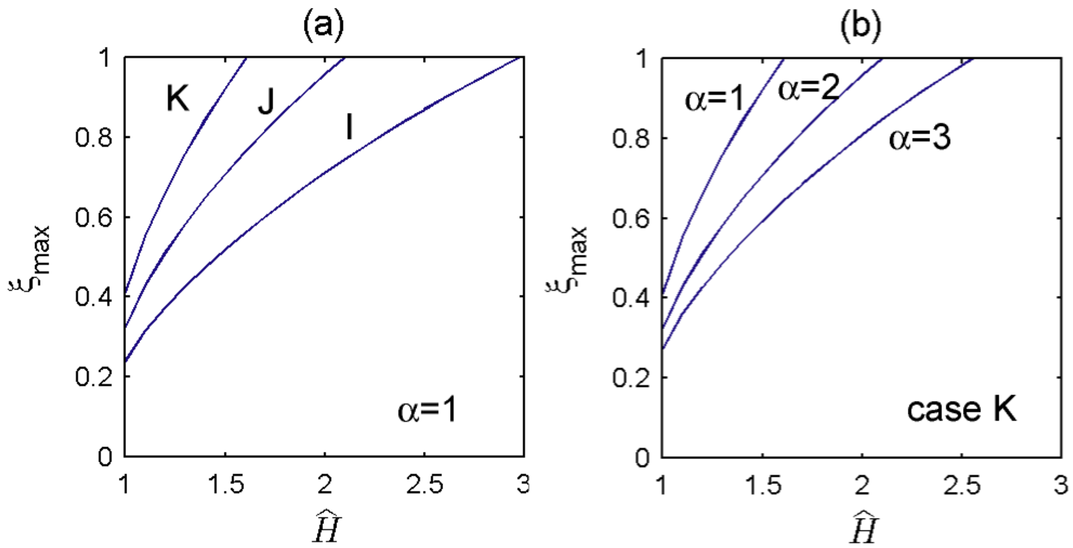

Figure 5.5: (a) The variation of $\xi_{\max}$ with $\hat{H}_f$ at $\alpha = 1$ for the I, J, and K cases, and (b) that with $\hat{H}_f$ at $\alpha = 1$, 2, and 3 for the K cases.

6.25×10^{-5}, and 2.5×10^{-4}, respectively, and $\alpha = 1$. The results show that $\xi_{\max}$ increases with $\mathcal{F}$ and $\hat{H}_f$. Figure 5.5(b) shows the effect of α on $\xi_{\max}$ by plotting the variation of $\xi_{\max}$ with $\hat{H}_f$ at three different values of α. Comparing the results of the three cases suggests that $\xi_{\max}$ is reduced when α increases. This implies a minimum of γ on (001) favors an array of sparse islands during the formation process.

Figure 5.5 can be further understood as follows. First, a higher value of $\hat{H}_f$ means more film material can transform into islands; hence, the maximum island surface coverage $\xi_{\max}$ increases. Second, as suggested in Eqs. (5.10) and (5.11), raising the ratio $\mathcal{F}$ results in more film material for island formation and larger island size. The effect on the former, however, is stronger, thus leading to a higher $\xi_{\max}$. Third, increasing α also causes more film material for island formation and larger island size, while the effect on the island size is stronger in the current case. Accordingly, $\xi_{\max}$ decreases when α increases.

As a remark, Eqs. (5.10)–(5.12) are valid only when the stability number Σ is negative. If $\Sigma > 0$, the coarsening of islands is stabilized and the wetting layer thickness is different from the first critical thickness (Chiu 2004); consequently, $(H_f - h)/L$ cannot be given by $(\hat{H}_f H_2 - H_1)/L$ as suggested in Eq. (5.10). Although it is beyond our capability to derive a simple expression for $\xi_{\max}$ of the stable SK systems, the simulation results in our

parametric study seem to indicate that the maximum surface coverage of faceted islands on the stable SK systems is high.

In short, Eqs. (5.10)–(5.12) show it is the characteristic length ratio $\mathcal{F}$, the normalized film thickness $\hat{H}_f$, and the NESE density α that determine the maximum surface coverage $\xi_{\max}$ of faceted islands. It becomes clear in the next section that the quantity $\xi_{\max}$ in turn controls the film surface profiles during the nanostructure formation.

5.5 The Film Morphologies

The film morphologies observed in our simulation can be classified into three types: (1) an array of separate islands, (2) localized wetting layers and induced facets, and (3) a faceted ripple structure. The film surface profile changes gradually from Type 1 to Type 2 and then to Type 3 when $\xi_{\max}$ increases. The three types of morphology and the effects of $\xi_{\max}$ on the film morphologies are discussed in this section.

5.5.1 An array of separate islands

An example of this type of film morphology can be found in Figs. 5.1(a1)–5.1(a5) for Case I2. The morphology is characterized by sparse pyramid islands. It is also observed that the wetting layer in this case has largely developed at the onset of the shape transition from bumps to pyramid islands, see Figs. 5.1(a1) and 5.1(a5).

This type of film morphology appears when $\xi_{\max}$ is low. For example, $\xi_{\max} = 0.43$ in Case I2. A low value of $\xi_{\max}$ means the wetting layer depth $H_f - h$ is much smaller than the height of the pyramid island $(d \tan \phi)/2$; accordingly, it takes less time for the wetting layer to form than the pyramid islands. This explains the relatively flat wetting layer at the onset of the bump-pyramid transition. The low surface coverage also implies that the bump-pyramid transition of an island can seldom activate another transition in the neighboring area. Therefore, most of the pyramid islands in this case form individually without a particular sequence.

The shape of islands in this type of film morphology is mainly pyramids with a square base. This is consistent with the result that the total energy of the pyramid is lower than elongated ridges and truncated huts of the same volume (Chiu and Poh 2005; Tersoff and Tromp 1993).

5.5.2 Localized wetting layers and induced facets

The second type of film morphology can be found in Figs. 5.1(b1)–5.1(b5) and 5.1(c1)–5.1(c5), the results of Cases J2 and K2, respectively. The distinguishing features of the morphology are the localized wetting layers and induced facets highlighted by the arrows in Figs. 5.1(b2).

This type of morphology occurs when $\xi_{\max}$ is high. In such cases, the wetting layer depth $H_f - h$ is higher and the wetting layer formation is slower. As a consequence, when some of the bumps start to transform into pyramids, the wetting layer has not developed, and the film surface still comprises mainly valleys and bumps, see Figs. 5.1(b1) and 5.1(c1). The emergence of the pyramids results in a higher stress gradient in the vicinity of the island base, causing the film material to be quickly transported away from the valleys to the pyramids and the nearby bumps. This leads to the two distinguishing features of this type of morphology: The removal of the material from the valleys results in the localized wetting layers around the pyramids; the accumulation of the material on the nearby bumps causes the bumps to develop facets on the sides facing the pyramids. The considerable influence of the existing islands on the subsequent faceting process also explains why there are more elongated islands in this type of morphology than in the first type.

The morphological evolution of the third case is plotted in Figs. 5.1(c1)–5.1(c5). The characteristics of the evolution are similar to those in the second case: the development of a wetting layer around a faceted island, the induced faceting on the neighboring bumps, and a higher percentage of non-pyramid islands. The difference between the two cases is that in the current case the island surface coverage ξ is higher.

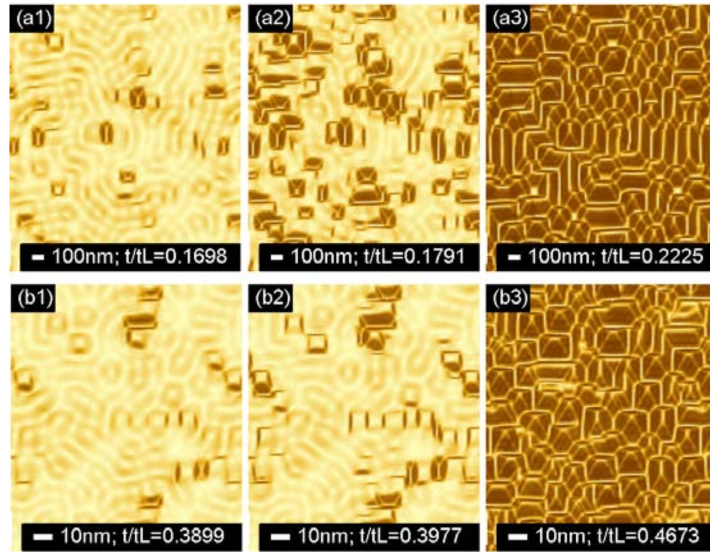

Figure 5.6: The morphological evolution of the faceted ripple structures due to (a1)–(a3) a high $\hat{H}_f$ and (b1)–(b3) a large value of $\mathcal{F}$. In (a1)–(a3) the material properties are given by those of the J2 case with $\hat{H}_f = 3$, and in (b1)–b(3) the material properties correspond to the M1 case with $\hat{H}_f = 1.3$

5.5.3 The faceted ripple structure I

The faceted ripple structure is observed in the SK systems with $\xi_{\max}$ being close or equal to one. As shown in Sec. 5.4, this happens when the normalized film thickness $\hat{H}_f$ and/or the characteristic length ratio $\mathcal{F}$ is large.

Figure 5.6(a1)–5.6(a3) plots an example of the ripple structure on a thick film. The material properties in the example are identical to those of Case J2, while $\hat{H}_f$ is increased to 3. Figure 5.6(a1) indicates that the nanostructure formation at large $\hat{H}_f$ is similar to that at small $\hat{H}_f$, also following the process of the growth of a wavy profile and the shape transition from the wavy profile to faceted nanostructures. The shape transition at high $\hat{H}_f$, however, is mainly from valleys to trenches/pits, instead of from bumps to pyramid islands.

After the shape transition, the pits and the trenches facilitate the growth of pyramids and ridges at the adjacent sites, see Fig. 5.6(a2). The process is called the cooperative nucleation in the literature (Jesson et al. 1996). As implied by the term, the cooperative nucleation is thought to be effected by nucleation. Our simulation, however, shows that the process can also result from the surface undulation. To highlight the different mecha-

nism, the process caused by the surface undulation is termed the cooperative formation. The cooperative formation is the kinetic pathway of the faceted ripple structure. The cooperative formation is further studied in the next chapter.

Figure 5.6(a3) depicts the faceted ripple structure after the nanostructures have fully developed, showing two characteristics of the morphology. First, the faceted ripple structure is a network of ridges and trenches covering the whole film surface. Second, the shapes of the nanostructures can be irregular because of the cooperative development of the trenches and the islands. The nanostructures are still defined by the {105} facets, while the shapes can be an L, U, T, or staircase. The two characteristics are consistent with the experimental observations in the literature (Ozkan et al. 1997; 1999), which studied a thick $Si_{0.78}Ge_{0.22}$ film on a Si substrates during the annealing process.

It is necessary to explain the intriguing finding in Figs. 5.6(a2) and 5.6(b2) that the trenches are the major surface structures at the early stage of the island formation process on a thick film even though, from the energy point of view, the trench formation is less favorable than the pit formation when the facet angle is small (Chiu and Poh 2005; Tersoff and Tromp 1993). The substantial trench formation is caused by the random roughness on the initial surface profile. During the surface undulation process, the random roughness leads to a wavy profile with many long valleys; it is the long valleys that trigger the trench formation. When the long valleys are suppressed in the initial surface profile, the formation process is dictated by the valley-pit transition.

5.5.4 The Faceted Ripple Structure II

Figures 5.6(b1)–5.6(b3) plot the morphological evolution of Case M1 with $\hat{H}_f = 1.3$. This is an example of the faceted ripple structure due to a large value of $\mathcal{F}$, and the corresponding SK system is stable against island coarsening. The results indicate the formation of the current faceted ripple structure is similar to that due to large $\hat{H}_f$: The formation process in both cases consists of the surface undulation, the shape transition, and the cooperative formation. In addition to the process, the morphologies of the two

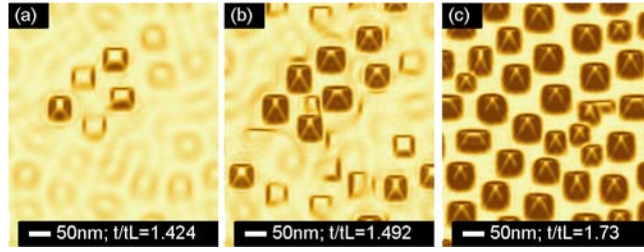

Figure 5.7: The morphological evolution of the SK system, where L = 250 Å, $\hat{g} = 0.0625$, $\alpha = 1.5$, and $\hat{H}_f = 1.3$

faceted ripple structures are also similar, which can be described as a network of faceted islands and trenches of various shapes.

The major difference between the two cases in Fig. 5.6 is the faceted structures developing from the shape transition at the initial stage of morphological evolution. In the case of high $\hat{H}_f$, the structure induced by the shape transition is the trenches; in contrast, the structure is the pyramid islands when $\mathcal{F}$ is high but $\hat{H}_f$ is low. Because of the difference, the cooperative formation of the former follows the trench-island sequence, while the latter follows the island-trench sequence. The difference also accounts for the finding that the fraction of the irregular islands/ridges of the former is higher than that of the latter.

The cooperative formation illustrated in Fig. 5.6 lacked the characteristic suggested in literature (Gray et al. 2004c; Jesson et al. 1996) that the process alternated between the emergence of islands and the development of trenches. This is mainly caused by the random roughness adopted in the initial surface profile, which yielded a higher density of islands or trenches at the initial stage. It is shown later in Chap. 6 that when the density is reduced by introducing a holes on a smooth surface, the ordered growth of islands and trenches became evident.

5.5.5 The nanostructure formation under the influence of a minimum of γ

The effect of a minimum of γ on (001) is examined by simulating the SK system that is the same as Case K2 except that α is increased to 1.5. The results, depicted in Figs. 5.7(a)–5.7(c), are then compared with those of Case K2 illustrated in Figs. 5.1(c1)–5.1(c5). The comparison indicates a higher value of α leads to larger islands, smaller $\xi_{\max}$, and accordingly a sparse island array. The finding confirms the prediction shown in Fig. 5.7(b).

5.6 Summary

The formation of islands effected by the surface undulation on the coarsening SK systems can be described as a gradual process to transform the portion of the film above the first critical thickness into islands. The process is characterized by the growth of a wavy profile, the shape transition from the wavy profile to faceted nanostructures, and the tendency to form a flat wetting layer at the first critical thickness. A unique property of the shape transition is that the variation of the island basic width is negligible during the transition.

Three types of film morphology can appear in the nanostructure formation process: (1) an array of separate islands, (2) localized wetting layers and induced facets, and (3) a faceted ripple structure. The film morphology is controlled by the maximum surface coverage $\xi_{\max}$ of faceted islands. As $\xi_{\max}$ increases, the film morphology changes gradually from the sparse array to the localized wetting layers and finally to the faceted ripple structure.

The crucial quantity $\xi_{\max}$ depends on three parameters of the SK systems, namely, the characteristic length ratio $\mathcal{F}$, the normalized film thickness $\hat{H}_f$, and the NESE density α. It is found that $\xi_{\max}$ increases with $\mathcal{F}$ and $\hat{H}_f$, while $\xi_{\max}$ is reduced as α increases.

As a remark, different assumptions for the interaction mechanisms will affect the details of the results; however, the essence of the nanostructure formation effected by the surface undulation would be similar. Irrespective of the interaction mechanism, the

formation process is still characterized by the surface undulation, the shape transition, and the tendency to form a wetting layer at the first critical thickness; the basic width is given by the fastest surface undulation mode, varying little during the process; and the film morphology is determined by the maximum surface coverage $\xi_{\rm max}$ of faceted islands.

Chapter 6

Self-Assembly of Quantum Dot Molecules by Cooperative Formation

This chapter investigate another important phenomenon observed in typical SK system, namely, the formation of quantum dot molecules on a thick film. Our investigation starts with numerical simulation for the morphological evolution of strained film-substrate system driven by surface diffusion. The results demonstrate that the surface undulation process on a thick film leads to the unique cooperative formation of faceted trenches and ridges. The cooperative formation mechanism is further explored from the energetic point of view by considering the crucial moment when the formation of a facet island adjacent to a trench becomes a barrierless process more favorable than the growth of the trench itself. The critical trench size for favorable growth of adjacent facet island suggests that alternative development of trenches and ridges is a self-limiting process dictating the size selection of quantum dots molecules.

6.1 Introduction

Rippling on solid surfaces at the length scale of nanometers is a remarkable phenomenon of self-assembly. The phenomenon was observed in literature by annealing a $Si_{0.5}Ge_{0.5}$ alloy film of 5 nm in thickness on a thick Si substrate at temperatures ranging from 570

to 590 °C (Jesson et al. 1996). The result revealed that the film developed into nanoridges and nanotrenches via a cooperative manner that the two types of nanostructures formed one after another at the adjacent sites. The cooperative ridge-trench (CRT) formation continued, resulting in a ripple structure. The ripples are characterized by the same type of facet but could exhibit a variety of different shapes. Similar ripple structures are also found in other SiGe films (Ozkan et al. 1997; 1999) and in the InGaAs/GaAs system (Chokshi et al. 2002; Chokshi and Millunchick 2000).

Subsequent to the observation, the CRT formation is realized to be a useful mechanism for self-assembling quantum-dot molecules (QDMs) on heteroepitaxial systems (Deng and Krishnamurthy 1998). The fabrication process of the QDMs consisted of two steps. The first step is to generate shallow holes on solid surfaces by embedding a small amount of hard particles in a buffer layer prior to the deposition of a heteroepitaxial film (Borgström et al. 2003; Deng and Krishnamurthy 1998; Weil et al. 1998). The shallow holes would trigger the CRT formation on the film in the second step, causing the self-assembly of QDMs around the holes. The QDMs generated by this process are clusters of dots with the number of dots being adjustable (Songmuang et al. 2003). The size distribution of the QDMs is much more uniform than that of single quantum dots. These advantages, namely, self-assembly, unique structures, adjustable number of dots, and uniform size distribution, suggest that the QDMs are a promising building block for quantum computation devices (Barth et al. 2005).

In addition to the two situations mentioned above (Deng and Krishnamurthy 1998; Jesson et al. 1996), the CRT formation also happened on heteroepitaxial films during the deposition process. This issue is examined in a series of papers aiming at understanding the dependence of the CRT formation on the growth rate, the substrate temperature, the film thickness, and the interrupting annealing during the process (Gray et al. 2004a; 2002; 2004b; 2005; 2004c; Vandervelde et al. 2003). Those papers focused on the $Si_{0.7}Ge_{0.3}$/Si system, and the key findings can be summarized as follows. (1) At 550 °C and a growth rate of 0.09 nm/s, the film morphology developed shallow indents and then QDMs via the CRT formation (Gray et al. 2002). The QDMs are mainly quantum fortresses, char-

acterized by a {105} ring surrounding a square pit with the same type of facet. (2) At the same 550 °C but a much slower growth rate (0.015 nm/s), no shallow indent is found, and the film morphological evolution led to a ripple structure when the film thickness reached 30 nm (Gray et al. 2002). The ripple structure is similar to that observed in literature (Jesson et al. 1996). (3) Increasing the temperature to 750 °C with similarly low growth rates caused nanoislands to form at small thickness (3 nm); the islands grew and coalesced as the film thickness increased (Floro et al. 1997; Gray et al. 2005). (4) The development of quantum fortresses from the shallow indents is prevented when the fast film growth at 550 °C is interrupted by annealing at the same temperature; instead of quantum fortresses, the indents evolved into elongated trenches (Gray et al. 2004b).

The CRT formation is generally explained by the cooperative nucleation model in the literature (Jesson et al. 1996). The model argues that the presence of one type of structure (e.g. a trench) can reduce the energy barrier for the nucleation of the other type (e.g. an island) at the adjacent site, thus facilitating the repeating occurrences of the two types of structures. The energy reduction can come from the mismatch strain in the film (Jesson et al. 1996) or the adatom concentration on the film surface (Bouville et al. 2004)

The cooperative nucleation model points out the significant effects of an existing nanostructure on the nucleation of a different one. The nucleation model, however, cannot fully account for the ordered morphology and the uniform size distribution of the QDMs generated by the pitted buffer layer (Deng and Krishnamurthy 1998) and by the fast film deposition (Gray et al. 2002). Furthermore, nucleation requires spontaneous accumulation of a large amount of adatoms at the adjacent sites, and there is an energy barrier during the process. The difficulty in nucleating new structures at the adjacent sites suggests the CRT formation may be dictated by a different mechanism.

The CRT formation is examined in this thesis by considering two issues. First, instead of nucleation, the adjacent new structure may develop gradually via the surface undulation process. The surface undulation process, driven by surface diffusion, is another mechanism of the morphological evolution of the film surface. The process is characterized by a

gradual change of the surface profile, and the process can lead to the formation of faceted islands without experiencing an energy barrier (Chiu and Huang 2006; 2007; Tersoff et al. 2002). These unique features suggest that the surface undulation process can play an important role in the development of the adjacent new structure. Second, the gradual development of the adjacent new structure has to compete with the growth of the existing outermost one. The competition between the two pathways is the key to the alternative growth of ridges and trenches during the CRT formation (Huang et al. 2007).

In this chapter, the two issues are studied by simulating the surface undulation process and by analyzing the energy difference between the two pathways of the CRT formation. The results confirm that the CRT formation can happen during the surface undulation process on a thick film and is caused by the competition between the two pathways. In particular, the growth of the existing outermost structure dictates the process initially when the size of the outermost structure is small. However, once the size reaches a critical value, the gradual development of a new structure adjacent to the outermost one becomes the more energetically favorable pathway. The critical size differentiating the two pathways explains the alternative growth of ridges and trenches in the CRT formation. The critical size also accounts for the uniform size distribution of the ripple structures and QDMs.

This chapter is organized as follows. Section 6.2 shows the simulation results for the alternative growth of ridges and trenches and the formation of QDMs. Section 6.3 presents the energy analysis for the two competing pathways that cause the CRT formation. Section 6.4 summarizes the results of this chapter and discusses the limitations of the model adopted in this chapter.

6.2 Numerical Simulation for the CRT Formation

This section presents numerical simulation results of the CRT formation. In particular, we simulate the surface undulation of three cases of $Si_{0.7}Ge_{0.3}$ films driven by the surface diffusion mechanism described in Chapter. 3.

The film morphology changes totally when the film thickness is sufficiently large. This is shown earlier in Chap 5, and is demonstrated again in the second case where the initial surface profile is identical to that of the first case but the film thickness is increased to 30 nm. Plotted in Figs. 6.1(b1), 6.1(b2), and 6.1(b3), the results indicate that the surface undulation process mainly result in faceted pits and trenches first, instead of islands or ridges. The pits and trenches subsequently facilitates the growth of pyramids and ridges at the adjacent sites, leading to a ripple structure. Using the same film as in the second case, the third case examines how the CRT formation is affected by the presence of shallow holes on the initial surface (Gray et al. 2004c). The holes are randomly distributed; the diameter and depth of the holes are varied ±10% around the prescribed average values, which are 50 and 0.9 nm, respectively. The same random roughness as employed in the earlier cases is still included on the initial surface profile. The results, illustrated in Figs. 6.1(c1), 6.1(c2), and 6.1(c3), show that the CRT formation causes the holes to develop into QDMs of comparable shapes. The QDMs consist of a faceted pit, a ridge ring, and a trench ring, which are consistent with the structures reported in the literature (Gray et al. 2002; 2004c). The regular QDMs morphology is in contrast to the random distribution of trenches and ridges in the second case. The difference demonstrates the important role of shallow holes in the QDMs formation.

In summary, Fig. 6.1 shows that the CRT formation happens on thick films; the process leads to QDMs if shallow holes are present on the initial surface and to a network of irregular ripples if the initial surface is characterized by random roughness.

The suppression of the cooperative formation on thin films can be understood as follows. Both islands and trenches/pits can reduce the strain energy stored in the film, and the latter is more effective than the former (Chiu and Gao 1993). Though reducing

Table 6.1: The film thickness and the initial surface profiles of the three cases shown in Fig. 6.1.

Case	Film Thickness (nm)	Initial Profile
1	4	random roughness
2	30	random roughness
3	30	holes and random roughness

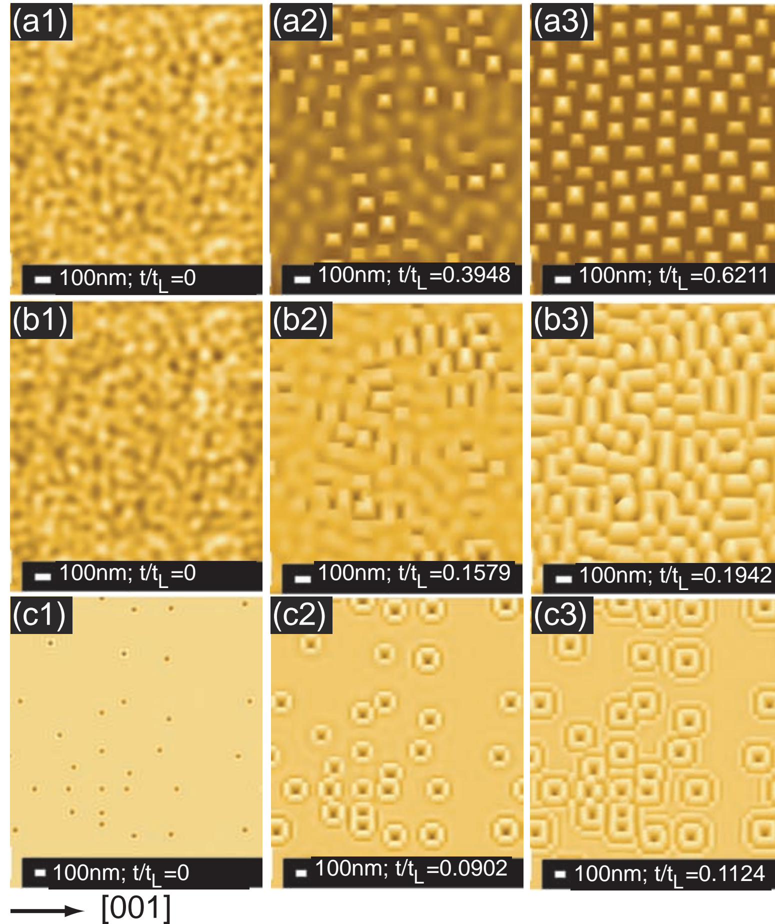

Figure 6.1: The morphological evolution of $Si_{0.7}Ge_{0.3}/Si$ with different film thickness and initial surface profiles. 6.1(a1), 6.1(a2), and 6.1(a3): $H_f = 4$ nm and the initial film surface is flat with rms roughness being 0.05 nm. 6.1(b1), 6.1(b2), and 6.1(b3): $H_f = 30$ nm and the initial profile is the same as the first case. 6.1(c1), 6.1(c2), and 6.1(c3): $H_f = 30$ nm and an array of shallow holes are present at $t = 0$. The average diameter and depth of the holes are 50 and 0.9 nm, respectively. The tone of the colors represents the angle ϕ between the normal vector of the surface and the vertical direction. The lightest one corresponds to $\phi = 0°$; the darkest ones to 0.14° in 6.1(a1) and 6.1(b1), 6.9° in 6.1(c1), 11.3° in 6.1(a2), 6.1(b2), 6.1(c2), and 6.1(a3), and 15° in 6.1(b3) and 6.1(c3).

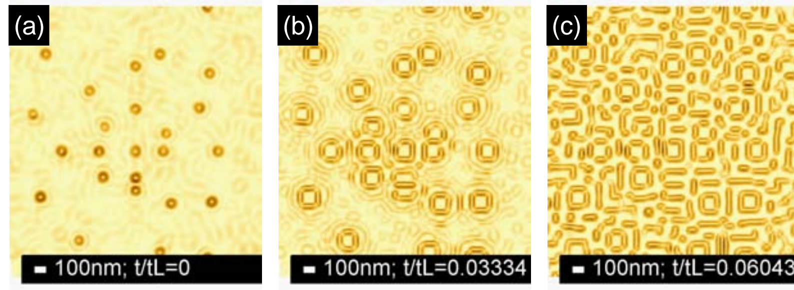

Figure 6.2: The morphological evolution of $Si_{0.7}Ge_{0.3}/Si$ at thin film with shallow holes. $H_f =$ 1.5 nm and the initial film surface is flat with rms roughness being 0.05 nm.

more strain energy, the formation of trenches/pits is obstructed on thin films because of the film-substrate interaction energy. The interaction energy favors nanostructures protruding out of the films over those penetrating into the films. Since the strength of the interaction energy increases with decreasing film thickness, the trench/pit growth and thus the CRT formation are impeded when H_f is small.

The significance of the interaction energy on suppressing the trench/pit formation is further investigated by employing a lower interaction energy density ($\hat{g}_0 = 0.01$) to simulate case 1 of Table 6.1. As plotted in Figs. 6.2(a)-6.2(c), the results confirmed that faceted trenches and pits formed if the interaction energy density is sufficiently low. The trenches and pits, however, exhibited flat bases at the bottom of the nanostructures instead of an apex or a sharp edge. The pit/trench shapes are different in this case because the depth of fully developed pits and trenches are larger than the thickness of the film above the wetting layer. Due to the small film thickness, when the growth of the pits and trenches approached the wetting layer, the growth is hindered by the wetting layer, leading to the formation of the flat bases.

6.3 Kinetic pathways

Motivated by the findings in Figs. 6.1(c1), 6.1(c2), and 6.1(c3), our investigation turns to the case of a single shallow hole on a thick $Si_{0.7}Ge_{0.3}$ film to reveal the kinetic pathways of the CRT formation. The diameter and depth of the hole are 50 and 0.9 nm, respectively.

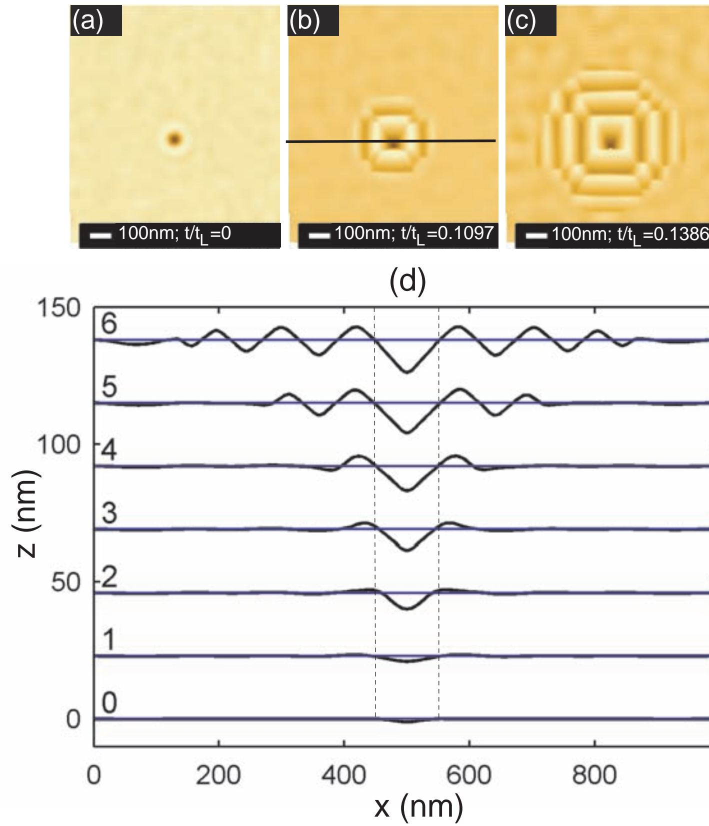

Figure 6.3: (a)–(c) The morphological evolution of a hole with 50 nm in diameter and 2 nm in depth on a film with $H_f = 30$ nm. (d) The film cross-sections along the solid lines shown in (b) during the evolution. In (d) the horizontal line represents the initial height of the film, and the dashed lines indicate the final pit size.

In addition to the hole, the random roughness is also present on the initial surface. The morphological evolution of the hole is depicted in Figs. 6.3(a) - 6.3(c). The results suggest, via the cooperative formation, the shallow hole first evolves into a QDM and then a relatively ordered ripple structure involving multiple rings of ridges and trenches.

The formation process is further studied in Fig. 6.3(d) by plotting the film cross-sections at different time steps along the solid line shown in Fig. 6.3(b). The figure reveals that the shallow hole first transforms into a faceted pit and then the pit enlarged (see lines 0–2). The pit growth is significantly impeded when ridges develops at the pit edges. The ridges are faceted on the side facing the pit initially (see line 3). Afterward, the ridges are fully faceted and grew continuously (see line 4). Similar to the pit, the ridge growth is also hindered after the ridges activated the formation of faceted trenches surrounding the ridges (see line 5). The subsequent morphological evolution on the film

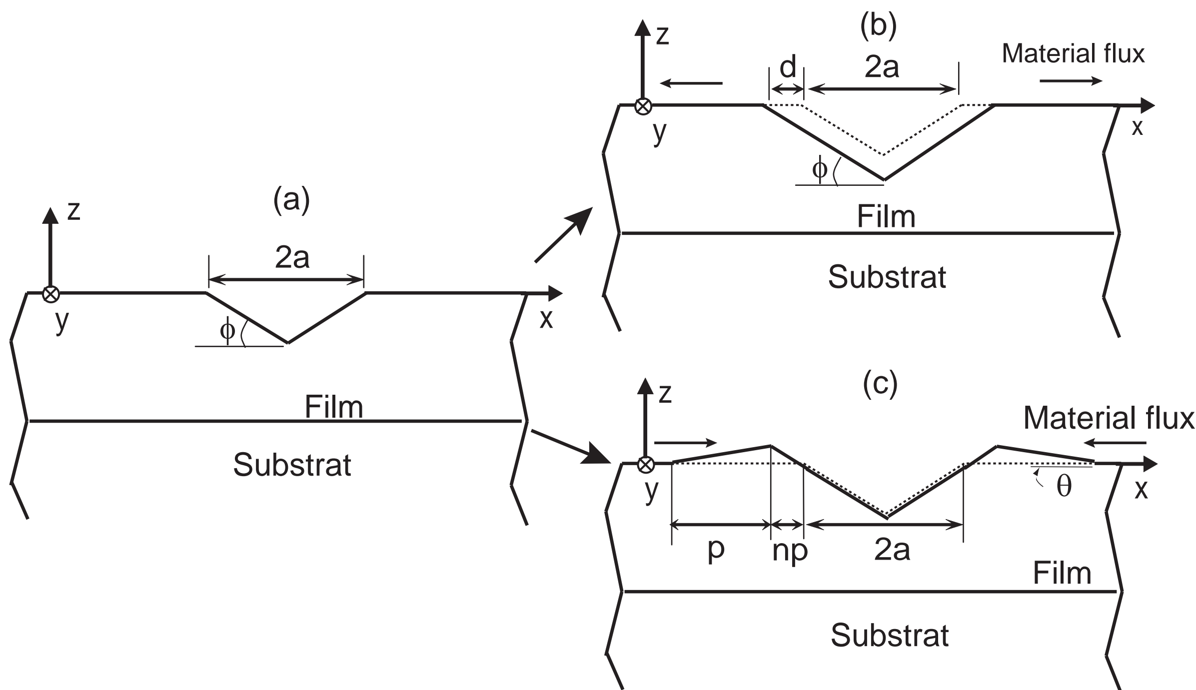

Figure 6.4: Schematic diagrams of the two competing pathways of the CRT formation: (a) the initial condition, (b) the self-similar pit growth, and (c) the adjacent ridge formation. The dotted lines in (b) and (c) indicate the initial profile illustrated in (a).

follows the same pattern, leading to the cooperative formation (see line 6).

In short, Fig. 6.3(d) shows that the cooperative formation results from the competition of two kinetic pathways: the growth of the existing outermost nanostructure and the formation of a new structure adjacent to the outermost one.

6.4 Energy Analysis for the Cooperative Formation

In this section, the two competing pathways of the CRT formation are analyzed from the energy point of view with the focus on the initial stage of the formation process, where the shallow hole has transformed into a faceted pit. The results provide an insight into the alternative growth of ridges and trenches and the size selection mechanism of the CRT formation.

6.4.1 A model problem

Figure 6.3 plots the 2D model adopted in the energy analysis for the CRT formation on the surface of a heteroepitaxial film-substrate system. The film thickness is sufficiently large so that the film-substrate interaction energy in the system can be neglected, and it is the strain energy and surface energy that dictate the morphological evolution of the nanostructures on the film surface.

The film-substrate system contains a faceted pit initially, as illustrated in Fig. 6.3(a). The pit may evolve via two pathways. In the first pathway, depicted in Fig. 6.3(b), the film material is transported from the pit surfaces to the remaining flat film profile, causing the pit to grow self-similarly. The volume ΔV (per unit length in the y direction) of the transported material can be calculated to be

$$\Delta V = \mathcal{S}(2a + d)d, \tag{6.1}$$

where $2a$ is the width of the initial facet and $2d$ is the increment of the pit width. According to Eq. (6.1), d can be expressed as a function of the volume ΔV,

$$d = \sqrt{a^2 + \frac{\Delta V}{\mathcal{S}}} - a. \tag{6.2}$$

In contrast to the first pathway, the film material in the second pathway is transported from the flat film surface to the edges of the pit, leading to the formation of a ridge at both edges of the pit, see Fig. 6.4(c). The surface of the ridge facing the pit is the same facet as the pit one, while the other surface of the ridge is nonfacet. The angle between the nonfacet surface and the flat film profile is θ and is allowed to vary during the formation process. The nonfacet surface with adjustable θ is adopted here as a simple model to account for the gradual ridge formation.

The surface energy density $\gamma(\theta)$ of the film surface is taken to be

$$\gamma(\theta) = \gamma_0 - \Delta\gamma \exp\left[-\beta|\theta - \phi|\right], \tag{6.3}$$

which contains a cusp at the facet angle $\theta = \phi$. In Eq. (6.3), $\Delta\gamma$ is the depth of the cusp, and $\beta\Delta\gamma$ is the gradient $d\gamma/d\theta$ at the cusp. The quantity β is assumed to be large; thus, γ approximates to γ_0 in the vicinity of $\theta = 0$.

The volume ΔV of the material that is transported from the flat film surface to form the ridges can be expressed as

$$\Delta V = \mathcal{S}n(1+n)p^2, \tag{6.4}$$

where p, as illustrated in Fig. 6.4(c), is the length of the projection of the ridge nonfacet surface onto the flat film and n is defined to be $n = \tan\theta/\tan\phi \approx \theta/\phi$.

The energy changes of the two pathways, namely, the self-similar pit growth and the adjacent ridge formation, are compared in the next section.

6.4.2 Energy changes

Self-similar pit growth

The energy change ΔE_{tot1} due to the self-similar pit growth can be estimated by using the method discussed in Sec. 3.1. We first consider the pit illustrated in Fig. 6.4(a) where the center of the pit is located at $x = 0$ and the width of the pit is $2a$. Based on the information and Eq. (3.10), the function $\Psi_0(x)$ for the pit can be found to be

$$\Psi_0(x) = -\frac{2}{\pi}\ln\left(\frac{x^2 - a^2}{x^2}\right). \tag{6.5}$$

Substituting the function into Eqs. (3.11) and (3.12) yields the strain energy change $W_{\sigma 0}$ due to the formation of the pit,

$$W_{\sigma 0} = -\frac{8\ln 2}{\pi}w_0\mathcal{S}V_0, \tag{6.6}$$

where $V_0 = \mathcal{S}a^2$ is the pit volume. Equation (6.6) suggests when the pit volume increases from V_0 to $V_0 + \Delta V$ during the self-similar growth as shown in Fig. 6.4(b), the total strain

energy changes by

$$\Delta W_{\sigma 1} = -\frac{8 \ln 2}{\pi} w_0 \mathcal{S} \Delta V. \tag{6.7}$$

Adding the strain energy change and the corresponding surface energy change, given by $2\gamma_0 G_\phi d$, leads to the total energy change ΔE_{tot1} of the self-similar growth,

$$\Delta E_{tot1} = -\frac{8 \ln 2}{\pi} w_{\sigma 0} \mathcal{S} \Delta V + 2\gamma_0 G_\phi d, \tag{6.8}$$

where $G_\phi = -1 + \gamma_1/\gamma_0 \cos\phi$, $\gamma_1 = \gamma_0 - \Delta\gamma$ is the surface energy density of the facet, and d is related to ΔV by Eq. (6.2).

Adjacent ridge formation

Turn to the adjacent ridge formation illustrated in Fig. 6.4(c). There are two adjacent ridges in this problem, differing from that considered in Sec. 3.1.3. In spite of the difference, the strain energy change of the current case can still be calculated by Eqs. (3.11) and (3.12) presented in Sec. 3.1.

The calculation begins with writing down the two functions $f^-(x)$ and $f^+(x)$ that describe the shapes of the adjacent ridges at the left and right edges of the pit, respectively,

$$f^-(x) = \begin{cases} n\mathcal{S}_\alpha(x+c) & \text{for } -c < x < -b \\ -\mathcal{S}_\alpha(x+a) & \text{for } -b < x < -a \end{cases} \tag{6.9}$$

$$f^+(x) = \begin{cases} \mathcal{S}_\alpha(x-a) & \text{for } a < x < b \\ -n\mathcal{S}_\alpha(x-c) & \text{for } b < x < c \end{cases}, \tag{6.10}$$

where $b = a + np$, $c = a + (n+1)p$, and $n = \tan\theta/\mathcal{S}_\alpha$. Based on the information provided in Eqs. (6.9) and (6.10), $\Psi_\alpha(x)$ of the two adjacent ridges can be expressed as

$$\Psi_\alpha(x) = -\frac{2}{\pi}\left(\ln\frac{x^2-b^2}{x^2-a^2} + n\ln\frac{x^2-b^2}{x-c^2}\right). \tag{6.11}$$

In comparison, $\Psi_0(x)$ of the pit is given in Eq. (6.5). Substituting the expressions for $\Psi_0(x)$ and $\Psi_\alpha(x)$ into Eqs. (3.11) and (3.12) and noticing that $\mathcal{S}_0$ and $\mathcal{S}_\alpha$ appearing in those two equations are equal to $\mathcal{S}$ for the current case yield the strain energy change $\Delta W_{\sigma 2}$ due to the adjacent ridge formation,

$$\Delta W_{\sigma 2} = -w_0 \mathcal{S} \Delta V\, U_2, \tag{6.12}$$

where $\Delta V\, U_2$ is given by

$$\Delta V\, U_2 \;=\; \int_{-c}^{-a} \left[2\Psi_0(x) + \Psi_\alpha(x)\right] f^-(x)dx + \int_a^c \left[2\Psi_0(x) + \Psi_\alpha(x)\right] f^+(x)dx. \tag{6.13}$$

Summing $\Delta W_{\sigma 2}$ and the corresponding surface energy changes yields the total energy change ΔE_{tot2} of the adjacent ridge formation expressed in Eq. (6.14),

$$\Delta E_{tot2} = -w_{\sigma 0} \mathcal{S} \Delta V U_2 + 2\gamma_0 (nG_\phi + G_\theta)p, \tag{6.14}$$

where the quantity $\Delta V U_2$ is defined in Eq. (6.13) and $G_\theta = -1 + \gamma(\theta)/(\gamma_0 \cos\theta)$.

The energy difference $\Delta E_{tot} = \Delta E_{tot2} - \Delta E_{tot1}$ between the ridge formation and the pit growth is illustrated in Fig. 6.5 by plotting the contours of ΔE_{tot} as a function of ΔV and θ. The contours with $\Delta E_{tot} < 0$ determine the domain $(\Delta V, \theta)$ in which the adjacent ridge formation is more energetically favorable, while those with $\Delta E_{tot} > 0$ define the domain where the pit growth is preferred. The figure considers two cases that differ in the initial pit size: $2a = 90$ and 190 nm in Figs. 6.5(a) and 6.5(b), respectively. Except a, the other parameters adopted in the two cases are identical: $L = \gamma_0/w_0 = 70$ nm, $\gamma_0 = 1$ J/m, $\Delta\gamma/\gamma_0 = 0.015$, $\beta = 50$, and $\phi = 11.3°$.

A distinctive feature in both Figs. 6.5(a) and 6.5(b) is the sharp variation of the contours in the narrow stripe located at $\theta = \phi$. The narrow stripe is called the facet domain in this thesis since the stripe corresponds to the case, where the adjacent ridge is fully faceted. The remaining area, characterized by smooth contours, gives ΔE_{tot} for the case, where the ridge contains a nonfacet surface; this area is termed the nonfacet

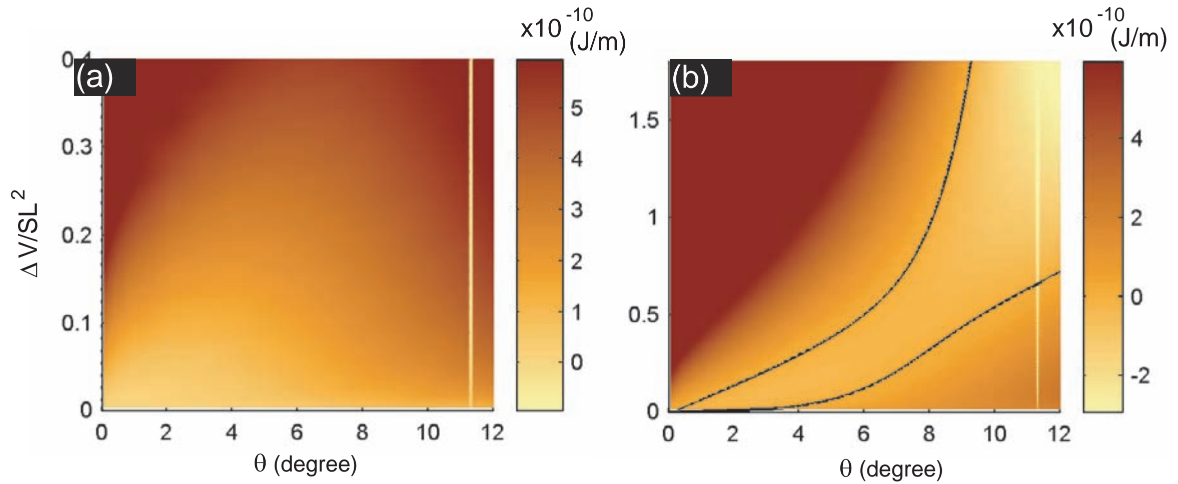

Figure 6.5: The contour of the energy difference ΔE_{tot} as a function of ΔV and θ for the cases, where $L = 70$ nm, $\gamma_0 = 1$ J/m, $\Delta\gamma_0/\gamma_0 = 0.015$, $\phi = 11.3°$, and $\beta = 50$; $2a = 90$ nm in (a) and $2a = 190$ nm in (b).

domain. The two domains represent different ways of adjacent ridge formation. The facet domain refers to an abrupt shape transformation, which can occur by nucleation. The nonfacet domain, in contrast, implies a gradual shape change that happens during the surface undulation process. The nonfacet domain is investigated in the following.

The nonfacet domain depicted in Fig. 6.5(a) shows a typical result of ΔE_{tot} for the case of small pit size. The result is characterized by the pattern that ΔE_{tot} is positive and increases with ΔV. The characteristics suggests that the energy favors the pit growth over the adjacent ridge formation during the surface undulation process when the pit size is small. The nonfacet domain plotted in Fig. 6.5(b), in contrast, represents the result of large pit size. The domain is divided into two regimes along the two black lines that depict the contours $\Delta E_{tot} = 0$. The regime outside the two black lines indicates positive ΔE_{tot} and is favored by the pit growth. The regime between the black lines, on the contrary, shows $\Delta E_{tot} < 0$ and is dictated by the adjacent ridge formation. The result suggests that the adjacent ridge formation can be more favorable than the pit growth during the surface undulation process when the pit size is sufficiently large.

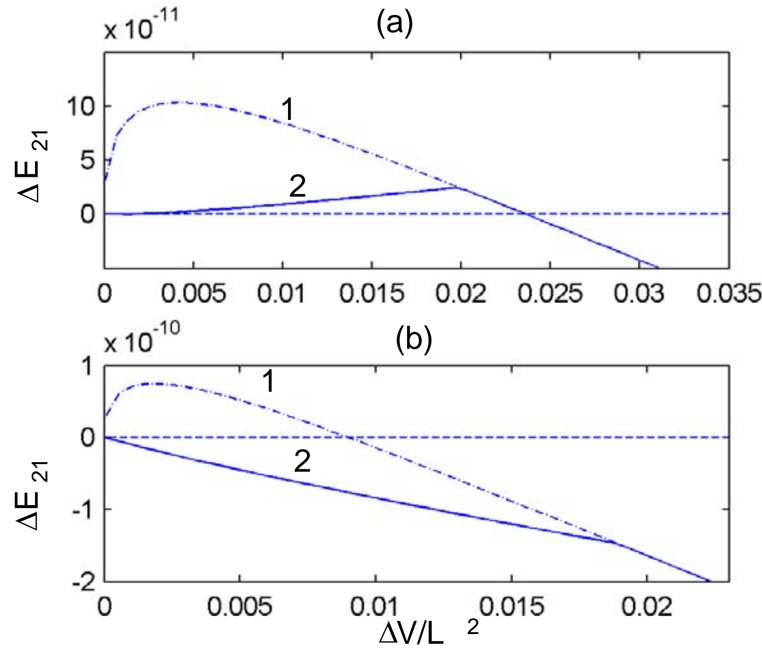

Figure 6.6: The effects of ΔV on ΔE_{eq} and ΔE_{tot} of faceted ridges for the two cases shown in Fig. 6.5. The function ΔE_{eq} is depicted by the solid lines and ΔE_{tot} of faceted ridges by the dash-dotted lines.

6.4.3 The gradient $\mathcal{F}$

The effect of the initial pit size on the adjacent ridge formation can be further understood by considering the function $\Delta E_{eq}(\Delta V)$, defined as the minimum of $\Delta E_{tot}(\Delta V, \theta)$ among all θ for a given value of ΔV. The function $\Delta E_{eq}(\Delta V)$ is plotted by the solid lines in Figs. 6.6(a) and 6.6(b) for the two cases shown in Fig. 6.5. The two lines suggest whether the adjacent ridge formation can happen or not during the surface undulation process is determined by the gradient $\mathcal{F}$ of the function $\Delta E_{eq}(\Delta V)$ at $\Delta V = 0$,

$$\mathcal{F} = \left. \frac{d\Delta E_{eq}}{d\Delta V} \right|_{\Delta V=0} . \tag{6.15}$$

A positive value of $\mathcal{F}$ signifies that the adjacent ridge formation encounters an energy barrier, see Fig. 6.6(a). On the contrary, $\mathcal{F}$ is negative if the formation process is barrierless, see Fig. 6.6(b).

6.4.4 Derivation of $\mathcal{F}$

The crucial quantity $\mathcal{F}$ is derived in this section. The result is then employed in the next section to determine the critical pit size for the adjacent ridge formation.

The key step in deriving $\mathcal{F}$ is to calculate ΔE_{tot1} and ΔE_{tot2} under the condition $\Delta V/\mathcal{S}a^2 \ll 1$. For ΔE_{tot1}, the condition means d given in Eq. (6.2) can be expressed as $d = \Delta V/(2\mathcal{S}a)$. Applying the result to Eq. (6.8) yields

$$\Delta E_{tot1} = w_0 \Delta V \left(-\frac{8\mathcal{S}\ln 2}{\pi} + \frac{LG_\phi}{\mathcal{S}a} \right). \tag{6.16}$$

For ΔE_{tot2}, the condition of small ΔV implies θ and n are small. Accordingly, $\gamma(\theta) \approx \gamma_0$, $G_\theta \ll G_\phi$, and $p = \sqrt{\Delta V/\mathcal{S}n}$. Substituting these expressions into Eq. (6.14), noticing that the term $\Delta V\, U_2$ can be simplified by the scheme presented in Sec. 3.2.3, and ignoring the terms with higher order of n reduce ΔE_{tot2} to

$$\Delta E_{tot2} = -\frac{w_0 \mathcal{S} \Delta V}{\pi} \left[6 - 4\ln 2 + 2\ln\left(\frac{\mathcal{S}na^2}{\Delta V} \right) \right] + 2\gamma_0 G_\phi \sqrt{\frac{n\Delta V}{\mathcal{S}}}. \tag{6.17}$$

The condition $\partial \Delta E_{tot2}/\partial n = 0$ yields the equilibrium relative slope n_{eq} that minimizes ΔE_{tot2} at $\Delta V/\mathcal{S}a^2 \ll 1$,

$$n_{eq} = \frac{4\mathcal{S}^3 \Delta V}{\pi^2 G_\phi^2 L^2}. \tag{6.18}$$

Substituting Eq. (6.18) into (6.17) and subtracting ΔE_{tot1} from the result determine the minimum ΔE_{eq} at small ΔV,

$$\begin{aligned} \Delta E_{eq} &= \Delta E_{tot2}|_{n=n_{eq}} - \Delta E_{tot1} \\ &= \frac{w_0 \mathcal{S} \Delta V}{\pi} \left[-2 - \frac{\pi G_\phi L}{a\mathcal{S}^2} + 4\ln\left(\frac{4\pi G_\phi L}{a\mathcal{S}^2} \right) \right]. \end{aligned} \tag{6.19}$$

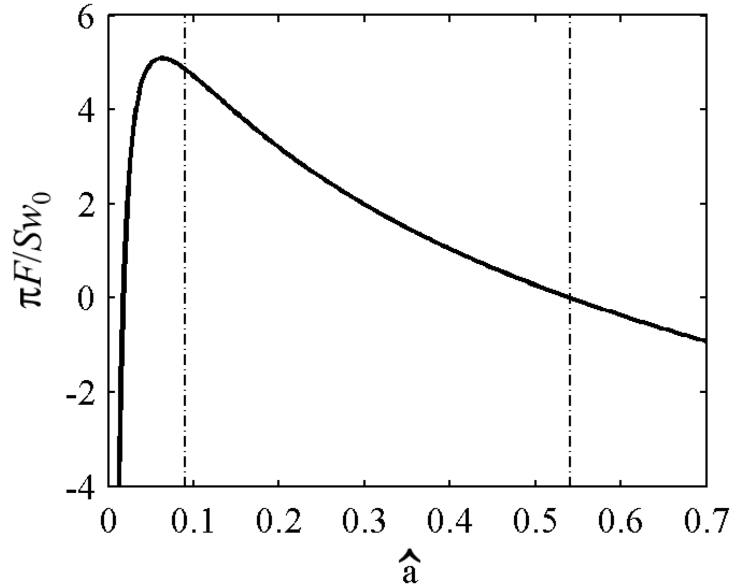

Figure 6.7: The variation of $\pi\mathcal{F}/w_0\mathcal{S}$ with the normalized pit size $\hat{a}$.

Differentiating Eq. (6.19) with respect to ΔV gives $\mathcal{F}$,

$$\mathcal{F} = \frac{w_0\mathcal{S}}{\pi}\left(-2 - \frac{1}{4\hat{a}} - 4\ln\hat{a}\right), \tag{6.20}$$

where $\hat{a}$ is the normalized pit size,

$$\hat{a} = \frac{a\mathcal{S}^2}{4\pi G_\phi L}. \tag{6.21}$$

6.4.5 Critical pit size for adjacent ridge formation

Figure 6.7 plots the variation of $\pi\mathcal{F}/w_0\mathcal{S}$ with the normalized pit size $\hat{a}$. The result is divided into three ranges of $\hat{a}$: $[0, \hat{a}_{cr,0}]$, $[\hat{a}_{cr,0}, \hat{a}_{cr}]$, and $[\hat{a}_{cr}, \infty]$ where $\hat{a}_{cr,0}$ corresponds to the critical pit size above which the formation of the faceted pit reduces the total energy of the system,

$$\hat{a}_{cr,0} = \frac{1}{16\ln 2}, \tag{6.22}$$

and the quantity $\hat{a}_{cr} = 0.5403$ is the larger solution of the two results that satisfy the equation $\mathcal{F} = 0$.

The first range, $[0, \hat{a}_{cr,0}]$, is characterized by a drastic variation of $\mathcal{F}$. The range, however, is disregarded since the initial pit is too small to be an energetically favorable nanostructure in the first place. The second range, $[\hat{a}_{cr,0}, \hat{a}_{cr}]$, is characterized by positive $\mathcal{F}$. The characteristics suggests that in the second range the pit formation is energetically favorable and the pit growth suppresses the development of adjacent ridges. The third range $[\hat{a}_{cr}, \infty]$, in contrast, shows negative $\mathcal{F}$. This confirms the finding implied in Figs. 6.5 and 6.6 that the adjacent ridge formation by a gradual shape change can reduce more energy than self-similar pit growth once the pit size exceeds a critical value. By substituting $\hat{a}_{cr} = 0.5403$ into Eq. (6.21), the critical pit size a_{cr} for the adjacent ridge formation can be expressed as

$$a_{cr} = \frac{\eta G_\phi L}{\mathcal{S}^2}, \tag{6.23}$$

where $\eta = 4\pi\hat{a}_{cr}$. The critical value a_{cr} gives a good estimate for the pit size appearing in the cooperative formation. For example, $2a_{cr} = 106$ nm for the parameters adopted in Figs. 6.5 and 6.6, which is consistent with the value reported in literature (Gray et al. 2002).

6.4.6 Fully faceted adjacent ridge

The adjacent ridge formation is barrierless when the ridge is allowed to change its shape during the formation process. The scenario is completely different if the adjacent ridge is fixed to be a fully faceted structure, i.e., $\theta = \phi$. The energy difference ΔE_{tot} of this scenario is illustrated by the facet domain in Figs. 6.5(a) and 6.5(b) and is redrawn by the dash-dotted lines in Figs. 6.6(a) and 6.6(b), respectively. The two dash-dotted lines follow the same trend: ΔE_{tot} increases with ΔV first, reaches a maximum, and then declines to negative values. The result demonstrates that the direct formation of a faceted structure

at the adjacent site always needs to overcome an energy barrier and a critical nucleation size before the process can reduce more energy than the pit growth.

The dash-dotted lines coincide with the solid lines in Fig. 6.6 after ΔV exceeds a critical value. The result shows that though the fully faceted structure is less favorable than a partially faceted one in the early stage of the adjacent ridge formation, the fully faceted one eventually becomes the most favorable morphology. The transition to the fully faceted ridge is expected to be similar to that of a single nanoisland changing from a shallow bump to a faceted pyramid (Chiu and Huang 2006; 2007; Tersoff et al. 2002).

6.5 Discussion

This section first presents an overview of the CRT formation based on the results shown in Secs. 6.2 and 6.3. This is followed by a brief discussion on how the CRT formation may be affected by the deposition process in Sec. 6.5.2 and a survey of the limitations of the model employed in this study in Sec. 6.5.3.

6.5.1 The CRT formation

The results in Secs. 6.2 and 6.3 reveal that the cooperative formation is an interplay between the growth of the outermost nanostructure and the formation of a new structure adjacent to the outermost one via the surface undulation process. The cooperative formation starts with the development of faceted nanostructures on a thick film by surface undulation, a barrierless process similar to that on a thin film (Chiu and Huang 2006; 2007; Tersoff et al. 2002). The faceted nanostructures are mainly pits and trenches.

After the faceted structure forms, the structure grows until reaching a critical size. In this stage, the growth reduces energy, and it reduces more energy than the gradual formation of adjacent structures. Above the critical size, however, the adjacent structure formation becomes more effective in reducing the energy than the growth of the first structure. As a consequence, the growth of the first structure is suppressed and the adjacent structure emerges.

The development of the new structure is characterized by a sequence similar to that of the first structure: (1) formation of a small ridge with nonfacet surface, (2) shape transition to a fully faceted structure, (3) further enlargement of the structure, and (4) suppression of growth due to the formation of another adjacent structure. The repeating emergence of the adjacent structures and their self-limiting growth is the mechanism of the CRT formation.

The resulting morphology of the cooperative formation is a ripple structure consisting of nanotrenches and nanoridges. The shapes of those nanostructures are irregular if the initial surface profile is dictated by random roughness (Ozkan et al. 1997; 1999). The nanostructures, however, can self-organize into an ordered configuration to form QDMs if the initial surface contains shallow holes (Gray et al. 2002) .

6.5.2 Deposition

Before exploring the effects of the deposition process on the CRT formation, it is helpful to discuss first how the deposition process influences the morphological evolution of the film surface from three aspects. First, the deposition introduces statistical roughening on the film surface, and this can play a crucial role in the development of shallow holes (Lam et al. 2002). Second, the deposition increases the film thickness, which in turn influences the types of nanostructures emerging from the film surface. Third, the effects of the deposition process are controlled by the ratio between the deposition and the surface diffusion rates. The ratio can be increased by raising the deposition rate and/or reducing the substrate temperature.

Back to the effects of the deposition process on the CRT formation. Of particular interest here are the three general cases, where the ratio between the deposition and the surface diffusion rates is large, moderate, and small, respectively. For the case, where the ratio is large, the film can quickly become a thick one before an island array can develop. Furthermore, when the ratio is large, there is a high probability for the statistical roughening to form holes deeper than the average roughness of the film surface during the

deposition process. The thick film and the holes suggest that the CRT formation happens in this case and is characterized by the development of ordered QDMs.

For the case of a moderate ratio, it is conjectured that the ratio is high enough to induce the CRT formation but insufficient to cause the statistical roughening to generate holes on the film surface. As a consequence, the film morphology is a ripple structures composed of irregular nanoridges and nanotrenches in the second case.

For the case of a small ratio, the film thickness can remain low for a long period of time to promote the development of islands on a thin wetting layer. After the development, the islands will grow in size since the material deposited onto the film surface can be transported to the islands quickly by surface diffusion. The process continues until the islands coalesce. The development and growth of the islands suppress the CRT formation in this case.

The qualitative descriptions of the three cases are consistent with the findings reported in the literature (Gray et al. 2005). In particular, the first case of a large ratio agrees with the observations at a low deposition rate and a high temperature. The second case of a moderate ratio corresponds to the experimental results at the same deposition rate but a lower temperature. The third case of a low ratio captures the phenomenon at fast deposition and a low temperature.

6.5.3 Limitations

The surface diffusion model adopted here captures well the formation of QDMs during the fast deposition process (Gray et al. 2002; 2005) and the development of the ripple structure during the high-temperature annealing (Ozkan et al. 1997; 1999). The model, however, cannot explain the finding that shallow holes evolve into long trenches when annealed at low temperatures. The difference suggests the simple model described by Eqs. (2.6) and (2.7) is suitable for the surface diffusion mechanism in the deposition and in the high-temperature annealing, while the model needs to be modified in order to simulate trench growth during annealing at low temperatures.

Besides the deposition process and the elongated trenches, other issues that need to be considered include the composition variation in the film (Spencer et al. 2001; Tu and Tersoff 2007), the surface stress (Shchukin et al. 1995), the orientation of the substrate, and the different stiffness between the film and the substrate (Spencer et al. 1991). Understanding these issues is essential for building a complete picture of the cooperative formation.

Chapter 7

The SK System under Electric Field

This chapter investigates the stability of wires against the size variation for Stranski-Krastanow systems under the influence of an electric field generated by a patterned electric plate. The stability is determined by considering the total energy change as a function of the wire size. The results show that the wire size can be stabilized by the electric field if the systems meet the viability criterion and the effective electric field effect is within the maximum and minimum limits.

7.1 Introduction

Recently, we proposed that electric fields generated by patterned electrodes could also be an effective prescription for controlling the self-assembly of nanoislands in the SK systems; the idea is termed the electromolding self-organization (EMSO) process (Chiu et al. 2006). Our numerical simulation for the EMSO process suggests that the process is capable of fabricating a wide range of island shapes, including 2×2 island arrays, square rings, cross junctions, and zigzag ridges, with controllable sizes and locations. The EMSO process also has the crucial advantage that the process can produce nanostructures stable against size variation (Chiu et al. 2006). The unique feature is in contrast to the common problem of unstable islands in the SK systems and in the LISA method (Chou et al. 1999; Schäffer et al. 2000).

The size stability is examined in this chapter by analyzing the total energy changes due to the formation of faceted nanostructures. Our investigation focuses on the two-dimensional cases, and of particular interest is the scenario where the height of the electric plate is much larger than the wire size. The results reveal that the size stability can be achieved in the EMSO process if the material properties and the film thickness of the SK system satisfy the viability criterion and the effective electric field effect is within the upper and lower limits. The results illuminate a clear overall picture for understanding how the size stability is affected by the vast amount of parameters involved in the EMSO process, including the material properties of the SK system, the film thickness, the electric plate height, and the size and slope of the pattern on the electric plate.

This chapter is organized as follows. Section 7.2 summarizes the methods for calculating the total energy change due to the formation of a faceted wire under an electric field. Section 7.3 examines the size stability of the SK systems without the electric field. Section 7.4 adopts a coarsening SK system to investigate the effects of the electric field on the size stability. Section 7.5 derives the stability condition for the case where the electric plate height is large. Section 7.6 presents the numerical simulation results. Section 7.7 discusses how to modify the SK system to produce stable nanostructures, the kinetic aspects and limitations. The chapter is concluded in Sec. 7.8 with a summary of the results.

7.2 Model and Energy Analysis

Section 7.2.1 first presents the model system for analyzing the size stability. The energy change ΔE_{tot} of the system is then determined in Sec. 7.2.2 by adopting the formulae discussed in Sec. 7.2.1. The result is further simplified in Sec. 7.2.3 for the case where the electric plate height is much larger than the wire base width.

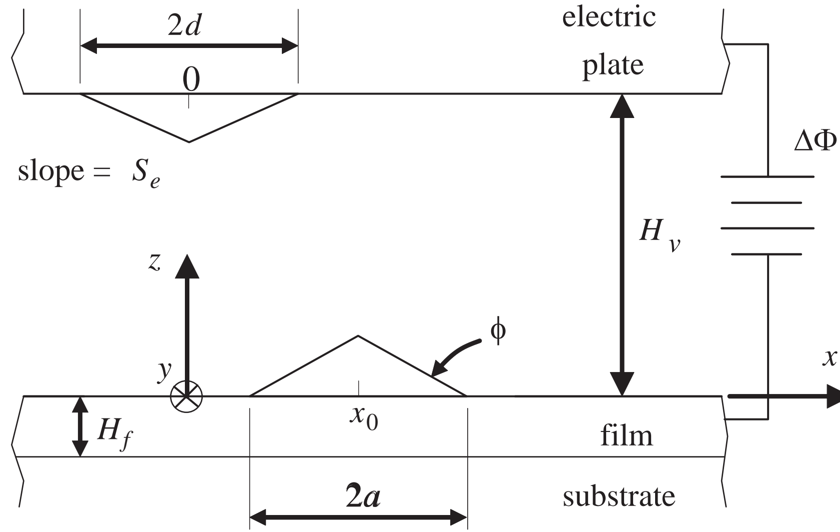

Figure 7.1: Schematic diagram of a triangular wire on an SK system under the influence of a triangular pattern on an electric plate with a misalignment of x_0 between the centers of the two structures.

7.2.1 Model system

Figure 7.1 plots the model adopted in this chapter where a triangular wire on an SK film-substrate system is exposed to an electric plate containing a triangular pattern. The wire is characterized by the slope $\mathcal{S} = \tan\phi$ and the base width $2a$; in comparison, the slope and width of the pattern are $\mathcal{S}_e$ and $2d$, respectively. In addition to the differences in slope and width, the wire and the pattern are also misaligned by x_0. For convenience, the center of the pattern base is taken to be at $(0, H_v)$, and that of the wire at $(x_0, 0)$.

7.2.2 Energy analysis

For the triangular wire and pattern considered in the model, the three functions, Ψ_σ, Ψ_1, and Ψ_2, for evaluating the changes of the strain and electrostatic energy can be written down directly by referring to Eqs. (3.50), and (3.52),

$$\Psi_\sigma = \frac{2}{\pi}\Re\left[\ln\frac{(x-b_1)(x-b_3)}{(x-x_0)^2}\right], \tag{7.1}$$

$$\Psi_1 = \frac{1}{\pi}\Re\left\{\ln\left[e^{\eta(x-b_1)}-1\right]+\ln\left[e^{\eta(x-b_3)}-1\right]-2\ln\left[e^{\eta(x-x_0)}-1\right]\right\}, \tag{7.2}$$

$$\Psi_2 = \frac{1}{\pi}\Re\left\{\ln\left[e^{\eta(x+d)}+1\right]+\ln\left[e^{\eta(x-d)}+1\right]-2\ln\left[e^{\eta x}+1\right]\right\}, \tag{7.3}$$

where $b_1 = x_0 - a$ and $b_3 = x_0 + a$. Substituting Eq. (7.1) into (3.67) leads to $U_\sigma = (8 \ln 2)/\pi$; for conciseness, this value is denoted as U_0, i.e.,

$$U_0 = \frac{8}{\pi} \ln 2. \tag{7.4}$$

Similarly, substituting Ψ_1 and Ψ_2 given in Eqs. (7.2) and (7.3) into (3.67) yields U_1 and U_2. The quantity U_1 depends on ηa, and U_2 is a function of ηx_0, ηa, and ηd. For moderate values of ηx_0 and ηa, the two quantities U_1 and U_2 have to be evaluated numerically. For the special case where $\eta x_0 \ll 1$ and $\eta a \ll 1$, on the other hand, U_1 and U_2 can be expressed as,

$$U_1 = \frac{U_0}{2} + \frac{\eta^2 a^2}{12\pi}, \tag{7.5}$$

$$U_2 = \frac{\mathcal{K}_0}{2} - \frac{\mathcal{K}_2 \eta^2 a^2}{12} - \frac{\mathcal{K}_2 \eta^2 x_0^2}{2}, \tag{7.6}$$

where the two constants $\mathcal{K}_0$ and $\mathcal{K}_2$ are given by

$$\begin{aligned} \mathcal{K}_0 &= \frac{4}{\pi} \ln \cosh \frac{\pi \hat{d}}{2}, \\ \mathcal{K}_2 &= \frac{1}{2\pi} \left(1 - \cosh^{-2} \frac{\pi \hat{d}}{2} \right), \end{aligned} \tag{7.7}$$

and $\hat{d} = d/H_v$ is the normalized pattern size.

The quantity U_1 described in Eq. (7.5) refers to the effect of the wire shape on the electrostatic energy change ΔW_e; U_1 is found to be positive, meaning the electrostatic energy is reduced when the wire is formed. The quantity U_2 given in Eq. (7.6), on the other hand, consists of three terms. The first two terms represent the pattern shape effect on ΔW_e, and the sum of the two terms is positive since $\mathcal{K}_0 > 0$ and $\eta a \ll 1$. This indicates that the pattern on the electric plate also enhances the electrostatic energy reduction during the wire formation. The third term of U_2 corresponds to the misalignment effect on ΔW_e; this term is always negative, suggesting that the misalignment x_0 between the pattern and the wire causes an increment in the electrostatic energy. The finding shows

that it is sufficient to consider the aligning case, i.e. $x_0 = 0$, in the remaining part of the thesis.

After U_σ, U_1, and U_2 are calculated, the total energy change ΔE_{tot} due to the formation of the wire at $x_0 = 0$ can be determined by substituting Eqs. (3.6), (3.66), (3.76), and (3.78) into (3.79),

$$\begin{aligned}\Delta E_{tot} &= -w_{\sigma 0}\mathcal{S}VU_0 + 2\gamma_0 Ga - w_{e0}\mathcal{S}VU_1(\eta a) - 2w_{e0}\mathcal{S}_e VU_2(\eta a, \hat{d}) \\ &\quad + \frac{2g_0 l}{\mathcal{S}}\ln\left(\frac{\mathcal{S}a + H_f + l}{H_f + l}\right) + \frac{g_0 lV}{(H_f+l)^2} - \frac{2g_0 la}{H_f + l},\end{aligned} \tag{7.8}$$

where $G = -1 + \gamma/(\gamma_0\cos\phi)$ and γ denotes the surface energy density of the wire facet. The quantity G is positive in the SK system; the scenario where G is negative is beyond the scope of this thesis. Equation (7.8) shows how ΔE_{tot} depends on the material properties, the film thickness, the applied electric field, the wire/pattern size and slope, and the electric plate height. For the special case where $\eta a \ll 1$, U_1 and U_2 are given by Eqs. (7.5) and (7.6), and (7.8) is reduced to

$$\begin{aligned}\Delta E_{tot} &= -w_{\sigma 0}\mathcal{S}VU_0 + 2\gamma_0 Ga - \frac{1}{2}w_{e0}\mathcal{S}VU_0 - w_{e0}\mathcal{S}_e V\mathcal{K}_0 + \frac{2g_0 l}{\mathcal{S}}\ln\left(\frac{\mathcal{S}a + H_f + l}{H_f + l}\right) \\ &\quad - \frac{w_{e0}\eta^2V^2}{12\pi\mathcal{S}} + \frac{w_{e0}\mathcal{S}_e\mathcal{K}_2\eta^2V^2}{6\mathcal{S}} + \frac{g_0 lV}{(H_f+l)^2} - \frac{2g_0 la}{H_f + l}.\end{aligned} \tag{7.9}$$

7.2.3 Parameters and normalization

Before normalizing $\Delta\hat{E}_{tot}$ expressed in Eq. (7.9), it is helpful to introduce three key parameters of the ESMO process, namely, the normalized film thickness $\hat{H}_f$, the normalized stability number $\hat{\Sigma}$, and the electromolding (EM) strength $\mathcal{J}$. The three parameters dominate the characteristics of the total energy change and the size stability of the wire.

The normalized film thickness $\hat{H}_f$ is defined to be

$$\hat{H}_f = \frac{H_f + l}{H_1}, \tag{7.10}$$

where H_1 is the critical thickness for spontaneous island formation (or called the first critical thickness in the literature) (Chiu et al. 2004),

$$H_1 = \sqrt{\frac{g_0 l L}{\gamma_0 U_0 \mathcal{S}}}. \tag{7.11}$$

The quantity $L = \gamma_0 / w_{\sigma 0}$ in Eq. (7.11) gives the length scale at which the strain energy reduction due to the wire formation is balanced by the corresponding surface energy increment.

The normalized stability number $\hat{\Sigma}$ is given by (Chiu 2004)

$$\hat{\Sigma} = \frac{1}{G}\sqrt{\frac{g_0 l U_0 \mathcal{S}}{\gamma_0 L}} - 1. \tag{7.12}$$

A positive value of $\hat{\Sigma}$ means that the SK system can develop an island array that is stable against coarsening, while a negative value indicates the opposite. Since G is positive for the SK systems, the parameter $\hat{\Sigma}$ is larger than -1.

The EM strength $\mathcal{J}$ is expressed as

$$\mathcal{J} = 1 + \frac{1}{2}\hat{w}_{e0} + \hat{w}_{e0}\hat{\mathcal{S}}_e \frac{\mathcal{K}_0}{U_0}, \tag{7.13}$$

where $\hat{w}_{e0} = w_{e0}/w_{\sigma 0}$ and $\hat{\mathcal{S}}_e = \mathcal{S}_e/\mathcal{S}$. The parameter $\mathcal{J}$, depending on the normalized electrostatic energy density $\hat{w}_{e0}$, the ratio between the pattern and the wire slopes $\hat{\mathcal{S}}_e$, and the normalized pattern size $\hat{d}$, describes the effect of the electric field on ΔE_{tot} when $\eta a \ll 1$ and $x_0 = 0$. The variation of $\mathcal{J}$ with $\hat{d}$ and $\hat{\mathcal{S}}_e$ is plotted in Fig. 7.2 for the case where $\hat{w}_{e0} = 0.5$. The result indicates $\mathcal{J}$ increases with $\hat{d}$ and $\hat{\mathcal{S}}_e$.

In addition to $\hat{H}_f$, $\hat{\Sigma}$, and $\mathcal{J}$, the total energy change ΔE_{tot} is also affected by the parameter $\mathcal{J}_2 = -\pi \hat{w}_{e0} \hat{H}_f^4 (1 - 2\pi \hat{\mathcal{S}}_e \mathcal{K}_2)/(24 U_0 \mathcal{S}^2)$. Though influencing ΔE_{tot}, this parameter has little effect on the condition of the wire size stability.

By evoking the definitions of $\hat{H}_f$, $\hat{\Sigma}$, $\mathcal{J}$, and $\mathcal{J}_2$, the total energy change ΔE_{tot} ex-

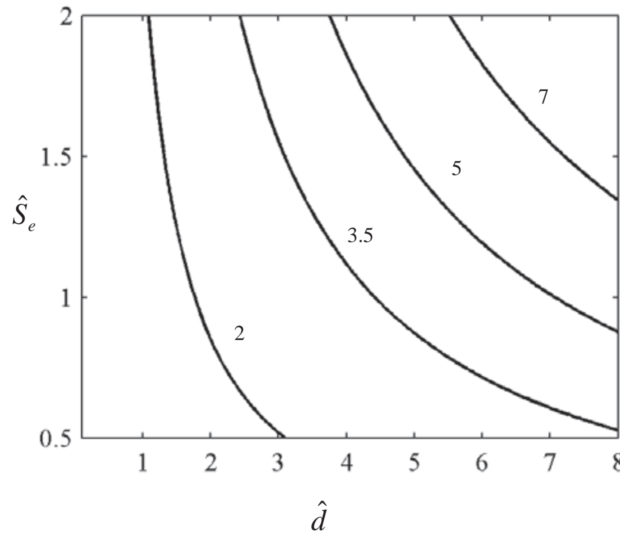

Figure 7.2: The contours of $\mathcal{J}$ as a function of $\hat{d}$ and $\hat{\mathcal{S}}_e$ for the case where $\hat{w}_{e0} = 0.5$.

pressed in Eq. (7.9) can be rewritten as

$$\Delta\hat{E}_{tot} = \ln(1+\hat{a}) + \hat{c}_1\hat{a} + \hat{c}_2\hat{a}^2 + \hat{c}_4\hat{a}^4, \tag{7.14}$$

where $\Delta\hat{E}_{tot} = \mathcal{S}\Delta E_{tot}/(2g_0 l)$, $\hat{a} = \mathcal{S}a/(H_f + l)$, and the three coefficients, $\hat{c}_1$, $\hat{c}_2$, and $\hat{c}_4$, are given by

$$\hat{c}_1 = \frac{\hat{H}_f - 1 - \hat{\Sigma}}{1+\hat{\Sigma}}, \tag{7.15}$$

$$\hat{c}_2 = \frac{1}{2}(1 - \mathcal{J}\hat{H}_f^2), \tag{7.16}$$

$$\hat{c}_4 = \frac{\mathcal{J}_2 H_1^2}{H_v^2}. \tag{7.17}$$

It is found that $\hat{c}_1$ and $\hat{c}_2$ are fully controlled by $\hat{H}_f$, $\hat{\Sigma}$, and $\mathcal{J}$, and $\hat{c}_4$ is proportional to H_v^{-2} as $H_v \to \infty$.

7.3 SK Systems without Electric Field

As a first step, this section focuses on the SK systems without an electric field. Of particular interest is the condition under which the systems can form a wire stable against

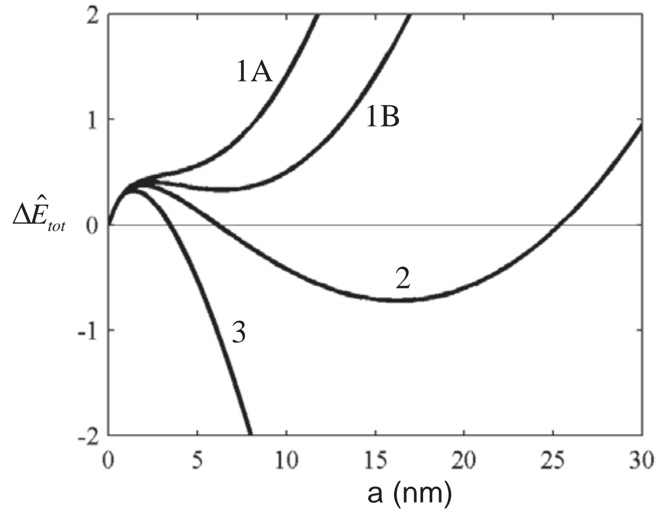

Figure 7.3: The variation of $\Delta\hat{E}_{tot}$ with $\hat{a}$ for the cases where $\hat{\Sigma} = 0.6$ and $\hat{H}_f = 0.97$, 0.98, 0.99, and 1.02, which are denoted by lines 1A, 1B, 2, and 3, respectively.

size variation. The results of this special case are used as a reference point for those under the influence of an electric field. The analysis follows closely those in (Chiu et al. 2004).

7.3.1 Characteristics of the total energy change

When the electric field is absent from the system, $w_{e0} = 0$, $\mathcal{J} = 1$, $\hat{c}_4 = 0$, and the total energy change ΔE_{tot} expressed in Eq. (7.14) is reduced to

$$\Delta\hat{E}_{tot} = \ln(1 + \hat{a}) + \hat{c}_1\hat{a} + \hat{c}_2^*\hat{a}^2, \tag{7.18}$$

where $\hat{c}_1$ is given in Eq. (7.15) and $\hat{c}_2^* = (1 - \hat{H}_f^2)/2$.

The variation of $\Delta\hat{E}_{tot}$ with $\hat{a}$ is plotted in Fig. 7.3 for the cases where $\hat{\Sigma} = 0.6$ and $\hat{H}_f = 0.97$, 0.98, 0.99, and 1.02. The results are denoted by lines 1A, 1B, 2, and 3, respectively. Lines 1A, 1B, and 2 describe typical examples of $\Delta\hat{E}_{tot}$ when $\hat{H}_f < 1$, and line 3 illustrates $\Delta\hat{E}_{tot}$ when $\hat{H}_f > 1$. These lines have the same property that the slope $d\Delta\hat{E}_{tot}/d\hat{a}$ is positive at $\hat{a} = 0$, while they differ in the maximum and minimum points of $\Delta\hat{E}_{tot}(\hat{a})$: Line 1A shows a monotonic increase of $\Delta\hat{E}_{tot}$ with $\hat{a}$, line 1B is distinguished by a maximum and a positive minimum of $\Delta\hat{E}_{tot}$, line 2 is similar to line 1B but the

minimum is negative, and line 3 is characterized by a maximum point followed by a monotonic decrease of $\Delta\hat{E}_{tot}$.

These characteristics of $\Delta\hat{E}_{tot}(\hat{a})$ signify different types of film morphology. In particular, lines 1A and 1B indicate $\Delta\hat{E}_{tot}$ is the lowest at $\hat{a} = 0$, meaning the wire cannot form and the flat film is the equilibrium morphology. The negative minimum on line 2, on the other hand, suggests the system can develop a wire stable against size variation. Wires can also form in the case of line 3 since $\Delta\hat{E}_{tot}$ can be negative; however, the lack of a minimum on line 3 means the wires are unstable in this case.

In brief, the film can be classified into three types of morphology, namely, the unstable wire, the stable wire, and the stable flat film. The unstable wire develops when $\hat{H}_f > 1$. The stable wire and the stable flat film, on the other hand, occur in the thickness range $\hat{H}_f < 1$; the condition differentiating the two types of morphology is further investigated in the next section.

7.3.2 Stability condition against size variation

The results depicted in Fig. 7.3 suggest that the film morphology is characterized by the stable wire when the following two conditions are satisfied.

- **Condition I:** There are one maximum and one minimum points in $\Delta\hat{E}_{tot}$.
- **Condition II:** The minimum of $\Delta\hat{E}_{tot}$ is negative.

The key quantities in the stable-wire conditions are the minimum/maximum points of $\Delta\hat{E}_{tot}$, which can be derived by solving the equation $\Delta\hat{E}_{tot}/d\hat{a} = 0$,

$$\hat{a}_1 = \frac{-(2\hat{c}_2^* + \hat{c}_1) - \sqrt{Q}}{4\hat{c}_2^*}, \tag{7.19}$$

$$\hat{a}_2 = \frac{-(2\hat{c}_2^* + \hat{c}_1) + \sqrt{Q}}{4\hat{c}_2^*}, \tag{7.20}$$

where $2\hat{c}_2^* + \hat{c}_1$ and Q are functions of $\hat{\Sigma}$ and $\hat{H}_f$,

$$2\hat{c}_2^* + \hat{c}_1 = \frac{\hat{H}_f}{1+\hat{\Sigma}}\left[1 - (1+\hat{\Sigma})\hat{H}_f\right], \quad (7.21)$$

$$\begin{aligned} Q &= (2\hat{c}_2^* + \hat{c}_1)^2 - 8(1+\hat{c}_1)\hat{c}_2^* \\ &= \frac{\hat{H}_f}{1+\hat{\Sigma}}\left[(1+\hat{\Sigma})^2\hat{H}_f^3 + 2(1+\hat{\Sigma})\hat{H}_f^2 + \hat{H}_f - 4(1+\hat{\Sigma})\right]. \end{aligned} \quad (7.22)$$

If both $\hat{a}_1$ and $\hat{a}_2$ are positive numbers, the two solutions correspond to the maximum and minimum points of $\Delta\hat{E}_{tot}$, respectively, meaning condition I is satisfied. In contrast, if any one of $\hat{a}_1$ and $\hat{a}_2$ is a negative or complex number, there is no minimum point in $\Delta\hat{E}_{tot}$ and condition I cannot be met.

The criterion of positive $\hat{a}_1$ and $\hat{a}_2$ holds in the overlapping region of the following three domains,

$$Q > 0, \quad (7.23)$$

$$2\hat{c}_2^* + \hat{c}_1 < 0, \quad (7.24)$$

$$\hat{c}_2^* > 0. \quad (7.25)$$

The first domain described by Eq. (7.23) ensures that $\hat{a}_1$ and $\hat{a}_2$ are real numbers, and the remaining two domains enforce $\hat{a}_1$ and $\hat{a}_2$ to be positive.

The three domains are plotted in Fig. 7.4(a) to determine the region of $(\hat{\Sigma}, H_f)$ that satisfies condition I. The results clearly show that condition I cannot be satisfied for SK systems with $\hat{\Sigma} < 0$. For SK systems with $\hat{\Sigma} > 0$, on the contrary, condition I is met if the normalized film thickness $\hat{H}_f$ falls into the range $[\hat{H}_Q, 1]$, where $\hat{H}_Q$ is the solution to the equation $Q(\hat{H}_Q, \hat{\Sigma}) = 0$. The critical thickness $\hat{H}_Q$ for condition I is equal to 1 at $\hat{\Sigma} = 0$ and decreases with increasing $\hat{\Sigma}$, see Fig. 7.4(a).

Calculating the minimum of $\Delta\hat{E}_{tot}$ in the thickness range $[\hat{H}_Q, 1]$ indicates the minimum $\Delta\hat{E}_{min}$ is always positive at $\hat{H}_f = \hat{H}_Q$, decreases gradually as $\hat{H}_f$ increases, and becomes zero at the thickness $\hat{H}_E$. The variation of $\hat{H}_E$ with $\hat{\Sigma}$ is plotted in Fig. 7.4(b). Similar to $\hat{H}_Q$, $\hat{H}_E$ is equal to 1 at $\hat{\Sigma} = 0$ and decreases as $\hat{\Sigma}$ increases. The domain

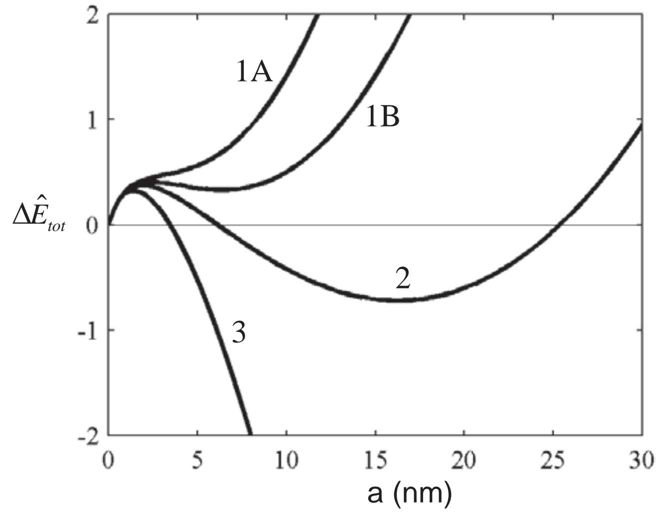

Figure 7.4: (a) The region of $(\hat{\Sigma}, \hat{H}_f)$ satisfying condition I; (b) the phase diagram of the film morphology of the SK systems without an electric field.

between $\hat{H}_f = \hat{H}_E(\hat{\Sigma})$ and $\hat{H}_f = 1$ gives the region of $(\hat{\Sigma}, \hat{H}_f)$ that satisfies conditions I and II for stable wires.

In summary, the dependence of the wire stability on the two parameters $\hat{\Sigma}$ and $\hat{H}_f$ of the SK systems can be illustrated by the phase diagram shown in Fig. 7.4(b). The diagram is divided into three regions along the two boundaries, $\hat{H}_f = 1$ and $\hat{H}_f = \hat{H}_E$. The region above the boundary $\hat{H}_f = 1$ corresponds to an unstable wire of which the total energy change $\Delta\hat{E}_{tot}$ is characterized by line 3 in Fig. 7.3. The region between the two boundaries identifies the SK systems that can develop wires stable against size variation, and $\Delta\hat{E}_{tot}(\hat{a})$ of this case is represented by line 2 in Fig. 7.3. The region below both boundaries refers to a stable flat film, and the total energy change is described by line 1A or 1B in Fig. 7.3.

7.4 Effects of Electric Field

This section examines the effects of H_v and d on the stability of wires against size variation for a typical coarsening system where $\hat{\Sigma} = -0.24$, $\hat{H}_f = 0.3$, $L = 100$ nm, $\hat{w}_{e0} = 3$, and $\mathcal{S} = \mathcal{S}_e = 1/5$. The results demonstrate the potential of using patterned electric plate to

fabricate stable wires. The results also reveal interesting features that motivate further stability analysis of the case where H_v and d are large in Sec. 7.6.

7.4.1 Characteristics of ΔE_{tot} and phase diagram of wire size stability

The size stability is determined by employing Eq. (7.8) to evaluate $\Delta E_{tot}(a)$ for different values of H_v and d. Typical examples are depicted in Fig. 7.5(a) where $H_v = 50$ nm and $d = 110$, 131, 140, and 160 nm. The results are found to be similar to those in Fig. 7.3 for the case without an electric field. The finding suggests the SK systems under the influence of an electric field can still be classified into the three types of film morphology discussed in Sec. 7.4, namely, a stable flat film, a stable wire, and an unstable wire.

The dependence of the film morphology on H_v and d is summarized by the phase diagram shown in Fig. 7.5(b). The diagram indicates stable flat films happen at small d and large H_v, unstable wires are triggered at large d and small H_v, and stable wires are obtained in the region between the two solid lines shown in the phase diagram. (The dashed boundaries in the diagram are discussed later in Sec. 7.5.2.) The existence of the stable wire region demonstrates that the EMSO process can cause an originally coarsening SK system to develop wires stable against size variation.

The stable wire region implies, for given electric plate height H_v, a range of pattern size d can be adopted to generate stable wires of different sizes. For example, taking d to be the value d_{max} on the upper boundary of the stable wire region results in the largest stable wire size $a_{eq(\max)}$, while adopting d_{min} on the lower boundary yields the smallest stable wire size $a_{eq(\min)}$. The size range $[a_{eq(\min)}, a_{eq(\max)}]$ of the stable wires is plotted in Fig. 7.5(c) as a function of H_v. The results show $a_{eq(\max)}$ increases with H_v, while $a_{eq(\min)}$ is insensitive to the electric plate height H_v.

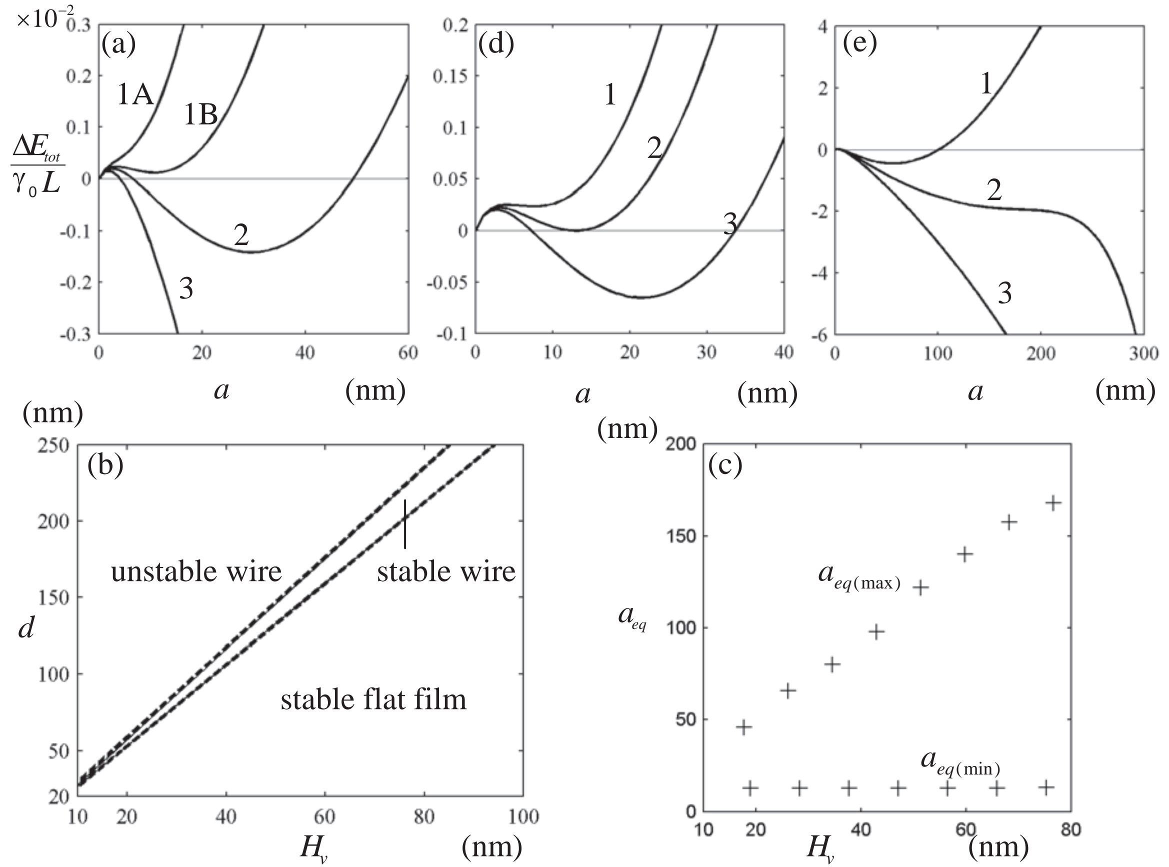

Figure 7.5: (a) The variation of $\Delta E_{tot}/\gamma_0 L$ with a for the cases where $H_v = 50$ nm and $d =$ 110, 131, 140, and 160 nm, denoted by lines 1A, 1B, 2, and 3, respectively. (b) The domains of (d, H_v) that lead to a stable flat film, a stable wire, and an unstable wire. (c) The variation of the stable wire sizes $a_{eq(\min)}$ and $a_{eq(\max)}$ with the electric plate height H_v. (d) The variation of $\Delta E_{tot}/\gamma_0 L$ with a for the cases where $H_v = 80$ nm and d is in the vicinity of the lower boundary of the stable wire region; $d = 205$, 212.4, and 220 nm for lines 1, 2, and 3, respectively. (e) The variation of $\Delta E_{tot}/\gamma_0 L$ with a for the cases where $H_v = 80$ nm and d is in the vicinity of the upper boundary; $d = 230$, 235, and 240 nm for lines 1, 2, and 3, respectively. The parameters adopted in the calculation are listed as follows. $L = 100$ nm, $\gamma_0 = 1$ J/m^2, $\gamma = 0.99$ J/m^2, $\hat{g}_0 = 0.15$, $l = 0.1$ nm, $\mathcal{S} = \mathcal{S}_e = 1/5$, $\hat{w}_{e0} = 3$, and $\hat{H}_f = 0.3$. The normalized stability number $\hat{\Sigma}$ can be evaluated to be -0.24.

7.4.2 Boundaries of stable wire region

After discussing the phase diagram of size stability and the effect of H_v on the range of stable wire size, the focus of this section turns to the two boundaries of the stable wire region.

The lower boundary is examined in Fig. 7.5(d) by depicting $\Delta E_{tot}(a)$ of three cases where the values of d are in the vicinity of the lower boundary and H_v is fixed. In particular, line 1 plots ΔE_{tot} when d is lower than the value d_{min} on the boundary, line 2 illustrates the result of the case where $d = d_{min}$, and line 3 presents that when $d > d_{min}$. The results indicate two properties of the lower boundary. First, the lower boundary is determined by the condition that the minimum of ΔE_{tot} is equal to zero. Second, the lower boundary signifies the onset of the morphological transition from a stable flat film to a stable wire. The morphological transition happens when the electric field effect caused by the patterned electrode is sufficiently strong.

Similarly, the upper boundary is investigated in Fig. 7.5(e) by considering the cases where d are lower than, equal to, and higher than the value d_{max} on the upper boundary. The results, denoted by lines 1, 2, and 3, respectively, demonstrate that the upper boundary corresponds to the morphological transition from a stable to an unstable wire, and is characterized by the scenario that the curvature of the minimum point of ΔE_{tot} vanishes. The characteristic suggests the wire becomes unstable against size variation if the electric field effect is too strong.

The lower and upper boundaries generally have to be determined by numerical methods, preventing the two boundaries from being described analytically. Further examination of the example depicted in Fig. 7.5(b), however, reveals that the two boundaries of the stable wire region approach straight lines at large values of d and H_v. The straight lines are expressed as $d = \alpha H_v$ (α is a constant), and are denoted by the dashed boundaries in the phase diagram. Motivated by the simple expression for the boundaries of the stable wire region, we investigate the wire size stability of the asymptotic cases in the next section.

7.5 The Asymptotic Cases

The size stability of the asymptotic case is analyzed by considering the onset of two critical morphological transitions, namely, the flat film-stable wire transition and the stable-unstable wire transition. The former is studied in Sec. 7.5.1, yielding the minimum criterion for the EM strength. The latter, imposing an upper limit on the EM strength, is investigated in Sec. 7.5.2. The results of the two sections are summarized in Sec. 7.5.3 to present an overall picture of the asymptotic cases. For convenience, the onset of the flat film-stable wire transition is termed the basic stable state, while that of the stable-unstable wire transition is called the utmost stable state.

7.5.1 Minimum criterion and basic stable states

The asymptotic cases are characterized by the condition that the height H_v and the pattern size d are large. This implies $\eta a = \pi a/H_v \ll 1$, and the total energy change $\Delta\hat{E}_{tot}$ can be expressed by Eq. (7.14). The expression can be further simplified by neglecting the term $\hat{c}_4\hat{a}^4$ when studying the basic stable states since Eqs. (7.15)–(7.17) and Fig. 7.5(c) suggest $\hat{c}_1$, $\hat{c}_2$, and $\hat{a}$ of the basic stable states are invariant with H_v, but $\hat{c}_4 \to 0$ as H_v approaches infinity. The simplification leads $\Delta\hat{E}_{tot}$ to

$$\Delta\hat{E}_{tot} = \ln(1+\hat{a}) + \hat{c}_1\hat{a} + \hat{c}_2\hat{a}^2, \qquad (7.26)$$

where $\hat{c}_1$ is a function of $\hat{H}_f$ and $\hat{\Sigma}$, and $\hat{c}_2$ is that of $\hat{H}_f$, $\hat{\Sigma}$, and the EM strength $\mathcal{J}$. Differentiating Eq. (7.26) with respect to $\hat{a}$ and requiring the result to be zero yield an equation for the wire size $\hat{a}_{min}$ at the minimum point,

$$\frac{1}{1+\hat{a}_{min}}\left[2\hat{c}_2\hat{a}_{min}^2 + (\hat{c}_1 + 2\hat{c}_2)\hat{a}_{min} + 1 + \hat{c}_1\right] = 0. \qquad (7.27)$$

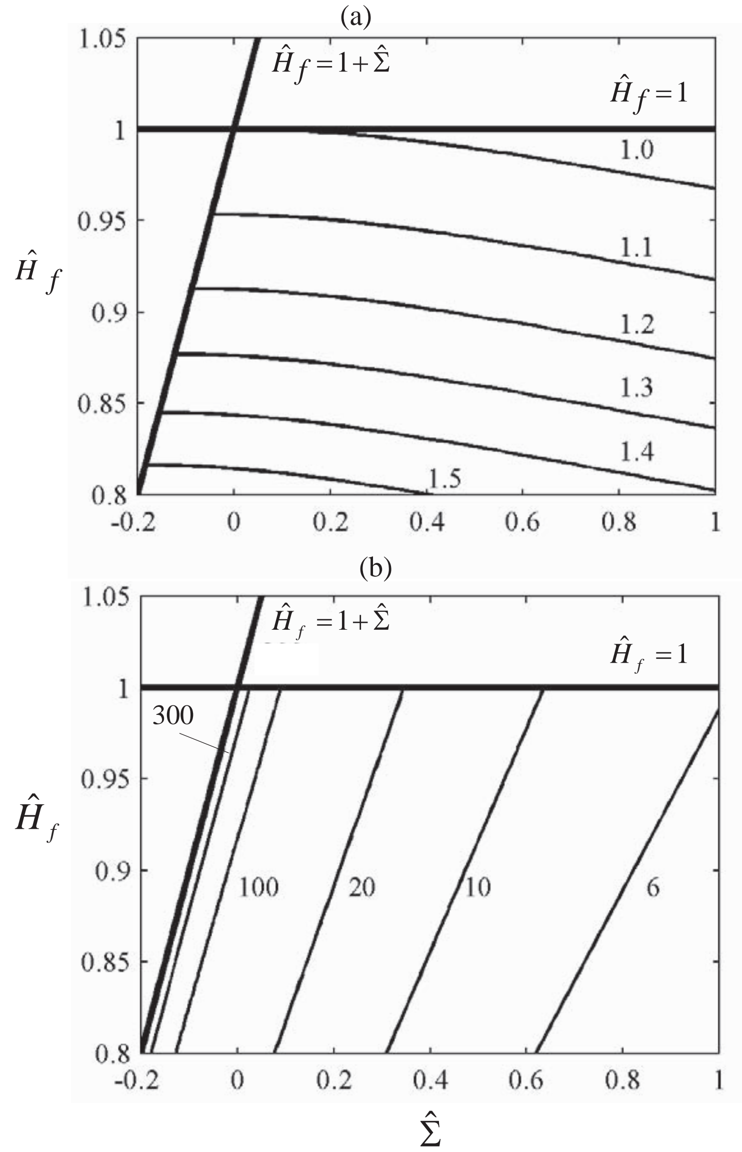

Figure 7.6: The contours of (a) $\mathcal{J}_{min}$ and (b) $\hat{a}_{min}$ of the basic stable states as functions of $\hat{\Sigma}$ and $\hat{H}_f$.

The minimum point corresponds to a basic stable state if the total energy change is zero at that point,

$$\ln(1 + \hat{a}_{min}) + \hat{c}_1 \hat{a}_{min} + \hat{c}_2 \hat{a}_{min}^2 = 0. \tag{7.28}$$

Equations (7.27) and (7.28) constitute the conditions of the basic stable states.

The procedure for solving the two conditions given in Eqs. (7.27) and (7.28) can be described as follows. For a given set of $\hat{H}_f$ and $\hat{\Sigma}$, the coefficient $\hat{c}_1$ can be calculated by

Eq. (7.15). After $\hat{c}_1$ is known, Eqs. (7.27) and (7.28) are two equations of $\hat{a}_{min}$ and $\hat{c}_2$, and the solutions can be obtained numerically. Substituting the result of $\hat{c}_2$ into Eq. (7.16) yields the EM strength $\mathcal{J}$ for the basic stable state. This critical value is denoted as $\mathcal{J}_{min}$ since it is also the minimum EM strength needed in order to induce a stable wire.

Minimum EM strength and viable region

The contours of $\mathcal{J}_{min}$ are plotted in Fig. 7.6(a) as a function of $\hat{\Sigma}$ and $\hat{H}_f$. The figure indicates the contours are present in the overlapping region of the following two domains,

$$\begin{aligned} \hat{H}_f &\leq 1, \\ \hat{H}_f &\leq 1 + \hat{\Sigma}. \end{aligned} \tag{7.29}$$

The overlapping region identifies the SK systems that can be activated by the EMSO process to develop wires stable against size variation, and is termed the viable region. Evidently, the SK systems outside the viable region cannot realize the size stability during the EMSO process.

The viable region illustrated in Fig. 7.6(a) suggests all of the non-coarsening SK systems ($\hat{\Sigma} > 0$) with $\hat{H}_f < 1$ can develop stable wires during the EMSO process. This is in contrast to the case without an electric field where the stable states can only occur in a much smaller thickness range $[\hat{H}_E(\hat{\Sigma}), 1]$. In addition to the non-coarsening systems, the viable region also includes the coarsening systems with $\hat{H}_f$ in the range $[0, 1 + \hat{\Sigma}]$.

The viable region of stable states can be further divided into two areas along the contour $\mathcal{J}_{min} = 1$. The area above the contour is characterized by $\mathcal{J}_{min} < 1$. Since $1 \leq \mathcal{J}$, this characteristic means the condition $\mathcal{J}_{min} < \mathcal{J}$ is always satisfied, and the corresponding SK systems can develop stable wires even if $\hat{w}_{e0} = 0$. This area, as a matter of fact, is the stable wire region shown in Fig. 7.4(b) for SK systems without an electric field.

In comparison, the area below the contour $\mathcal{J}_{min} = 1$ is characterized by $\mathcal{J}_{min} > 1$. In this area, the EM strength has to be higher than the minimum value in order to activate

the stable states. The required minimum strength $\mathcal{J}_{min}$ decreases when $\hat{\Sigma}$ and/or $\hat{H}_f$ increases.

Wire size of basic stable states

Turn to $\hat{a}_{min}$, the wire size of the basic stable states and the smallest size of the stable wires in the asymptotic cases. As discussed earlier in this section, $\hat{a}_{min}$ can be obtained by solving Eqs. (7.27) and (7.28) with given $\hat{\Sigma}$ and $\hat{H}_f$. This shows $\hat{a}_{min}$ is fully controlled by $\hat{\Sigma}$ and $\hat{H}_f$ of the SK systems, independent of the electric field generated by the patterned electrode. The result explains the finding in Fig. 7.5(c) that the smallest stable wire size $a_{eq(\mathrm{min})}$ is insensitive to the electric plate height H_v.

The effects of $\hat{\Sigma}$ and $\hat{H}_f$ on the wire size $\hat{a}_{min}$ of the basic stable states are depicted in Fig. 7.6(b). The results indicate $\hat{a}_{min}$ decreases when $\hat{\Sigma}$ is raised or $\hat{H}_f$ is reduced, while $\hat{a}_{min}$ increases drastically when approaching the boundary $\hat{H}_f = 1 + \hat{\Sigma}$ of the viable region. The wire size $\hat{a}_{min}$ in the vicinity of the boundary is further explored below.

The basic stable states in the vicinity of $\hat{H}_f = 1 + \Sigma$

When studying the basic stable states in the vicinity of the boundary $\hat{H}_f = 1 + \hat{\Sigma}$, it is convenient to express the coefficient $\hat{c}_1$ as $\hat{c}_1 = -\epsilon$ where ϵ is a positive number with small magnitude. Substituting the expression into Eq. (7.26) and employing the change of variable $t = \hat{a}_{min}\epsilon$ reduce $\Delta\hat{E}_{tot}$ given in Eq. (7.26) to

$$\Delta\hat{E}_{tot} = \ln t - \ln \epsilon t + \frac{\hat{c}_2 t^2}{\epsilon^2}. \tag{7.30}$$

The minimum point of $\Delta\hat{E}_{tot}$ is determined by solving the equation $\Delta\hat{E}'_{tot}(t) = 0$, which can be rewritten as

$$\frac{\hat{c}_2 t^2}{\epsilon^2} - \frac{t}{2} + \frac{1}{2} = 0. \tag{7.31}$$

According to (7.31), $\Delta\hat{E}_{tot}$ at the minimum point can be calculated to be

$$\Delta\hat{E}_{min} = \ln t - \ln\epsilon - \frac{t}{2} - \frac{1}{2}. \tag{7.32}$$

It can be verified later that $t \gg 1$ at small values of ϵ. Thus, $t \gg \ln t$, $|\ln\epsilon| \gg 1/2$, and $\Delta\hat{E}_{min}$ can be further simplified to

$$\Delta\hat{E}_{min} = -\ln\epsilon - \frac{t}{2}. \tag{7.33}$$

The minimum $\Delta\hat{E}_{min}$ vanishes at the basic stable states, leading to the solution $t = -2\ln\epsilon$. The result confirms the assertion that $t \gg 1$ as $\epsilon \to 0$. The result also determines the stable wire size $\hat{a}_{min}$ in the vicinity of the boundary to be

$$\hat{a}_{min} = \frac{-2\ln\epsilon}{\epsilon}. \tag{7.34}$$

Equation (7.34) explains the result depicted in Fig. 7.6(b) that $\hat{a}_{min}$ increases drastically when approaching the boundary $\hat{H}_f = 1 + \hat{\Sigma}$.

Substituting the solution of t into Eq. (7.31) and ignoring the smallest term $-1/2$ yields

$$\hat{c}_2 = \frac{\epsilon^2}{2t} = -\frac{\epsilon^2}{4\ln\epsilon}. \tag{7.35}$$

Comparing Eq. (7.35) with (7.16) gives the required minimum EM strength $\mathcal{J}_{min}$ in the vicinity of the boundary $\hat{H}_f = 1 + \hat{\Sigma}$,

$$\mathcal{J}_{min} = \left(1 + \frac{\epsilon^2}{2\ln\epsilon}\right)\frac{1}{\hat{H}_f^2}. \tag{7.36}$$

Equation (7.36) indicates that the minimum EM strength J_{min} on the boundary $\hat{H}_f = 1 + \hat{\Sigma}$ is given by $1/\hat{H}_f^2$, which is independent of the parameter $\hat{\Sigma}$.

7.5.2 Maximum EM strength and utmost stable states

This section first focuses on the maximum EM strength under the condition $\hat{c}_4 < 0$, which is satisfied when $\hat{\mathcal{S}}_e < 1$. It is then shown that the result is also applicable to the cases with $\hat{c}_4 > 0$.

The utmost stable states, as shown in Fig. 7.5(e), are characterized by a stationary point with zero curvature in $\Delta\hat{E}_{tot}$ to signify the onset of no minimum in the total energy change. The characteristic can be described by the two equations, $\Delta\hat{E}'_{tot}(\hat{a}_{max}) = \Delta\hat{E}''_{tot}(\hat{a}_{max}) = 0$. By assuming $\hat{c}_4 < 0$, the two equation can be expressed as

$$\frac{1}{1+\hat{a}_{max}} + \hat{c}_1 + 2\hat{c}_2\hat{a}_{max} + 4\hat{c}_4\hat{a}_{max}^3 = 0, \tag{7.37}$$

$$-\frac{1}{(1+\hat{a}_{max})^2} + 2\hat{c}_2 + 12\hat{c}_4\hat{a}_{max}^2 = 0, \tag{7.38}$$

where $\hat{a}_{max}$ is the wire size of the utmost stable state. Comparing the order of magnitude of the terms in Eqs. (7.37) and (7.38) suggests $(1+\hat{a}_{max})^{-1}$ and $(1+\hat{a}_{max})^{-2}$ can be neglected, simplifying the two equations to

$$\hat{c}_1 + 2\hat{c}_2\hat{a}_{max} + 4\hat{c}_4\hat{a}_{max}^3 = 0, \tag{7.39}$$

$$2\hat{c}_2 + 12\hat{c}_4\hat{a}_{max}^2 = 0. \tag{7.40}$$

Equations (7.39) and (7.40) can be solved to express $\hat{c}_2$ and $\hat{a}_{max}$ in terms of $\hat{c}_1$ and $\hat{c}_4$,

$$\hat{a}_{max} = \left(\frac{\hat{c}_1}{8\hat{c}_4}\right)^{1/3}, \tag{7.41}$$

$$\hat{c}_2 = -\frac{3\hat{c}_1}{4\hat{a}_{max}}. \tag{7.42}$$

Since $\hat{c}_4$ is proportional to H_v^{-2} when H_v approaches infinity, Eqs. (7.41) and (7.42) imply $\hat{a}_{max} \propto H_v^{2/3}$ and $\hat{c}_2 \propto H_v^{-2/3}$. The result $\hat{a}_{max} \propto H_v^{2/3}$ confirms the insignificance of $(1+\hat{a}_{max})^{-1}$ and $(1+\hat{a}_{max})^{-2}$ in Eqs. (7.37) and (7.38), respectively.

The finding that $\hat{c}_2$ is proportional to $H_v^{-2/3}$ at larger values of H_v determines the EM strength of the utmost stable states or equivalently the maximum EM strength $\mathcal{J}_{max}$ allowed for stable wires,

$$\mathcal{J}_{max} = \frac{1}{\hat{H}_f^2}. \tag{7.43}$$

Equation (7.43) indicates $\mathcal{J}_{max}$ is independent of the normalized stability number $\hat{\Sigma}$.

For the case where $\hat{c}_4 > 0$, it is necessary to include higher order terms of $\hat{a}$ in order to determine the maximum stable size $\hat{a}_{max}$. The maximum EM strength $\mathcal{J}_{max}$, however, is still given by Eq. (7.43) because the coefficients of the higher order terms, similar to $\hat{c}_4$, all decay to zero as $H_v \to \infty$. In such a case, the minimum point of $\Delta\hat{E}_{tot}$ would cease to exist when $\hat{c}_2 \leq 0$. The critical condition $\hat{c}_2 = 0$ leads to the maximum EM strength expressed in Eq. (7.43).

7.5.3 Size stability of wires

The results in Secs. 7.5.1 and 7.5.2 reveal that the size stability of wires in the asymptotic cases is determined by two criteria. The first one is the viability criterion expressed in Eq. (7.29). This criterion evaluates whether or not the SK system can be activated by the electric field to develop stable wires during the EMSO process. Failing the viability criterion indicates stable wires cannot be produced on the SK system during the EMSO process. Satisfying the viability criterion, on the other hand, means stable wires can be generated if the EM strength $\mathcal{J}$ meets the second criterion that $\mathcal{J}$ is in the range of $\mathcal{J}_{min}$ to $\mathcal{J}_{max}$,

$$\mathcal{J}_{min}(\hat{H}_f, \hat{\Sigma}) \leq \mathcal{J}(\hat{w}_{e0}, \hat{d}, \hat{\mathcal{S}}_e) \leq \mathcal{J}_{max}(\hat{H}_f). \tag{7.44}$$

Since $\mathcal{J} \geq 1 + \hat{w}_{e0}/2$, the second criterion imposes an upper bound for the normalized electrostatic energy density $\hat{w}_{e0}$,

$$\hat{w}_{e0} \leq \hat{w}_{e(\max)} = 2\left(\frac{1}{\hat{H}_f^2} - 1\right). \tag{7.45}$$

For a viable SK system with a given $\hat{w}_{e0}$ below its upper bound $\hat{w}_{e(\max)}$, the solution to the second criterion for stable wires is given by the region of $(\hat{d}, \hat{\mathcal{S}}_e)$ between the contours $\mathcal{J}(\hat{d}, \hat{\mathcal{S}}_e) = \mathcal{J}_{min}$ and $\mathcal{J}(\hat{d}, \hat{\mathcal{S}}_e) = \mathcal{J}_{max}$. Consider the case where $\hat{H}_f = 0.4472$, $\hat{\Sigma} = 1.715$, and $\hat{w}_{e0} = 0.5$ for example. The values of $\hat{H}_f$ and $\hat{\Sigma}$ yield $\mathcal{J}_{min} = 3.5$ and $\mathcal{J}_{max} = 5$. Thus, the stable wire region $(\hat{d}, \hat{\mathcal{S}}_e)$ of this case is between the contours $\mathcal{J} = 3.5$ and $\mathcal{J} = 5$, see Fig. 7.2. It is found that $\hat{d}$ in the region increases with decreasing $\hat{\mathcal{S}}_e$.

The region of $(\hat{d}, \hat{\mathcal{S}}_e)$ for stable wires is reduced to a range of normalized pattern size $[\hat{d}_{min}, \hat{d}_{max}]$ when $\hat{\mathcal{S}}_e$ is fixed. The two limits, $\hat{d}_{min}$ and $\hat{d}_{max}$, explain the finding in Fig. 7.5(b) that the upper and lower boundaries of the stable wire region approach straight lines in the asymptotic cases. The two limits also suggest the straight lines are given by $d = \hat{d}_{min} H_v$ and $d = \hat{d}_{max} H_v$.

As a remark, the maximum EM strength J_{max} expressed in Eq. (7.43) is always larger than the minimum EM strength J_{min} in the viable region. This can be understood as follows. We first compare J_{max} and J_{min} on the boundary $\hat{H}_f$, where the former is expressed in Eq. (7.43) and the latter in Eq. (7.45). The comparison shows J_{max} and J_{min} coincide on the boundary. Nevertheless, except on the boundary, the upper and lower limits of the EM strength are different. In particular, J_{min} decreases if $\hat{H}_f$ is fixed but $\hat{\Sigma}$ decreases, see Fig. 7.6 and Eq. (7.43). On the other hand, $\mathcal{J}_{max}$ remains the same as long as $\hat{H}_f$ is fixed. This demonstrates that $\mathcal{J}_{max} \geq \mathcal{J}_{min}$ in the viable region for the stable wires.

7.6 Numerical Simulation

In addition to the energy analysis, we also carried out simulation for the morphological evolution of the SK system during the EMSO process. The EMSO method is essentially

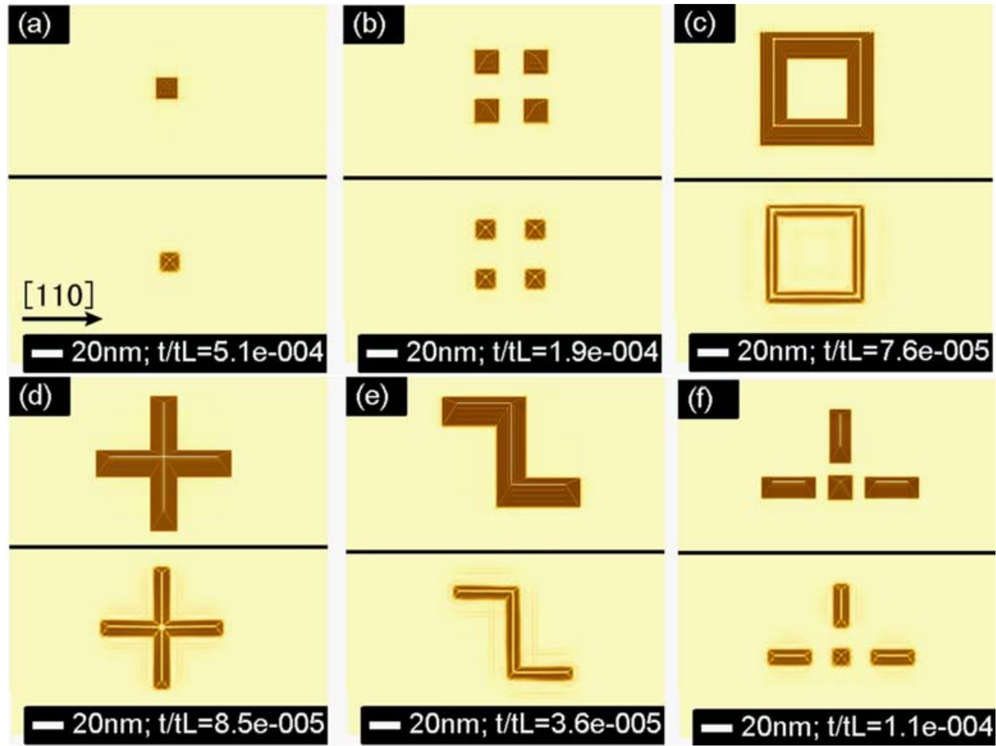

Figure 7.7: The simulation results of the EMSO process for the system described in Fig. 7.1 with $\hat{w}_{e0} = 2$, $H_f = 2$ nm, and $H_v = 10$ nm, $L = 50$ nm. By using different patterns, the EMSO process produces (a) a single island, (b) a 2×2 island array, (c) a square ring, (d) a cross-junction, (e) a zigzag wire, and (f) a structure with potential applications in single-electron transistors. The patterns are depicted on the top and the resulting nanoislands at the bottom of each part of the figure.

an annealing process of the SK system under a non-uniform electric field (Chiu et al. 2006), and the morphological evolution morphological evolution is dictated by Eqs. (2.6) and (2.7).

Figure 7.7 plots the simulation results of the EMSO process for the SK system described in Fig. 7.1. In addition, the surface energy density $\gamma(\mathbf{n})$ contained shallow minimums at {113} and {116} to model the development of facets on the nano-structures. Figure 7.7(a) presents the pattern profile and the resulting pyramid island morphology at the steady state. The simulation result clearly indicates that the EMSO process can produce islands aligning well with the patterns. To test the stability of the island against size variation, the island in Fig. 7.7(a) is enlarged by about 10% and then subject to the EMSO process with the original pattern on the electric plate. It is found that the enlarged island could return to the original size. The stability is also tested by adding

shallow bumps and random roughness in the initial film surface. The results showed the bumps and the initial roughness had no significant effect on the geometry or the formation time of the nanostructure induced by the pattern. The two tests demonstrate that the EMSO process can lead the system to the intended equilibrium/meta-stable states.

Besides the pyramids shown in Fig. 7.7(a), more complicated shapes of island may also be "molded" by the EMSO process using different patterns. The examples demonstrated in our simulation include 2×2 island arrays, square rings, cross junctions, straight and zigzag wires; see Figs. 7.7(b)–7.7(e). These examples, though incomprehensive, strongly imply the EMSO process is capable of fabricating a wide range of three-dimensional structures for the nano-technologies. The structures can be the basic building blocks of quantum dot cellular automa, single-electron transistors, nano-electronics, and opto-electronics (Orlov et al. 1997).

7.7 Discussion

7.7.1 Modification of SK systems for stable nanostructures

In this section we briefly discuss how to modify the SK systems in order to satisfy the viability criterion for stable nanostructures. The approach depends on whether the film is a conductor or a semiconductor. For conductor films, the interaction energy strength $g_0 l$ is high; thus, the critical thickness H_1 for the SK transition is large, and $\hat{\Sigma}$ is a positive value. In those systems, the viability criterion can be fulfilled by simply decreasing the film thickness H_f below H_1.

As an example, consider the case where the film is silver, $\epsilon_m = 0.02$, $E = 83$ GPa, $\nu = 0.37$, $\gamma_0 = 1$ J/m^2, $L = 27.7$ nm, $\hat{\gamma} = 0.99$, and $\phi = 10°$. The interaction energy strength $g_0 l$ of silver films was estimated to be 6.62×10^{-10} J/m (Suo and Zhang 1998). Substituting the value of $g_0 l$ and the material properties into Eqs. (7.12) and (7.11) yields $\hat{\Sigma} = 15.4$ and $H_1 = 7.7$ nm. Since $\hat{\Sigma} > 0$, the film would satisfy the viability criterion if H_f is less than $H_1 = 7.7$ nm.

The large value of H_1 implies a_{min} can be small even at moderate film thickness. For instance, a film of 4.8 nm ($\hat{H}_f = 0.622$) in our current case yields $a_{min} = 12.2$ nm when the electric field is taken to be 0.073 volt/nm and the pattern is described by $\hat{d} = 2.5$ and $\phi_e = 10°$. The size a_{min} is reduced to 1.86 nm if H_f is equal to 1.5 nm, and a high electric field of 1.29 volt/nm is applied.

Turn to the semiconductor film-substrate systems. It is more difficult to meet the viability criterion in those systems because the interaction strength $g_0 l$ is much smaller. One possible solution is to enhance the strength by doping the film heavily. It was suggested that the strength $g_0 l$ of a SiGe film could reach 5.7×10^{-12} J/m when introducing one atomic percent of donors in the film (Chiu 2004). This interaction strength can produce $a_{min} = 26$ nm for the case where $L = 100$ nm, $\phi = 11.3°$, $\hat{\gamma} = 0.99$, and $H_f = 0.4$ nm, which roughly corresponds to the SiGe film with 25% of Ge in atomic concentration. The equilibrium island size can be further reduced if the interaction strength can be increased significantly. This, however, requires a different interaction mechanism, a crucial issue that needs to be explored in the future.

7.7.2 Kinetics

After discussing the possible approaches for satisfying the size stability criteria, we comment briefly in this section whether or not the stable nanostructures can develop during a typical annealing process where surface diffusion is the dominating kinetic mechanism. To answer this question, it is helpful to compare the simulation results in Fig. 7.7 and Fig. 5.1. Both adopt the same model for the SK systems to study the growth of nanoislands driven by the surface diffusion mechanism, while the two results differ in the electric field: Figure 7.7 takes into account the effects of the electric field generated by a patterned electric plate; in contrast, Fig. 5.1 focuses on the cases where the electric field is absent.

Figures 7.7 and 5.1 also present the results in term of the normalized time t/t_L. It is found that the normalized time t/t_L for the formation of nanostructures during the EMSO process is less than 5×10^4, see Fig 7.7. The results plotted in Fig. 5.1, on the

other hand, suggest the normalized formation time t/t_L is about 0.5 during the annealing process without the electric field.

The comparison of the two results reveals that the growth of nanoislands under a patterned electric plate is much faster than that without the electric field. Since the latter can be observed in experiments routinely, the patterned-induced island formation is expected to be feasible.

The effect of a pattern on the growth rate of nanostructures can be understood as follows. The growth of nanostructures in SK systems without an electric field is driven by the strain energy reduction, and it follows from Eq. (3.3) that the corresponding energetic force for island growth is given by the negative of the strain energy density $-w(x)$. (This is analogous to the energetic force due to the electrostatic energy discussed in Sec. 3.2.3.) This energetic force, as expressed in Eq. (3.9), increases with the slope and size of the nanostructure. Thus, the energetic force for island growth is small when the film morphology is a slightly rough surface profile.

The pattern on the electric plate, on the contrary, induces an energetic force that is independent of the geometry of the nanoislands on the film surface. This energetic force can be large even when the nanostructures on the film are still shallow and/or small. This explains why the pattern can accelerate the growth of nanostructures drastically.

7.7.3 Controlled growth of nanoislands

The size stability analysis presented in this section illustrates a potential method for controlling the self-assembly of nanostructures. The first step is to choose a system that can satisfy the viability criterion given in Eq. (7.29). The system can be a coarsening one characterized by $\hat{\Sigma} < 0$ or a stable one with $\hat{\Sigma} > 0$, while the stable one is a better choice since it allows a larger thickness range for fabricating stable nanostructures.

The stable SK system can develop stable wires without an electric field if the normalized thickness $\hat{H}_f$ is in the range $\hat{H}_E < \hat{H}_f < 1$, where $\hat{H}_E$ is defined earlier in Fig. 7.4. This range, however, is unsuitable for controlling the island growth since the nanostructures can develop at any location on the film surface.

The controllable self-assembly of nanoislands is achieved by using films in the thickness range $\hat{H}_f < \hat{H}_E$ together with a patterned electric plate. In this design, the flat film is the equilibrium morphology in the areas with little influence from the patterns, while the flat film is transformed into stable nanostructures in the area affected by the pattern. The transformation can occur if the EM strength $\mathcal{J}$ due to the patterns satisfies the criterion expressed in Eq. (7.44), which in turn defines a stability domain of the pattern parameters. Varying the pattern geometry within the stability domain leads to different sizes and shapes of stable nanostructures at the specified locations.

For a given SK system, $\hat{\Sigma}$ is fixed, and the smallest size of stable nanostructures $\hat{a}_{min}$ can be reduced by decreasing the normalized thickness $\hat{H}_f$, see Fig. 7.3(b). Decreasing $\hat{H}_f$, however, causes $\mathcal{J}_{min}$ and thus the electric field to increase, see Fig. 7.3(a). The electric field can become too high to be feasible in the actual systems, and this imposes a constraint on the smallest film thickness that can be attained in the process.

7.7.4 Limitations

The analysis presented in this section provide a simple scheme for determining the size stability of wires under the influence of a patterned electric plate. The scheme, nevertheless, overlooks several issues that can affect the size stability. For example, the formulas adopted here for calculating the strain and electrostatic energy changes are accurate to the first order of the wire slope. This is valid for shallow islands, while the effects of large wire slopes have to be included in order to have more accurate predictions of the size stability.

Besides the large slopes, other issues that need to be considered include the kinetics of the EMSO process, the surface stress, other mechanisms of the interaction energy in SK systems such as SiGe and III-V compounds, the electrostatics of semiconductor films, bulk diffusion of alloy film, and the evaporation of As in III-V compounds. Understanding these issues is essential for developing technologies that can control the growth of nanoislands in the SK systems.

7.8 Summary

This chapter investigates the stability of wires against size variation for SK systems during the EMSO process. The investigation starts with the case where the electric field is absent from the process. In such a case, the wire is stable against size variation if the normalized stability number $\hat{\Sigma}$ is positive and the normalized film thickness $\hat{H}_f$ is within the range $[\hat{H}_E, 1]$. The variation of the thickness range with $\hat{\Sigma}$ is illustrated in Fig. 7.4(b).

The investigation then turns to a typical example of coarsening SK system to study the effects of d and H_v on the wire size stability. The results show that the coarsening system can be activated to develop stable wires of different sizes when the pattern size d and the electric plate height H_v are in the stable wire region depicted in Fig. 7.5(b). The results also indicate the upper limit of the wire size $a_{eq(\max)}$ increases with H_v, while the lower limit $a_{eq(\min)}$ is insensitive to the parameters of the electric field.

Motivated by the findings in the specific example, the investigation further explores the wire size stability of the asymptotic cases where the pattern size d and the electric plate height H_v are large. The size stability is shown to be determined by two criteria. The first one, the viability criterion given in Eq. (7.29), evaluates whether or not the SK system can be activated by the electric field to generate stable wires. The second criterion, expressed in Eq. (7.44), requires that the EM strength $\mathcal{J}$ is in the range $[\mathcal{J}_{min}, \mathcal{J}_{max}]$.

In conclusion, the EMSO process adopts a patterned electrode to effect island formation on the film of an SK system below the critical thickness for the SK transition. The EMSO process has enormous potential for the self-assembly of nanostructures. The EMSO process works well for conductor films on semiconductor substrates; and it is conjectured that the process can also be extended to semi-conductor and dielectric films on semiconductor substrates. The EMSO process can be implemented without much difficulty since the enabling technologies for the realization of the process are already demonstrated in the LISA method and the growth of the SK systems. Most importantly, the EMSO process can produce islands at the equilibrium/meta-stable state, and the process can control the sizes, shapes, and sites of the islands.

Chapter 8

Conclusion

This thesis presents our research on the nanostructures formation in Stranski-Krastanow film-substrate system with and without the effects of electric field. The physics of the nanostructure formation is investigated via two methods: the 3D numerical simulation for the morphological evolution and the energy analysis for the nanostructures. Our results provide qualitative explanation for experimental observations of nanostructure formation in the SK system. The results also lead to our proposed schemes to control the self-assembly of nanostructures in term of the sizes, the sites, and the shapes.

Chapters 2 and 3 show the first-order boundary perturbation model adopted in our research. The model allows us to compute the key energy components in the SK system, including the strain energy, the surface energy, the interaction energy and the electro-static energy.

Chapter 4 discusses our study about the critical film thickness which is dictated by the mechanism of nanostructures formation: spontaneous formation by nucleation and gradual morphological transition by surface diffusion. It shows that the critical thickness under surface undulation is generally larger than that under spontaneous formation. The difference in the critical thickness implies that there is a special thickness range in which an almost flat film can develop into islands via spontaneous formation where the the surface undulation is suppressed. It is demonstrated in that chapter that the thickness range can be used to control the nanostructure formation via the ASKT method.

Chapter 5 investigates the nanostructure formation of typical Stranski-Krastanow systems by simulating the surface undulation of the system driven by the surface diffusion mechanism. The results lead to the following findings.

- The whole nanostructure formation process on the SK system is characterized by the surface undulation, the shape transition, and the formation of wetting layer. The unique feature of the shape transition is the invariance of the basic width during the process.
- Three types of film morphologies appear during the nanostructure formation process without the effect of electric field: an array of separate islands; localized wetting layers and induced facets; and a faceted ripple structure.
- The film morphology is controlled by the maximum surface coverage of faceted islands. As maximum surface coverage increases, the film morphology changes gradually from the sparse array to localized wetting layer and finally to the faceted ripple structures. The maximum surface coverage depends on three parameters of the SK systems, namely the ratio between the interaction energy density and strain energy density, the normalized film thickness , and the strength of the minimum of surface energy density on (001).

Chapter 6 presents the formation of quantum dot molecules on a thick film. The results demonstrate that the special nanostructures can grow by the surface undulation process on a thick film with shallow indents via the unique cooperative formation of faceted trenches and ridges. The cooperative formation mechanism is further explored from the energetic points of view by considering the crucial moment when the formation of a faceted island adjacent to a trench become more favorable than the growth of the trench itself. It is also demonstrated in the chapter that the critical trench size can be determined analytically. The critical trench size for favorable growth of adjacent faceted island suggests that alternative development of trenches and ridges is a self-limiting process dictating the size selection of the quantum dots molecules.

Chapter 7 presents our theoretical study of the SK transition under the effect of electric field and demonstrates that it is feasible to self-assemble nanostructures with controllable sites, sizes,and shapes by using patterned electric field when the viability criterion is satisfied.

Bibliography

Asaro, R. J., Tiller, W. A., 1972. Interface morphology development during stress corrosion cracking: part i. via surface diffusion. Metall. Trans. 3, 1789–1796.

Ballet, P., Smathers, J. B., Yang, H., Workman, C. L., Salamo, G. J., 2000. Scanning tunneling microscopy investigation of truncated InP/GaInP$_2$ self-assembled islands. Appl. Phys. Lett 77, 3406–3408.

Barth, J. V., Costantini, G., Kern, K., 2005. Engineering atomic and molecular nanostructures at surfaces. Nature 437, 671–679.

Beer, G., 2001. Programming the Boundary Element Method: An Introduction for Engineer. John Wiley & Sons, New York.

Berbezier, I., Ronda, A., 2007. Self-assembling of Ge dots on nanopatterns: Experimental investigation of their formation, evolution and control. Phys. Rev. B 75, 19–28.

Borgström, M., Zela, V., Seifert, W., 2003. Arrays of ge islands on Si(001) grown by means of electron-beam pre-patterning. Nanotechnology 14, 264–267.

Bouville, M., Millunchick, J. M., Falk, M. L., 2004. Pit nucleation in the presence of three-dimensional islands during heteroepitaxial growth. Phys. Rev. B 70, 235312(9).

Chen, G., Lichtenberger, H., Bauer, G., Jantsch, W., Schäffler, F., 2006. Initial stage of two-dimensional to three-dimensional transition of a strained SiGe layer on a pit-patterned Si(001) template. Phys. Rev. B 74, 035302(8).

Chiu, C.-h., 1999a. The self-assembly of uniform heteroepitaxial islands. Appl. Phys. Lett 75, 3473–3475.

Chiu, C.-h., 1999b. Three-dimensional simulation of the morphological evolution of a strained film on a thick substrate. MRS Symp. Proc. 529, 125–130.

Chiu, C.-h., 2004. Stable and uniform arrays of self-assembled nanocrystalline islands. Phys. Rev. B 69, 165413(4).

Chiu, C.-h., Gao, H., 1993. Stress singularities along a cycloid rough surface. Int. J. Solids Struct. 30, 2983–3012.

Chiu, C.-h., Gao, H., 1995. A numerical study of stress controlled surface diffusion during epitaxial film growth. In: Baker, S. P., Borgesen, P., Townsend, P. H., Ross, C. A., Volkert, C. A. (Eds.), Thin Films: Stresses and Mechanical Properties V. Materials Research Society, Pittsburgh, pp. 33–44.

Chiu, C.-h., Huang, Z., 2006. The common features of nanostructure formation induced by the surface undulation on the Stranski-Krastanow systems. Appl. Phys. Lett. 89, 171904(3).

Chiu, C.-h., Huang, Z., 2007. Numerical simulation for the formation of nanostructures on the Stranski-Krastanow systems by surface undulation. J. Appl. Phys. 101, 113540(10).

Chiu, C.-h., Huang, Z., Poh, C. T., 2004. Formation of nanostructures by the activated Stranski-Krastanow transition method. Phys. Rev. Lett. 93, 136105(4).

Chiu, C.-h., Huang, Z., Poh, C. T., 2006. Formation of nanoislands by the electromolding self-organization process. Phys. Rev. B 73, 193409(4).

Chiu, C.-h., Poh, C. T., 2005. Strain energy of nanocrystalline islands on strained film-substrate systems. Phys. Rev. B 71, 045406(16).

Chiu, C.-h., Wang, H., 2007. First-order perturbation solutions of embedded strain wires. J. Appl. Phys. 100, 123506(10).

Chokshi, N., Bouville, M., Millunchick, J. M., 2002. Pit formation during the morphological evolution of InGaAs/GaAs. J. Crystal Growth 236, 563–571.

Chokshi, N. S., Millunchick, J. M., 2000. Cooperative nucleation leading to ripple formation in ingaas/gaas films. Appl. Phys. Lett. 76, 2382–2384.

Chou, S. Y., Zhuang, L., Guo, L., 1999. Lithographically induced self-construction of polymer microstructures for resistless patterning. Appl. Phys. Lett. 75, 1004–1006.

Cui, Y., Lieber, C. M., 2001. Functional nanoscale electronic devices assembled using silicon nanowire building blocks. Science 291, 851–853.

Daruka, I., Barabasi, A.-L., 1997. Dislocation-free island formation in heteroepitaxial growth: a study at equilibrium. Phys. Rev. Lett. 79, 3708–3711.

Daruka, I., Tersoff, J., Barabási, A.-L., 1999. Shape transition in growth of strained islands. Phys. Rev. Lett. 82, 2753–2756.

Deng, X., Krishnamurthy, M., 1998. Self-assembly of quantum-dot molecules: heterogeneous nucleation of SiGe islands on Si(100). Phys. Rev. Lett. 81, 1473–1476.

Deshpande, P., Chou, S. Y., 2001. Lithographically induced self-assembly of microstructures with a liquid filled gap between the mask and polymer surface. J. Vac. Sci. Technol. B 19, 2741–2744.

Du, D., Srolovitz, D., 2004. Electrostatic filed-induced surface instability. Appl. Phys. Lett. 85, 4917–4919.

Eaglesham, D. J., Cerullo, M., 1990. Dislocation-free stranski-krastanow growth of Ge on Si(100). Phys. Rev. Lett. 64, 1943–1946.

Eggleston, J. J., Voorhees, P. W., 2002. Ordered growth of nanocrystals via a morphological instability. Appl. Phys. Lett. 80, 306–308.

Eisenberg, H. R., Kandel, D., 2000. Wetting layer thickness and early evolution of epitaxially strained thin films. Phys. Rev. Lett. 85, 1286–1289.

Eshelby, J. D., 1970. Energy relations and the energymomentum tensor in continuum mechanics. In: Kanninen, M. F. (Ed.), Inelastic Behavior of Solids. McGraw-Hill, New York, pp. 78–115.

Floro, J. A., Chason, E., Twesten, R. D., Hwang, R. Q., Freund, L. B., 1997. Sige coherent islanding and stress relaxation in the high mobility regime. Phys. Rev. Lett. 79, 3946–3949.

Floro, J. A., Lucadamo, G. A., Chason, E., Freund, L. B., Sinclair, M., Twesten, R. D., Hwang, R. Q., 1998. Sige island shape transitions induced by elastic repulsion. Phys. Rev. Lett. 80, 4717–4720.

Floro, J. A., et al., 2000. Novel sige island coarsening kinetics: Ostwald ripening and elastic interaction. Phys. Rev. Lett. 84, 701–704.

G., S., M., P., P., M., V., H., G., B., H., K. H., L., S.-R., 2000. Tuning of vertical and lateral correlations in self-organized PbSe/$\text{Pb}_{1-x}\text{Eu}_x\text{Te}$ quantum dot superlattices. Phys. Rev. Letts. 84, 4669–4672.

Gao, H., 1991a. A boundary perturbation analysis for elastic inclusions and interfaces. Int. J. Solids Struct. 28, 703–725.

Gao, H., 1991b. Morphological instabilities along surfaces of anisotropic solids. In: Wu, J. J., Ting, T. C. T., Barnett, D. (Eds.), Modern Theory of Anisotropic Elasticity and Applications. SIAM, Philadelphia, pp. 139–150.

Gao, H., 1994. Some general properties of stress-driven surface evolution in a heteroepitaxial thin film structure. J. Mech. Phys. Solids 42, 741–772.

Goldfarb, I., Hayden, P. T., Owen, J. H. G., Briggs, G. A. D., 1997. Nucleation of “hut” pits and clusters during gas-source molecular-beam epitaxy of Ge/Si(001) in in situ scanning tunnelng microscopy. Phys. Rev. Lett. 78, 3959–3962.

Golovin, A. A., Davis, S. H., Voorhees, P. W., 2003. Self-organization of quantum dots in epitaxially strained solid films. Phys. Rev. E 68, 056203(11).

Gray, J. L., Atha, S., Hull, R., Floro, J. A., 2004a. Hierarchical self-assembly of epitaxial semiconductor nanostructures. Nano Lett. 4, 2447–2450.

Gray, J. L., Hull, R., Floro, J. A., 2002. Control of surface morphology through variation of growth rate in SiGe/Si(100) epitaxial films: nucleation of quantum fortresses. Appl. Phys. Lett. 81, 2445–2447.

Gray, J. L., Hull, R., Floro, J. A., 2004b. Formation of one-dimensional surface grooves from pit instabilities in annealed SiGe/Si(100) epitaxial films. Appl. Phys. Lett. 85, 3253–3255.

Gray, J. L., Hull, R., Floro, J. A., 2006. Periodic arrays of epitaxial self-assembled SiGe quantum dot molecules grown on patterned Si substrates. J. Appl. Phys. 100, 084312(7).

Gray, J. L., Hull, R., Lam, C.-H., Sutter, P., Means, J., Floro, J. A., 2005. Beyond the heteroepitaxial quantum dot: self-assembling complex nanostructures controlled by strain and growth kinetics. Phys. Rev. B 72, 155323(11).

Gray, J. L., Singh, N., Elzey, D. M., Hull, R., Floro, J. A., 2004c. Kinetic size selection mechanisms in heteroepitaxial quantum dot molecules. Phys. Rev. Lett. 92, 135504(4).

Helen, R. E., Daniel, K., 2005. Formation, ripening, and stability of epitaxially strained island arrays. Phys. Rev. B 71, 115423(9).

Herring, C., 1950. Diffusional viscosity of a polycrystalline solid. J. Appl. Phys. 21, 437–445.

Huang, Z., Zhou, T., Chiu, C.-h., 2007. Size selection of the cooperative ridge-trench formation on heteroepitaxial systems. Phys. Rev. Lett. 98, 196102(4).

Hughes, T. J. R., 1987. The Finite Element Method. Prentice-Hall, Singapore.

Jang, C. H., Paik, S. I., Kim, Y. W., Lee, N.-E., 2007. Substrate pit formation and surface wetting during thermal annealing of strained-Si/relaxed-$Si_{0.78}Ge_{0.22}$ heterostructure. Appl. Phys. Lett. 90, 091915(3).

Jesson, D. E., Chen, K. M., Pennycook, S. J., Thundat, T., Warmack, R. J., 1996. Morphological evolution of strained films by cooperative nucleation. Phys. Rev. Lett. 77, 1330–1333.

Jin, G., Liu, J. L., Wang, K. L., 2000. Regimented placement of self-assembled Ge dots on selectively grown Si mesas. Appl. Phys. Lett. 76, 3591–3593.

Kamins, T. I., Ohlberg, D. A. A., Williams, R. S., Zhang, W., Chou, S. Y., 1999. Positioning of self-assembled, single-crystal, germanium islands by silicon nanoimprinting. Appl. Phys. Lett. 74, 1773–1775.

Kamins, T. I., Williams, R. S., 1997. Lithographic positioning of self-assembled Ge islands on Si(001). Appl. Phys. Lett. 71, 1201–1203.

Kammler, M., hull, R., Reuter, M. C., Ross, F. M., 2003. Lateral control of self-assembled island nucleation by focused-ion-beam micropatterning. Appl. Phys. Lett. 82, 1093–1095.

Kim, D., Lu, W., 2006. Three-dimensional model of electrostatically induced pattern formation in thin polymer films. Phys. Rev. B 73, 035206(7).

Kiravittaya, S., Heidemeyer, H., Schmidt, O. G., 2004. Growth of three-dimensional quantum dot crystals on patterned GaAs(001) substrates. Physica E 23, 253–259.

Kitajima, T., Liu, B., Leone, S. R., 2002. Two-dimensional periodic alignment of self-assembled Ge islands on patterned Si surfaces. Appl. Phys. Lett. 80, 497–499.

Konkar, A., Madhukar, A., Chen, P., 1998. Stress-engineered spatially selective self-assembly of strained InAs quantum dots on nonplanar patterned GaAs(001) substrates. Appl. Phys. Lett. 72, 220–222.

Kukta, R. V., Freund, L. B., 1997. Minimum energy configuration of epitaxial material clusters on a lattice-mismatched substrate. J. Mech. Phys. Solids 45, 1835–1860.

Lam, C.-H., Lee, C.-K., Sander, L. M., 2002. Competing roughening mechanisms in strained heteroepitaxy: a fast kinetic monte carlo study. Phys. Rev. Lett. 89, 216102(4).

Leach, K. A., Lin, Z., Russell, T. P., 2005. Early stages in the growth of electric field-induced surface fluctuations. Macromolecules 38, 4868–4873.

Lee, H., Johnson, J. A., Speck, J. S., Petroff, P. M., 2000. Controlled ordering and positioning of InAs self-assembled quantum dots. J. Vac. Sci. Technol. B 18, 2193–2196.

Leo, P. H., Sekerka, R. F., 1989. The effect of surface stress on crystal-melt and crystal-crystal equilibrium. Acta Metall. Mater. 37, 3119–3138.

Leonard, D., Krishnamurhty, M., Reaves, C. M., Denbaars, S. P., Petroff, P. M., 1993. Direct formation of quantum-sized dots from uniform coherent islands of InGaAs on GaAs-surfaces. Appl. Phys. Lett 63, 3203–3205.

Leonard, D., Krishnamurhty, M., Reaves, C. M., Denbaars, S. P., Petroff, P. M., 1994. Molecular-beam epitaxy growth of quantum dots from strained coherent uniform islands of InGaAs on GaAs. J. Vac. Sci. Technol. B 12, 1063–1066.

Levine, M. S., Golovin, A. A., Davis, S. H., Voorhees, P. W., 2007. Self-assembly of quantum dots in a thin epitaxial film wetting an elastic substrate. Phys. Rev. B 75, 205312(11).

Li, J. H., Moss, S. C., Han, B. S., Mai, Z. H., 2001. Evolution of island-pit surface morphologies of InAs epilayers grown on GaAs (001) substrates. J. Appl. Phys 89, 3700–3705.

Liang, J., Suo, Z., 2001. Stable island arrays by height-constrained Stranski-Krastanov growth. Appl. Phys. Lett. 20, 3251–3253.

Lin, Z., Kerle, T., Baker, S. M., Hoagland, D. A., Schäffer, E., Steiner, U., Russell, T. P., 2001. Electric field induced instabilities at liquid/liquid interfaces. J. Chem. Phys. 114, 2377–2381.

Liu, F., Metiu, H., 1993. Dynamics of phase separation of crystal surfaces. Phys. Rev. B 48, 5808–5811.

Liu, P., Lu, C., Zhang, Y. W., 2007. Formation of surface structures during heteroepitaxial thin film growth on prepatterned substrates. Phys. Rev. b 76, 085336(5).

Liu, P., Zhang, Y. W., 2007. Morphological evolution of heteroepitaxial islands during Stranski-Krastonov growth. Int J Solids Struct 44, 1733–1744.

Liu, P., Zhang, Y. W., Lu, C., 2003a. Coarsening kinetics of heteroepitaxial islands in nucleationless Stranski-Krastanov growth. Phys. Rev. B 68, 035402(8).

Liu, P., Zhang, Y. W., Lu, C., 2003b. Finite element simulations of the self-organized growth of quantum dot superlattices. Phys Rev B 44, 1733–1744.

Liu, P., Zhang, Y. W., Lu, C., 2003c. Formation of self-assembled heteroepitaxial islands in elastically anisotropic films. Phys. Rev. B 67, 165414(6).

Lu, G. H., Liu, F., 2005. Atomistic view of the recombinative desorption of H2 from H/Si(100). Phys. Rev. Lett 94, 196103(4).

Lu, W., Koerner, H., Vaia, R., 2006. Effect of electric field on exfoliation of nanoplates. Appl. Phys. Lett. 89, 22–24.

Machtay, N. D., Kukta, R. V., 2006. Energetics of epitaxial island arrangements on substrate mesas. J. Appl. Mech. 73, 212–219.

McKay, H. A., Dehne, A., Lee, J. Y., Millunchick, J. M., 2007. Focused-ion-beam-directed nucleation of InAs quantum dots. Appl. Phys. Lett. 90, 163109(3).

Medeiros-Ribeiro, G., Bratkovski, A. M., Kamins, T. I., Ohlberg, D. A. A., Williams, R. S., 1998. Shape transition of germanium nanocrystals on a silicon (001) surface from pyramids to domes. Science 279, 353–355.

Mo, Y.-W., Savage, D. E., Swartzentruber, B. S., Lagally, M. G., 1990. Kinetic pathways in Stranski-Krastanov growth of Ge on Si(001). Phys. Rev. Lett. 65, 1020–1023.

Morariu, M., Voicu, N., Schäffer, E., Lin, Z., Russell, T. P., Steiner, U., 2003. Hierarchical structure formation and pattern replication induced by an electric field. Nature Materials 2, 48–52.

Muller, J., Grand, M., 1999. Model of surface instabilities induced by stress. Phys. Rev. Lett 82, 1736–1739.

Mullins, W. W., 1957. Theory of thermal grooving. J. Appl. Phys. 28, 333–339.

Nitta, Y., Shibata, M., Fujita, K., Ichikawa, M., 2000. Nanometer-scale Ge selective growth on Si(001) using ultrathin SiO_2 film. Surf. Sci. 462, L587–L593.

Orlov, A. O., Amlani, I., Bernstein, G. H., Lent, C., Snider, G. L., 1997. Realization of a functional cell for quantum-dot cellular automata. Science 277, 928–930.

Ortiz, M., Repetto, E. A., Si, H., 1999. A continuum model of kinetic roughening and coarsening in thin films. J. Mech. Phys. Solids 47, 697–730.

Ozkan, C. S., Nix, W. D., Gao, H., 1997. Strain relaxation and defect formation in heteroepitaxial $Si_{1-x}Ge_x$ films via surface roughening induced by controlled annealing experiments. Appl. Phys. Lett. 70, 2247–2249.

Ozkan, C. S., Nix, W. D., Gao, H., 1999. Stress-driven surface evolution in heteroepitaxial thin films: anisotropy of the two-dimensional roughening mode. J. Mater. Res. 14, 3247–3256.

Pang, Y., Huang, R., 2007. Bifurcation of surface pattern in epitaxial thin films under anisotropic stresses. J. Appl. Phys. 2, 023519(5).

Pascale, A., Gentile, P., Eymery, J., Mezière, J., Bavard, A., Schülli, T. U., Fournel, F., 2006. Ge quantum dots growth on nanopatterned Si(001) surface: morphology and stress relaxation study. Surf. Sci. 600, 3187–3193.

Pease, I., F., L., Russel, W. B., 2004. Limitations on length scales for electrostatically induced submicrometer pillars and holes. Langmuir 20, 795–804.

Poydenot, V., Dujardin, R., Rouvière, J. L., Barski, A., Mezière, J., Fournel, F., 2006. Ordered growth of germanium dots induced by the strain field of tilt dislocations in molecular bonded silicon (001) thin films. Surf. Sci. 600, L135–L138.

Ramasubramaniam, A., Shenoy, V. B., 2004. Three-dimensional simulations of self-assembly of hut-shaped Si-Ge quantum dots. J. Appl. Phys. 95, 7813–7824.

Rastelli, A., Kummer, M., von Känel, H., 2001. Reversible shape evolution of Ge islands on Si(001). Phys. Rev. Lett. 87, 256101(4).

Rastelli, A., von Känel, H., Spencer, B. J., Tersoff, J., 2003. Prepyramid-pyramid transition of SiGe islands on Si(001). Phys. Rev. B 68, 115301(6).

Retford, C. M., Asta, M., Miksis, M. J., Voorhees, P. W., Webb, E. B. I., 2007. Energetics of 105-faceted Ge nanowires on Si(001): An atomistic calculation of edge contributions. Phys. Rev. B 75, 075311–075318.

Rice, J. R., 1968. A path independent integral and the approximate analysis of strain concentration by notches and cracks. J. Appl. Mech. 35, 379–386.

Rice, J. R., Chuang, T.-J., 1981. Energy variation in diffusive cavity growth. J. Amer. Ceramic. Soc 64, 46–53.

Robinson, J. T., Liddle, J. A., Minor, A., Radmilovic, V., Dubon, O. D., 2006. Morphological evolution of Ge islands on Au-patterned Si. J. Crystal Growth 287, 518–521.

Robinson, J. T., Ratto, F., Moutanabbir, O., 2007. Gold-catalyzed oxide nanopatterns for the directed assembly of Ge island arrays on Si. Nano Lett. 9, 2655–2659.

Romanov, A. E., Petroff, P. M., Speck, J. S., 1999. Lateral ordering of quantum dots by periodic subsurface stressors. Appl. Phys. Lett. 74, 2280–2282.

Ross, F. M., Tromp, R. M., Reuter, M. C., 1999. Transition states between pyramids and domes during Ge/Si island growth. Science 286, 1931–1934.

Schäffer, E., Thurn-Albrecht, T., Russell, T. P., Steiner, U., 2000. Electrically induced structure formation and pattern transfer. Nature 403, 874–877.

Schmidt, O. G., Jin-Phillipp, N. Y., Lange, C., Denker, U., Eberl, K., Schreiner, R., Grabeldinger, H., Schweizer, H., 2000. Long-range ordered lines of self-assembled Ge islands on a flat Si(001) surface. Appl. Phys. Lett. 77, 4139–4141.

Shchukin, V. A., Bimberg, D., 1998. Strain-driven slef-organization of nanostructures on semiconductor surfaces. Appl. Phys. A: Mater. Sci. Process 67, 687–700.

Shchukin, V. A., Ledentsov, N. N., Kop'ev, P. S., Bimberg, D., 1995. Spontaneous ordering of arrays of coherent strained islands. Phys. Rev. Lett. 75, 2968–2971.

Shi, H., Lederman, D., 2000. Annealed Co thin films: Pit formation and magnetic anisotropy. J. Appl. Phys. 87, 6095–6097.

Shiryaev, S. Y., et al., 1997. Nanoscale structuring by misfit dislocations in $Si_{1-x}Ge_x$/Si epitaxial systems. Phys. Rev. Letts. 78, 503–506.

Shklyaev, O. E., Beck, M. J., Asta, M., Miksis, M. J., Voorhees, P. W., 2005. Role of strain-dependent surface energies in Ge/Si(100) island formation. Phys. Rev. Lett 94, 196102(4).

Sirlpitakchai, N., Suraprapapich, S., 2007. Evolution of self-assembled lateral quantum dot molecules. J. Crystal Growth 301, 812–816.

Songmuang, R., Kiravittaya, S., Schmidt, O. S., 2003. Formation of lateral quantum dot molecules around self-assembled nanoholes. Appl. Phys. Lett. 82, 2892–2894.

Spencer, B. J., 1999. An asymptotic derivation of the glued wetting layer model and contact angle condition for stranski-krastanow islands. Phys. Rev. B 59, 2011–2017.

Spencer, B. J., Davis, S. H., Voorhees, P. W., 1993. Morphological instability in epitaxially strained dislocation-free solid films-nonlinear evolution. Phys. Rev. B 47, 9760–9777.

Spencer, B. J., Tersoff, J., 1997. Equilibrium shape and properties of epitaxially strained islands. Phys. Rev. Lett. 79, 4858–4861.

Spencer, B. J., Voorhees, P. W., Davis, S. H., 1991. Morphological instability in epitaxially strained dislocation-free solid films. Phys. Rev. Lett 67, 3696–3699.

Spencer, B. J., Voorhees, P. W., Tersoff, J., 2001. Morphological instability theory for strained alloy film growth: the effect of compositional stresses and species-dependent surface mobilities on ripple formation during epitaxial film deposition. Phys. Rev. B 64, 235318–235348.

Srolovitz, D. J., 1989. On the stability of surfaces of stressed solids. Acta Metall. Mater. 37, 621–625.

Stoffel, M., Rastelli, A., Stangl, J., Merdzhanova, T., Bauer, G., Schmit, O., 2007. Shape oscillations: A walk through the phase diagram of strained islands. Phys. Rev. B 75, 113307(4).

Suo, Z., Zhang, Z., 1998. Epitaxial films stabilized by long-range forces. Phys. Rev. B 58, 5116–5120.

Tekalign, W. T., Spencer, B. J., 2004. Evolution equation for a thin epitaxial film on a deformable substrate. J. Appl. Phys. 96, 5505–5512.

Tersoff, J., 1991. Stress-induced layer-by-layer growth of Ge on Si(100). Phys. Rev. B 43, 9377–9380.

Tersoff, J., Spencer, B. J., Rastelli, A., von Känel, H., 2002. Barrierless formation and faceting of SiGe islands on Si(001). Phys. Rev. Lett. 89, 196104(4).

Tersoff, J., Teichert, C., Lagally, M. G., 1996. Self-organization in growth of quantum dot superlattices. Phys. Rev. Lett. 76, 1675–1678.

Tersoff, J., Tromp, R. M., 1993. Shape transition in growth of strained islands: spontaneous formation of quantum wires. Phys. Rev. Lett. 70, 2782–2785.

Tu, Y., Tersoff, J., 2007. Coarsening, mixing, and motion: the complex evolution of epitaxial islands. Phys. Rev. Lett. 98, 096103(4).

Vandervelde, T. E., Kumar, P., Kobayashi, T., Gray, J. L., Pernell, T., Floro, J. A., Hull, R., Bean, J. C., 2003. Growth of quantum fortress structures in $Si_{1-x}Ge_x/Si$ via combinatorial deposition. Appl. Phys. Lett. 82, 5205–5207.

Verma, R., Sharma, A., Kargupta, K., Bhaumik, J., 2005. Electric field induced instability and pattern formation in thin liquid films. Langmuir 21, 3710–3721.

Weil, J. D., Deng, X., Krishnamurthy, M., 1998. Preferential nucleation of Ge islands at self-organized pits formed during the growth of thin Si buffer layers on Si(110). J. Appl. Phys. 83, 212–216.

Xie, Z. G., Solomon, G. S., 2005. Spatial ordering of quantum dots in microdisks. Appl. Phys. Lett. 87, 093106(3).

Yang, B., Liu, F., Lagally, M. G., 2004. Local strain-medicated chemical potential control of quantum dot self-organization in heteroepitaxy. Phys. Rev. Lett. 92, 025502(4).

Yoon, T.-S., et al., 2006. Selective growth of Ge islands on nanometer-scale patterned SiO_2/Si substrate by molecular beam epitaxy. Appl. Phys. Lett. 89, 063107(3).

Zhang, R., Tsui, R., Shiralagi, K., Convey, D., Goronkin, H., 1998. Selective formation and alignment of InAs quantum dots over mesa stripes along the [011] and [001] directions on GaAs (100) substrates. Appl. Phys. Lett. 73, 505–507.

Zhang, Y. W., 2000. Self-organization, shape transition, and stability of epitaxially strained islands. Phys. Rev. B 61, 10388–10392.

Zhang, Y. W., Bower, A. F., 2001. Three-dimensional analysis of shape transitions in strained-heteroepitaxial islands. Appl. Phys. Lett. 78, 2706–2708.

Zhong, Z., Halilovic, A., Fromherz, T., Schäffler, F., Bauer, G., 2003. Two-dimensional periodic positioning of self-assembled ge islands on prepatterned Si(001) substrates. Appl. Phys. Lett. 82, 4779–4781.

Zhu, J.-H., Brunner, K., Abstreiter, G., 1998. Two-dimensional ordering of self-assembled Ge islands on vicinal Si(001) surfaces with regular ripples. Appl. Phys. Lett. 73, 620–622.